BOSTON UNIVERSITY

GRADUATE SCHOOL OF ARTS AND SCIENCES

Dissertation

USE OF *IN SITU* AND AIRBORNE DATA TO ASSESS SATELLITE-BASED ESTIMATES OF DIRECTIONAL REFLECTANCE AND ALBEDO

by

MIGUEL O. ROMÁN

B.Sc., University of Puerto Rico, Mayagüez, 2004
M.Eng., Cornell University, Ithaca, 2005

Submitted in partial fulfillment of the

requirements for the degree of

Doctor of Philosophy

2009

Approved by

First Reader

Crystal B. Schaaf, Ph.D.
Research Professor of Geography and Environment at
Boston University Graduate School of Arts & Sciences

Second Reader

Alan H. Strahler, Ph.D.
Professor of Geography and Environment at
Boston University Graduate School of Arts & Sciences

Third Reader

Curtis E. Woodcock, Ph.D.
Professor of Geography and Environment at
Boston University Graduate School of Arts & Sciences

Acknowledgements

There are a lot people that have helped me throughout the many years of study leading to the culmination of this dissertation; certainly, more than I can acknowledge by name in this section. I wish to acknowledge and thank each of them for all they have done to help me in my achievements. There are a few I would like to give a special acknowledgement. First I wish to thank my wife, for her love, patience, and understanding through this timely process; to my mother, who has challenged me to see the world in new ways; and to my brother and sister, for always being there for me despite geographical distance.

I would like most sincerely to thank my academic advisor, Dr. Crystal B. Schaaf, for her support and guidance throughout this study. I have benefited greatly from her expertise and from the help and advice she has given me throughout all the stages of this project. I would also like to thank the members of my dissertation committee, Dr. Alan H. Strahler and Dr. Curtis E. Woodcock, for their support throughout the dissertation period. Thanks to them, I quickly learned to apply the key principles of quantitative remote sensing and spatial accuracy assessments discussed in this dissertation. Special thanks also go to Dr. Charles K. Gatebe for hosting my fellowship assignments at NASA Goddard Space Flight Center and for his technical assistance throughout the field and instrument deployments during the 2007 CLASIC experiment. I would like to acknowledge Dr. Jeffrey T. Morisette, for his review of this text, remarkable insights, and valuable suggestions on the development of new validation techniques using MODIS data.

I express my earnest acknowledgement to Dr. Sucharita Gopal for sharing with me her expertise on the concepts of geospatial data integration. Christopher DeVits, Jennifer Stacy, Theresa White, Erin Wnorowski, and Victoria Woodward have always been there to solve any administrative hassle. Grateful thanks to Don Johnson for keeping the workstations up and running 24/7.

I would also like to thank the fellow graduates and alumni from Boston University's Center for Remote Sensing and the Department of Geography and Environment for providing a cheerful and stimulating work environment. Special thanks go to Yanmin Shuai, Dr. Jicheng Liu, Dr. Qingling Zhang, Zhuosen Wang, Xiaoyuan Yang, Feng Zhao, Tian Yao, Dr. Ziti Jiao, Jonathan Salomon, Mitchell Schull, Dr. Sangram Ganguly, Damien Sulla-Menashe, Manish Verma, Martin Gamache, and Bill Boykin Morris. Thanks also go to Raul Fernandez and the wonderful staff at the Howard Thurman Center for Race, Culture & Ethnicity, for providing me with a home away from home while at BU.

Nearly all of my undergraduate and post-graduate education has been supported by the National Aeronautics and Space Administration for which I am extremely grateful. I have always received unyielding support from my NASA mentors to pursue my educational endeavors, which is a credit to the agency that values and fosters a highly educated workforce. In particular, I would most sincerely like to thank the Office of Higher Education, including Mablelene S. Burrell, David J. Rosage, Dr. Vigdor L. Teplitz, and Dr. Mabel J. Matthews, as well as the NASA Harriet G. Jenkins Pre-doctoral

Fellowship Program Office (JPFP); in particular, Dr. Melissa C. Green, Dr. Sonya L. Greene, and all my fellow colleagues from JPFP Cohort IV.

Finally, I would like to thank my dear friends and mentors, Dr. Michael D. King, Dr. Gail P. Anderson, Dr. Michael J. Hill, Dr. William D. Philpot, Dr. Mason A. Peck, and Dr. Peter L. Jackson, for supporting me through my academic and professional development; and Dr. Lawrence Jacobowitz, Dr. Casimer Decusatis, Dr. Enectalí Figueroa-Feliciano, Dr. Christa Peters-Lidard, and Dr. Ramón E. Vásquez-Espinoza, for encouraging me to pursue higher studies, and for challenging me to become a better engineer and a decent scientist.

USE OF *IN SITU* AND AIRBORNE DATA TO ASSESS SATELLITE-BASED ESTIMATES OF DIRECTIONAL REFLECTANCE AND ALBEDO

(Order No.)

MIGUEL O. ROMÁN

Boston University Graduate School of Arts and Sciences, 2009

Major Professor: Crystal B. Schaaf, Professor of Geography and Environment

ABSTRACT

Accurate representation of the regional characteristics of anisotropic light scattering by land surfaces under a wide range of sky conditions is required (1) for modeling atmospheric shortwave radiative fluxes; (2) for modeling the energy exchange between the earth and atmosphere; and (3) determining the lower boundary conditions for atmospheric radiative transfer models. However, uncertainties due to spatial scale arise when models that describe the albedo and reflectance anisotropy of land surfaces are directly compared against in-situ measurements. This research focuses on comparisons between satellite, airborne, and ground measurements, namely, MODerate Resolution Imaging Spectroradiometer (MODIS) Bidirectional Reflectance Distribution Function (BRDF) and Albedo products, airborne angular reflectance measurements, and point tower albedo measurements. A new integrated methodology for establishing the spatial representativeness between tower measurements of surface albedo and MODIS retrievals is developed. This method brings together knowledge of the intrinsic biophysical properties of a given spatial domain and its surrounding landscape to produce a number of geostatistical attributes that describe the overall variability, spatial extent, strength, and temporal structure of surface albedo patterns at separated seasonal periods throughout the year. Local upscaling results over a wide range of forested ecosystems demonstrate the ability of this method to identify landscapes that capture the spatial and seasonal features of surface albedo over large enough footprints to be suitable for use in modeling studies. Airborne measurements from NASA's Cloud Absorption Radiometer taken over agricultural and natural landscapes in the Southern Great Plains (SGP) region during the Cloud and Land Surface Interaction Campaign (CLASIC) were utilized to compare the spatial characteristics between finer-scale BRDFs and MODIS retrievals in a well-characterized atmospheric regime. Results confirm that the semi-empirical kernel models used in MODIS data processing generally capture surface heterogeneities. Regional upscaling results across the entire 142,000-square-kilometer SGP domain show consistent agreement, generally meeting pixel-specific accuracy requirements of 0.02 units and realistically accounting for solar zenith angle dependences between spatially-integrated retrievals of surface albedo from 22 evenly distributed facilities and co-located MODIS retrievals. This synergy between local and regional analyses improves the confidence of MODIS retrievals, thus providing the necessary quality controls required by rigorous modeling efforts.

Table of Contents

List of Tables

List of Figures

List of Abbreviations

6S	Second Simulation of a Satellite Signal in the Solar Spectrum
AERONET	AErosol RObotic NETwork Program
ARM	Atmospheric Radiation Measurement Program
ASTER	Advanced Spaceborne Thermal Emission and Reflection Radiometer
AVHRR	Advanced Very High Resolution Radiometer
AWiFS	Advanced Wide Field Sensor
BHR	Bi-hemispherical Reflectance
BRDF	Bidirectional Reflectance Distribution Function
BSA	Black-sky Albedo
CAR	Cloud Absorption Radiometer
CAVE	CERES ARM Validation Experiment
CERES	Clouds and the Earth's Radiant Energy System
CF	ARM Central Facility
ChEAS	Chequamegon Ecosystem Atmosphere Study
CLASIC	Cloud and Land Surface Interaction Campaign
CLM	Community Land Model
CMG	Climate Modeling Grid
CV	Coefficient of Variation
DHR	Directional Hemispherical Reflectance
DN	Digital Number
DOE	Department of Energy
EDR	Earth-Science Data Record
ER-2	Earth Resources Aircraft
ETM+	Landsat 7 Enhanced Thematic Plus Instrument
FC	Fort Cobb Watershed
FS	Okmulgee Forest Site
GCM	General Circulation Model

GSFC	Goddard Space Flight Center
HFEMS	Harvard Forest Environmental Measurement Site
IEEE	Institute of Electrical and Electronics Engineers
IGBP	International Geosphere-Biosphere Programme
IOP	Intense Observing Period
J-31	Jetstream-31 Research Aircraft
LAI	Leaf Area Index
LSN	Local Solar Noon
LW	Little Washita Watershed
MISR	Multiangle Imaging Spectroradiometer
MODIS	Moderate Resolution Imaging Spectroradiometer
MODTRAN	Moderate Resolution Atmospheric Transmittance and Radiance
NASA	National Aeronautics and Space Administration
NIR	Near Infrared
NOAA	National Oceanic and Atmospheric Administration
NPOESS	National Polar-orbiting Operational Environmental Satellite System
NPP	NPOESS Preparatory Project
NTB	Narrowband-to-Broadband
PFT	Plant Functional Type
POLDER	Polarization and Directionality of the Earth’s Reflectances
QA	Quality Assessment
QQ	Quantile-Quantile
RCF	Radiometric Calibration Facility
RMSE	Root Mean Squared Error
RTLSR	RossThick-LiSparse Reciprocal Model
SAA	Solar Azimuth Angle
SBDART	Santa Barbara DISORT Atmospheric Radiative Transfer Code
SGP	Southern Great Plains
SWIR	Shortwave Infrared

SZA	Solar Zenith Angle
TOA	Top-of-Atmosphere
UCI	University of California-Irvine
UMBS	University of Michigan Biological Station
UTM	Universal Transverse Mercator
VCF	Vegetation Continuous Fields
VIS	Visible Solar Range
WGS	World Geodetic System
WSA	White Sky Albedo

Chapter 1

1. Introduction

1.1. Research statement

A major goal of NASA’s Earth observation efforts is the long term monitoring of key biophysical variables and the production of long term and consistent parameters for rigorous modeling studies. The MODIS BRDF/Albedo products (Lucht et al. 2000; Schaaf et al. 2002; Schaaf et al. 2008) have been embraced by the modeling community since the launch of NASA’s Terra and Aqua satellites (King and Herring 2000; Parkinson 2003). These highly successful products have been available since 2000 and will be entering their sixth reprocessing cycle in 2009. MODIS BRDF/Albedo retrievals have been recently validated to a stage-2 (i.e. over a widely distributed set of locations and time periods via several ground-truth and validation efforts) (Morisette et al. 2006) and the high quality primary algorithm has been shown to produce consistent global land surface albedo quantities over a variety of land surface types and snow cover conditions (Jin et al. 2003a; 2003b; Liu et al. 2009; Román et al. 2009a; 2009b; Salomon et al. 2006).

Additional assessments over a wide range of spatial (from 10s of meters to 5-30 km) and temporal (from daily to monthly) scales are nonetheless required to accurately provide users with a pixel-specific measure of product uncertainty – both in terms of the quality of the model inversions (e.g. given a limited number of cloud-free satellite observations) and their ability to capture the underlying spatial and seasonal variability of the underlying landscape. However, estimating these uncertainties is complicated because it requires an accurate understanding of the intrinsic properties and anisotropic behavior of the landscape at both local and regional modeling scales. This research specifically focuses on estimating these uncertainties by combining satellite, airborne, and ground measurements, namely, the MODIS BRDF/Albedo retrievals, airborne angular reflectance measurements, and point tower albedo measurements, in a geostatistical framework.

A synergy between local and regional assessments contributes to a better understanding of the relationships between vegetation parameters estimated from remotely sensed data and scale. The role played by scale in models describing the BRDF of land surfaces needs to be understood in terms of scale-driven multidirectional and multispectral signatures from different satellite and airborne sensors. These assessment activities are directly relevant to NASA’s mission of delivering improved Earth-Science Data Records (EDRs), improved modeling of the Earth’s water and energy cycles, and address the need for on-going evaluation and validation of long-term consistent terrestrial and climate-quality products.

1.2. Background

The properties of anisotropic light scattering by land surfaces is described and specified by the bidirectional reflectance distribution function (BRDF) (Nicodemus

1977). The BRDF provides surface reflectance explicitly in terms of its spectral, directional, spatial, and temporal properties. It is used in remote sensing applications for extracting primary biophysical parameters (Gao et al. 2003; Hill et al. 2008), for the correction of view and illumination angle effects (Li et al. 1996; Strahler et al. 1996), for land cover classification schemes (Friedl et al. 2002; Friedl and Strahler 2000), for vegetation monitoring (Zhang et al. 2003), for cloud detection (d'Entremont et al. 1996; DiGirolamo and Davies 1994; Leroy et al. 1997), for atmospheric correction (Kaufman 1989), and other applications. The BRDF gives the lower radiometric boundary condition for any radiative transfer problem in the atmosphere and is hence of relevance for climate modeling and energy budget investigations.

The availability of a large number of directional reflectances available from a particular land surface over a wide angular range can effectively capture its surface anisotropy and thus be used to accurately model the surface albedo. Knowledge of the BRDF of the Earth’s land surface can also be used to derive intrinsic surface albedos in the absence of atmospheric effects, which are mathematically defined as weighted integrals (or averages) of the BRDF (Wanner et al. 1997). More generally albedo is defined as the ratio of radiant energy scattered upward and away from the surface in all directions to the downwelling irradiance incident upon the surface. Measuring changes in intrinsic (atmospheric-independent) surface albedo through time provides a quantitative means for tracking land surface change and measuring that change in terms that can be directly applied by regional and global modeling efforts, in particular those which have to monitor energy transfer at the surface. Variations in the extent of snow cover and flooding, the phenology of natural vegetation and agricultural crops, as well as other signatures from rapidly changing surface covers (e.g. burning, clearing, and tilling) are all accompanied by significant changes in surface albedo (Schaaf et al. 2008). Surface albedo also varies strongly with seasonal trends, soil-vegetation contrasts, and canopy chemistry and structure (Ollinger et al. 2008). If the albedo of the soil surface is significantly different from above-canopy albedo, for example, any changes in vegetation cover that may expose the soil can be important (Berbet and Costa 2003). Rainfall events can also reduce the magnitude of sparse above-canopy albedo by as much as 50% of its dry-peak, and are more persistent if the downpour occurs in the morning than in the afternoon. Daily variations in actual land-atmosphere coupled surface albedo are also influenced by changes in water-vapor content, which absorbs strongly in the NIR (0.7 – 5.0 μm) region, and by changing atmospheric conditions (clouds and haze) that influence the partitioning of direct and diffuse solar irradiance. Over bright-colored soils, vegetation cover reduces surface albedo, whereas plants on dark or litter-covered soils increase surface albedo (Rechid and Jacob 2006). These considerations underscore the importance of understanding the natural and anthropogenic influences in surface albedo for determining changes in global climate.

Actual surface albedo is a continuously varying function of both the specific atmospheric conditions that modulate the incoming solar irradiance as well as the intrinsic anisotropic scattering of the surface as determined by the reflected irradiance. Consequently, an accurate estimation of actual surface albedo is dependent on an accurate description of the overlying atmosphere as well as the intrinsic reflective properties of the underlying surface (i.e. the intrinsic albedo) at a specific point in time. When dealing with accuracy requirements for albedo, Henderson-Sellers and Wilson (1983) and Sellers et al. (1995) proposed an absolute accuracy of ±0.02-0.05 units, or equal to an accuracy on monthly averaged reflected solar irradiance of ±10 Wm^{-2}, for snow-free and snow-covered albedos in the full solar range (0.3 - 5.0 μm). This is required at a diverse range of spatial (from 10s of meters to 5-30 km) and temporal (from daily to monthly) scales. Estimating albedos at intra-daily scales also influences the accuracy of daily mean values of albedo. For instance a lack of consideration of the diurnal cycle of surface albedo yields an absolute error on the daily mean value of up to ±0.03 units, corresponding to 15% in relative terms (Grant et al. 2000). Similarly, Kimes et al. (1987) reported a 18% relative error on the daily mean value of reflected solar irradiance.

Satellite remote sensing offers the only realistic means of monitoring the BRDF and surface albedo in a continental or global sense by providing spatially variable and temporally dynamic observations. However, the ability of a satellite sensor to characterize the BRDF at any point on the Earth's surface is dependent on its ability to acquire a sufficient number of high-quality retrievals over a wide angular (both view and solar) range. Global land surface anisotropy products must also contend with issues of cloud-clearing, snow detection, and aerosol correction as well as sensor-specific matters of view angle, spatial footprint, gridding, repeat cycles, and narrowband- to broadband conversion. These problems have been successfully overcome in BRDF retrieval algorithms for polar orbiting satellite sensors, such as those of MODIS (Lucht et al. 2000; Schaaf et al. 2002; 2008; Wanner et al. 1997), MISR (Diner et al. 1998), Meteosat

(Pinty et al. 2000), MSG/Seviri (Geiger et al. 2008); and POLDER (Bacour and Breon 2005; Buriez et al. 2007; Hautecoeur and Leroy 1998; Maignan et al. 2004). Among these, the MODIS (Collection V005) BRDF/Albedo product routinely provides global multispectral anisotropy model information (or BRDF parameters), intrinsic measures of albedo, including "black-sky" albedo (directional-hemispherical reflectance), and "white-sky" albedo (bihemispherical reflectance under isotropic illumination), and nadir BRDF-adjusted surface reflectances every 8 days at 500 m, 1 km, 30 arc-sec and 0.05 deg resolutions. The algorithm relies on multi-day, cloud-free, atmospherically-corrected surface reflectances from both Terra and Aqua to sample the surface reflectance anisotropy over a 16 day period, and allow for the retrieval of a reflectance anisotropy model for each pixel.

A number of studies have evaluated the consistency of these various satellite-derived global land surface albedo products against in-situ data at different spatial and temporal scales (Chen et al. 2008; Hautecoeur and Roujean 2007; Jin et al. 2003a; 2003b; Liang et al. 2002; Liu et al. 2009; Rutan et al. 2009; Salomon et al. 2006). These assessments have been carried out under the general assumption that both the satellite and tower albedo measurements are roughly sampling the same spatial domain. However, the vast differences in spatial resolution invariably create a number of challenges for such direct “point-to-pixel” comparisons. Surface albedo, within and between different ecosystems differ as a function of spatial resolution and, consequently, scaling errors plague satellite to field measurement comparisons. These spatial albedo patterns will also change seasonally and are particularly hard to establish throughout periods of rapidly changing surface conditions. Recent studies have addressed these scaling issues by employing fine spatial resolution datasets to form the intermediary basis between field measurements and MODIS data (Baccini et al. 2004; Baret et al. 2006; Tian et al. 2004). Additional advances in spatially-explicit environmental research have been increasingly aided by the field of geostatistics. One of the most frequently used geostatistical tools for describing the spatial continuity of primary biophysical properties is the semivariogram (Carroll and Cressie 1996; Davis 1986; Isaaks and Srivastava 1989; Materon 1963). Remote sensing data enables efficient monitoring of the properties of semivariograms and its most important characteristics, namely the sill, range, and nugget-effect, and can further reveal highly interesting patterns of spatial variability and scaling information. Accordingly a new set of routines were developed during this research to establish whether a given field station is spatially representative of the broader regional ecosystems. By employing a combination of geostatistical models and aggregation techniques, these efforts seek to provide a better understanding the intrinsic properties and anisotropic behavior of surface albedo at a diverse range of spatial and seasonal scales.

Aircraft retrievals of the BRDF and albedo serve as important additional sources of validation land surface satellite products. By transforming and scaling the directional surface reflectances derived from the Cloud Absorption Radiometer (CAR) into image space, this research seeks to recreate the measurement methodology, spatial coverage, and data processing protocols employed in the MODIS satellite data processing. Surface anisotropy data acquired by the CAR throughout the 2007 Cloud and Land Surface

Interaction Campaign (CLASIC) provide the ideal scenario to evaluate the consistency of BRDF retrievals at increased scales of interest (i.e. 50 to 500 m) and to evaluate the ability of the MODIS data to reproduce areal-mean signatures of the finer-scale retrievals of the BRDF and albedo possible from the airborne sensor.

Previous global and regional assessments of satellite driven products have not focused on the changes seen in surface albedo, and related sources of uncertainty, back to their primary drivers. Fewer regional studies have investigated the degree of correspondence between areal-mean estimates of surface albedo and in-situ measurements at the multiple spatial scales at which MODIS data are commonly utilized (Baret et al. 2006; Trishchenko et al. 2005). Accordingly, this dissertation focuses on both global and regional assessments of surface albedo, based on comparisons between daily retrievals at local solar noon (LSN) of the MODIS BRDF/Albedo product against a number of upscaling approaches that utilize a combination of in-situ data sources, from tower albedo measurements to finer scale BRDFs of archetypal landscapes, to drive the MODIS albedo retrievals over the entire domain of the ARM-SGP region.

1.3. Structure of this dissertation

1.3.1. Assessment of Spatial Representativeness over Forested Landscapes

A major effort of this research is to establish the spatial representativeness of tower albedo measurements that are routinely used in validation of retrievals from the MODIS

V005 BRDF/Albedo product. This was achieved by combining knowledge of the spatial and temporal dynamics of the landscape, using multispectral high spatial resolution imagery, to produce a number of geostatistical attributes that describe the overall variability, spatial extent, strength, and temporal structure of surface albedo patterns for a given measurement site. A validation scheme was implemented over a wide range of forested landscapes, looking at both deciduous and coniferous sites, from tropical to boreal ecosystems.

1.3.2. Airborne Measurements of Surface Anisotropy at the SGP-Site

Local upscaling techniques were then applied using airborne retrievals of the BRDF derived from the CAR across thee SGP-Central Facility during CLASIC. The directional signatures acquired by the CAR were processed to specifically recreate the measurement methodology, spatial coverage, and data processing protocols employed in the MODIS satellite data processing. Results provide fine-scale retrievals of the BRDF, at 50 m and 100 m spatial resolutions, for the representative land covers across the SGP-CF, over eight spectral bands, three broadbands, and including a number of quality assurance fields. Comparisons between the spatial characteristics of the finer-scale airborne retrievals and the MODIS retrievals were then performed to assess the degree of correspondence at the native (500 m) MODIS resolution. The diurnal performance of surface albedos derived from MODIS and CAR retrievals was also evaluated using tower albedo measurements at the ARM-SGP Central Facility throughout the period of CLASIC.

1.3.3. Development of a Confidence Layer for the MODIS BRDF/Albedo Product

To further explore the scaling gaps between the point-based and satellite-based retrievals, region-based assessments of spatial representativeness for broader regional ecosystems were developed. The key sources of uncertainty of regional and global-scale albedos across the entire 142,000-square-kilometer ARM-SGP domain, were identified by evaluating the spatial correspondence between daily albedo retrievals at LSN from MODIS and surface albedo fields reconstructed from spatial aggregations based on: (1) finer-scale areal-mean albedos that were reconstructed from 50 m BRDF retrievals of archetypal landscapes as derived by the CAR during the 2007 CLASIC campaign; and (2) areal interpolations of ground albedo measurements, from 20 field station across the SGP region, using ordinary kriging techniques with a spherical variogram model fit. Thus, this research establishes a new set of confidence layers for the MODIS BRDF/Albedo product that provide a measure of pixel-specific accuracy at regional (500 m) and global modeling scales (0.05°).

1.3.4. Concluding Remarks

This research is focused on comparisons between satellite, airborne, and ground measurements, namely, MODIS, CAR, and point tower albedometer measurements. This synergy of local, regional, and global analyses contributed to the confidence of MODIS retrievals, thus providing the necessary quantification of quality required by surface energy budget investigations (Kustas et al. 2004), climate models (Dickinson et al. 1990; Lawrence and Chase 2007; Lean and Rowntree 1997; Oleson et al. 2003; Roesch et al. 2004; Wang et al. 2004; Zhou et al. 2003), biogeochemical models (Sitch et al. 2003), and weather forecasting schemes (Ferranti and Viterbo 2006; Morcrette 2000).

Chapter 2

2. Assessment of Spatial Representativeness over Forested Landscapes

2.1. Introduction

The ability to characterize the spatial representativeness of a measurement site has significant implications in the efficiency of direct “point-to-pixel” assessments of surface biophysical properties derived from satellite data. This would enable a better understanding of product uncertainty, both in terms of the quality of the model inversions (e.g. given a limited number of cloud-free satellite observations), and their ability to capture the underlying spatial variability of the surrounding landscape. However, estimating these uncertainties is complicated because it requires an accurate understanding of the intrinsic properties and anisotropic behavior of the underlying landscape. Accordingly, this chapter introduces a new methodology for validating the MODIS BRDF/Albedo product (Figure 2.1), which focuses on quantifying the spatial representativeness – defined here as the degree to which a retrieval of surface albedo (whether ground or satellite-based) is able to resolve the spatial and seasonal variability of the adjacent landscape – by combining knowledge of the spatial and temporal dynamics of the landscape with multispectral high spatial resolution imagery, in a geostatistical framework.

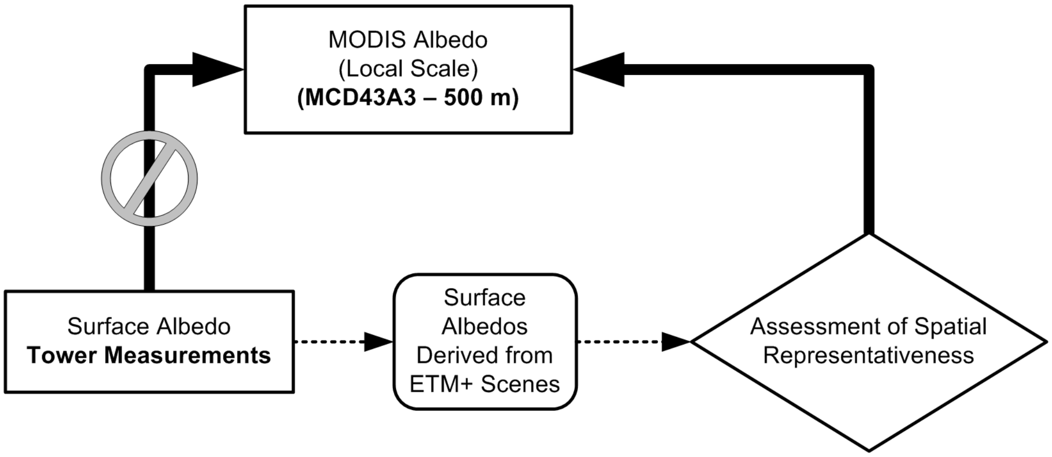

Figure 2.1. A new methodology for evaluating the MODIS BRDF/Albedo product assesses the spatial representativeness at local (site-level) scales.

By resolving the residual spatial and seasonal dependence of surface albedo over a wide-range of forested landscapes where above-canopy albedometers have been recently deployed, we can identify field stations that are appropriately representative of a large enough footprint to validate satellite-derived retrievals of albedo; and, if needed, recommend a series of instrumental upgrades (e.g. increasing the height of the tower and instrument field of view) to properly improve their utility for evaluating satellite-derived retrievals of albedo. This method is very much within the overall trend for MODIS validation; and is related to previously introduced methods that also employ fine spatial resolution datasets to form the intermediary basis between field measurements and MODIS data (Baccini et al. 2004; Baret et al. 2006; Tian et al. 2004).

Note that the goal of this research is to provide measures of spatial representativeness, as opposed to spatial heterogeneity. One could argue that the observed landscape can be categorized as both spatially heterogeneous and spatially representative depending on, among several things, the structural consistency between the landscape elements resolved by both the ground instrument field of view (be it from a small 10 m flux tower or a tall radio tower albedometer overlooking a 1 km circular footprint) and the surrounding region extending to the size of the satellite pixel.

This chapter is organized as follows. First, we detail the definitions and major theory to be used; and provide a description of the ground and remote sensing data sources, including an overview of the MODIS (Collection V005) BRDF/Albedo product. Implementation of the proposed geostatistical framework was developed as follows: (1) surface albedos were derived from Landsat 7 Enhanced Thematic Mapper Plus (ETM+) retrievals according to the methodology of (Liang 2001); (2) semivariogram functions were then extracted from ETM+ subsets and evaluated at increased scales of interest; and (3) the geostatistical attributes of spatial representativeness were calculated at separated seasonal periods throughout the year (i.e. during leaf-on and leaf-off conditions). We also provide various examples over a select number of measurement sites to explain the thought process behind these measures. A validation scheme was then implemented over a wide range of forested landscapes, looking at both deciduous and coniferous sites, from tropical to boreal ecosystems. These scheme is presented in the results section through a comparison of daily retrievals of surface albedo at LSN from the MODIS V005 500 m albedo product (MCD43A3) against coincident ground retrievals; and a comparison between the geostatistical attributes of spatial representativeness and the abovementioned validation results during representative periods of leaf-on and leaf-off conditions. The techniques and results are then summarized in the conclusions.

2.2. Background

The following two sections define and distinguish the variables of interest: surface radiative properties related to BRDF and albedo, and remote sensing measurements. The definitions are then linked to nomenclatures proposed by Nicodemus (1977) and reviewed in Martonchik et al. (2000) and Schaepman-Strub et al. (2006).

2.2.1. BRDF, Albedo, and Other Definitions

The spectral bidirectional reflectance distribution function (BRDF) describes the scattering of a parallel beam of incident light from one direction in the hemisphere into another direction in the hemisphere. It is defined as the ratio of the radiance observed through an infinitesimally small solid angle cone, *dL* [W m^{-2} sr^{-1}], to the irradiance illuminating that surface within an infinitesimal solid angle *dE* [W m^{-2}]:

$$BRDF_{\lambda} = f_r(\theta_s, \phi_s; \theta_v, \phi_v; \lambda) = \frac{dL(\theta_s, \phi_s; \theta_v, \phi_v; \lambda)}{dE(\theta_s, \phi_s; \lambda)} \left[sr^{-1} \right] \tag{2.1}$$

The BRDF is a function of solar zenith angle, θ_s, solar azimuth angle, ϕ_s, pixel viewing zenith angle, θ_v, pixel viewing azimuth angle ϕ_v, and wavelength λ. It is the basic quantity that geometrically characterizes the reflecting properties of a surface. The subscript *r* is thus used to describe reflected radiation. On the other hand, hemispherical reflectance in the form of the two purely reflected fractions of direct and diffuse irradiance can also be derived from BRDF:

$$BSA(\theta_s, \phi_s, \lambda) = \int_0^{2\pi} \int_0^{\frac{\pi}{2}} f_r(\theta_s, \phi_s; \theta_v, \phi_v; \lambda) \cos\theta_v \sin\theta_v d\theta_v d\phi_v \qquad (2.2)$$

$$WSA(\lambda) = \frac{1}{\pi} \int_0^{2\pi} \int_0^{\frac{\pi}{2}} BSA(\theta_s, \phi_s, \lambda) \cos\theta_s \sin\theta_s d\theta_s d\phi_s \qquad (2.3)$$

The directional-hemispherical reflectance (DHR), or ‘‘black-sky’’ albedo (BSA), is the albedo that would be expected when the surface is irradiated by a plane parallel beam, with no diffuse radiation. Conversely, the bi-hemispherical reflectance (BHR), or ‘‘white-sky’’ albedo (WSA), is the albedo for isotropic diffuse light only, with no direct radiation (comparable but not equivalent to totally overcast sky conditions) (Martonchik et al. 2000). Since the black-sky and white-sky albedo quantities only depend on the BRDF, they also describe the properties of a reflecting surface and are: (1) intrinsic to a specific location, (2) governed by the character and structure of its land cover, and (3) independent of atmospheric conditions.

Broadband albedos are obtained by integrating spectral albedo over wavelength, usually referring to the entire spectrum of solar radiation (0.3–5.0 µm). Frequently, visible (0.3 - 0.7 µm) and near-infrared (0.7 - 5.0 µm) broadband albedos are also of interest due to the marked difference of the reflectance of vegetation in these two spectral regions. More precise work (e.g. aerosol remote sensing, surface aerosol forcing, and radiative transfer calculations) requires the use of spectral (or narrowband) albedos, referenced to specific wavelengths such as those originating from the spectral bands of an instrument.

2.2.2. RossThick-LiSparseReciprocal BRDF Kernel Model

Being a ratio of infinitesimal quantities, the BRDF cannot be measured directly (Schaepman-Strub et al. 2006). However, it can be estimated using surface reflectance models in conjunction with high-quality, clear-sky, atmospherically-corrected surface reflectances acquired at different view and solar angles. These data can be expanded into a linear sum of terms (or kernels) characterizing different scattering modes that, when combined, result in a kernel-based BRDF model (Roujean et al. 1992; Wanner et al. 1995). The superposition assumes that these modes are either spatially distinct within the scene viewed with little cross-coupling, physically distinct within a uniform canopy with negligible interaction, or empirically justified (Strahler et al. 1999). In this work, we use the kernel models employed in the MODIS V005 BRDF/albedo product, which result from a reciprocal version of the semiempirical RossThick-LiSparse model (RTLSR) (Lucht et al. 2000; Wanner et al. 1995; 1997):

$$\begin{aligned} BRDF(\theta_s, \theta_v, \Delta\phi, \lambda) &\cong R(\theta_s, \theta_v, \Delta\phi, \Lambda) \\ &= f_{iso}(\Lambda) + \; f_{vol}(\Lambda) K_{vol}(\theta_s, \theta_v, \Delta\phi) \,, \\ &\quad + f_{geo}(\Lambda) K_{geo}(\theta_s, \theta_v, \Delta\phi, P_4, P_5) \end{aligned} \tag{2.4}$$

where

$$K_{VOL} \quad = \quad \frac{(\pi/2 - \xi)\cos\xi + \sin\xi}{\cos\theta_s + \cos\theta_v} - \frac{\pi}{4} \tag{2.5}$$

$$\cos\xi = \cos\theta_s \cos\theta_v + \sin\theta_s \sin\theta_v \cos\Delta\phi \tag{2.6}$$

$$K_{GEO} = \frac{1+\sec\theta_s'\sec\theta_v' + \tan\theta_s'\tan\theta_v'\cos\Delta\phi}{2} + \left(\frac{t-\sin t\cos t}{\pi} - 1\right)\left(\sec\theta_s' + \sec\theta_v'\right) \tag{2.7}$$

$$\cos^2 t = \min\left\{\left(\frac{P_4}{\sec\theta_v' + \sec\theta_s'}\right)^2 \left[D^2 + \left(\tan\theta_v' \tan\theta_s' \sin\Delta\phi\right)^2\right],\ 1\right\} \tag{2.8}$$

$$\tan\theta_x' = P_5 \tan\theta_x \quad ;\ x = v \ \ or \ \ s \tag{2.9}$$

$$D = \sqrt{\tan^2\theta_s' \ \tan^2\theta_v' - 2\tan\theta_s' \ \tan\theta_v' \ \cos\Delta\phi} \tag{2.10}$$

In remote sensing measurement terms, we define wavelength for the narrow band instruments of interest here as the solar spectrum weighted center, Λ, of the spectral band of a particular instrument. Parameter $f_{iso}(\Lambda)$ is the isotropic scattering component and equal to the bidirectional reflectance for a pixel viewing zenith angle $\theta_v = 0$ and a solar zenith angle $\theta_s = 0$. Parameter $f_{geo}(\Lambda)$ is the coefficient of the LiSparse-Reciprocal geometric scattering kernel K_{GEO}, derived for a sparse ensemble of surface casting shadows on a lambertian background (Li and Strahler 1992). Parameter $f_{vol}(\Lambda)$ is the coefficient for the RossThick volume scattering kernel K_{VOL}, so called for its assumption of a dense leaf canopy (Ross 1981). $\Delta\phi$ is the relative view-sun azimuth angle ($\Delta\phi = \phi_S - \phi_V$) and ξ is the scattering phase angle between sun and view directions. The two constants, dimensionless crown relative height (P_4 = h / b) and shape (P_5 = b / r) parameters, have been fixed at h / b = 2 and b / r =1 to invert the angular radiance data from MODIS (Wanner et al. 1997). For these two parameters, h is the variable for height at which a crown center is located, b is the vertical half axis of the modeled ellipsoid, and r is its horizontal radius.

In summary, we use the following colloquial designation, in the current study: actual albedo for apparent (or instantaneous or blue-sky) albedo, and white-sky and black-sky albedo for the intrinsic albedos (bihemispherical reflectance under isotropic illumination and directional hemispherical reflectance at a particular illumination) of the land surface. Note that throughout the dissertation, we express these three quantities in both their narrowband and broadband forms. We also use the terms directional surface reflectance for the remote sensing retrievals of narrowband atmospherically-corrected bidirectional reflectance, and BRDF parameters for the weights of each of the RTLSR kernel coefficients used in forming the overall surface reflectance from MODIS.

2.3. Ground Data Sources

2.3.1. AmeriFlux Network

Tower-based albedo measurements were acquired over a broad range of forested landscapes that are part of the AmeriFlux network of sites and the global network, FLUXNET (Table 2.1). The AmeriFlux network provides continuous observations of ecosystem level exchanges of CO_2, water, energy, and momentum spanning diurnal, synoptic, seasonal, and interannual time scales and is currently composed of sites from North America, Central America, and South America (Law et al. 2002; Running et al. 1999).

The fields stations in this study cover a broad range in climate and growth form, including ponderosa pine in the Southwestern US, broadleaf forest in the Midwest, and subtropical semidecidous broadleaf forests in the Amazon region. A total of 42 site-years worth of data include a wide range, from recently harvested plantation stands to old-growth forests. Measurement sites were instrumented with Kipp and Zonen (CNR1, CM-3, or CM-6b), or Eppley-PSP tower albedometers. These sensors have been outfitted with clear domes to collect broadband albedo and radiation fluxes in the shortwave (SWIR) (0.3-2.8 μm). The data received from individual sites have been reviewed and stored as mean values provided at 30 minute intervals. The review process also included additional quality-assurance checks (e.g. consistent units, naming conventions, and reporting intervals) to maintain consistency within the larger network-wide AmeriFlux database.

Table 2.1 Field measurements acquired from the network-wide AmeriFlux database.

Site Name	**Location**	**Forest Type**	**Lat**	**Lon**	**MODIS Tile**	**Time Period**	**Tower Height [m]**	**Data Source**
Santarem-Km83	BRZ	Evergreen Broadleaf	-3.010	-54.582	h12v09	2002-2004	65	(Miller et al. 2004)
UCI-1850 Burn Site	CAN	Evergreen Needleleaf	55.879	-98.484	h12v03	2002-2004	20	(Goulden et al. 2006)
UCI-1930 Burn Site	CAN	Evergreen Needleleaf	55.906	-98.525	h12v03	2002-2004	22	(Goulden et al. 2006)
UCI-1964 Burn Site	CAN	Evergreen Needleleaf	55.912	-98.382	h12v03	2002-2004	12	(Goulden et al. 2006)
UCI-1981 Burn Site	CAN	Evergreen Needleleaf	55.863	-98.485	h12v03	2002-2004	10	(Goulden et al. 2006)
Flagstaff-Managed	USA-AZ	Evergreen Needleleaf	35.133	-111.728	h08v05	2005-2007	23	(Sullivan et al. 2008)
Flagstaff-Unmanaged	USA-AZ	Evergreen Needleleaf	35.089	-111.762	h08v05	2005-2007	23	(Sullivan et al. 2008)
Morgan Monroe	USA-IN	Deciduous Broadleaf	39.323	-86.413	h11v05	2002-2006	48	(Schmid et al. 2002)
Harvard Forest	USA-MA	Deciduous Broadleaf	42.538	-72.171	h12v04	2006-2007	30	(Urbanski et al. 2007)
Howland Forest	USA-ME	Evergreen Needleleaf	45.209	-68.747	h13v04	2007-2007	30	(Hollinger et al. 2004)
UMBS	USA-MI	Mixed	45.560	-84.714	h12v04	2005-2006	50	(Gough et al. 2008)
Ozark Site	USA-MO	Deciduous Broadleaf	38.744	-92.2	h10v05	2004-2006	30	(Gu et al. 2006)
Bartlett Forest	USA-NH	Deciduous Broadleaf	44.065	-71.288	h12v04	2004-2006	25	(Jenkins et al. 2007)
Chestnut Ridge	USA-TN	Deciduous Broadleaf	35.931	-84.332	h11v05	2006-2007	60	(Wilson and Meyers 2007)
Walker Branch	USA-TN	Deciduous Broadleaf	35.959	-84.287	h11v05	2006-2007	40	(Wilson and Meyers 2007)
WLEF-ChEAS	USA-WI	Mixed	45.946	-90.272	h11v04	2006-2007	396	(Davis et al. 2003)

2.4. Remote Sensing Data Sources

2.4.1. MODIS (Collection V005) BRDF/Albedo Product

The MODIS V005 BRDF/Albedo product is available globally at a 500 m spatial resolution (Schaaf et al. 2002; 2008) for the period 2000 - present. It is derived from an algorithm that uses multidate, atmospherically-corrected, spectral, directional surface reflectances from MODIS sensor onboard the Terra and Aqua satellites to establish a sparsely-filled estimate of the BRDF of land surfaces (Lucht et al. 2000; Schaaf et al. 2002) over a 16-day period. In view of the often insufficient angular sampling available, this synergistic use of multi-sensor observations has offered the best opportunity to improve both the coverage and the quality of global anisotropy and albedo retrievals. These products have thus far been validated to a stage-2 (i.e. over a widely distributed set of locations and time periods via several ground-truth and validation efforts) (Morisette et al. 2006) and the high quality primary algorithm has been shown to produce consistent global land surface albedo quantities over a variety of land surface types and snow cover.

The MODIS V005 BRDF/Albedo product provides RTLSR BRDF kernel model parameters, which can be used to compute the intrinsic black-sky albedo (directional-hemispherical reflectance) and white-sky albedo (bihemispherical reflectance under isotropic illumination):

$$BSA(\theta_s, \Lambda) = \sum_k f_k(\Lambda) h_k(\theta_s) \tag{2.11}$$

$$WSA(\Lambda) = \sum_k f_k(\Lambda) H_k \tag{2.12}$$

where, $h_k(\theta_s)$ is the integral of the RTLSR BRDF model kernels k over θ_v and ϕ_v; H_k is the integral of h_k over θ_s; and $f_k(\Lambda)$ are the RTLSR BRDF kernel model parameters k, which are retrieved from multiangular reflectance observations. Note that the kernel integrals, H_k and h_k, do not depend on the observations; they may therefore be pre-computed and stored. This is a feature specific to kernel-based BRDF models (Strahler et al. 1999).

We define the actual surface albedo, $a(\theta_s,\Lambda)$, as the ratio of radiant fluxes; thus, it is a function of the intrinsic anisotropic character of the surface coupled with the specific atmospheric conditions that may be overlying that surface at any particular point in time. To accurately couple these satellite-derived intrinsic quantities with field and airborne-derived albedos, the MODIS black-sky and white-sky quantities must be combined as a function of solar geometry and atmospheric state:

$$\begin{aligned} a(\theta_s,\Lambda) = \{1 - S(\theta_s,\tau_{0.55\mu m})\} \cdot BSA(\theta_s,\Lambda) \\ + S(\theta_s,\tau_{0.55\mu m}) \cdot WSA(\Lambda) \end{aligned}, \tag{2.13}$$

where $S(\theta_{s,}\tau_{0.55\mu m})$ is the proportion of diffuse skylight (Lewis and Barnsley 1994; Lucht et al. 2000), which is assumed as an isotropic fraction of total illumination, at a certain point in time for a given aerosol optical depth $\tau_{0.55\mu m}$.

The white-sky and black-sky albedo quantities are retrieved in seven narrow spectral bands between 0.4 - 2.4 µm. Since field-measured albedos commonly tend to be measured in broadband quantities, the MODIS V005 BRDF/Albedo product also provides broadband retrievals of intrinsic albedo (i.e. BSA(θ_s)$_{BB}$ and WSA$_{BB}$) and reflectance anisotropy ($F_{ISO\text{-}BB}$, $F_{VOL\text{-}BB}$, and $F_{GEO\text{-}BB}$) in the visible (0.3 - 0.7 µm), near-infrared (0.7 - 5.0 µm), and the entire spectrum of solar radiation (0.3 - 5.0 µm) (e.g. Figure 3.4). Given $S(\theta_{s,}\tau_{0.55\mu m})$ for a particular instant during the day, we can also produce an actual broadband albedo retrieval (A(θ_s)$_{BB}$) equivalent to measurements in the field.

In addition to the spectral and broadband BRDF model and albedo quantities themselves, the MODIS V005 BRDF/Albedo product provides extensive quality information. A full retrieval of the parameters for the RTLSR BRDF model is attempted if sufficient high-quality, cloud-free well distributed directional samples are acquired during a 16-day period. A backup algorithm is used if insufficient directional samples survive the screening process or if a robust full retrieval cannot be made. This method relies on a global database of archetypal anisotropic models applied to a custom land cover classification using historical high-quality full model retrievals of both leaf-on and leaf-off vegetation situations (Strugnell et al. 2001). This *a priori* database is then used as an estimate of the underlying BRDF and any available observations are used to constrain the model. Salomon et al. (2006) found that the combination of MODIS Aqua and Terra sensor data has increased the occurrence of high quality fully data-driven retrievals and thus reduced the product's reliance upon *a-priori* determinations of the underlying surface anisotropy used by the backup algorithm.

A major improvement in Collection V005 of the MODIS reprocessing is an increase in spatial resolution to a nominal 500 m pixel resolution. Due to the extraordinary geolocation capabilities of the MODIS instruments (in the range of 45 m ±1 sigma) (Wolfe et al. 2002), the 500 m products were implemented to satisfy numerous requests from the ecosystem, carbon, hydrological and mesoscale modeling communities. Also, the finer resolution increases our ability to screen for subpixel clouds and snow cover and thus improves the quality of our values at coarser resolutions.

Although cloud contaminated information is detected so that it can be removed from the retrieval, snow covered information is detected so that it can be handled separately. Accordingly, only if a pixel is primarily snow-covered throughout a period is a snow albedo retrieved. By more carefully partitioning observations between snow-free or snow-covered, MODIS retrievals become more characteristic of the actual predominant condition during that period.

2.4.2. MODIS (V005) Aerosol Products

Daily Level 2 aerosol optical depths (at 550nm) available from the MODIS (Collection V005) Aerosol Products (Remer et al. 2005) were acquired over each of our study locations to estimate actual (or blue-sky) albedo retrievals from MODIS. These products, retrieved from both Terra (MOD04_L2) and Aqua (MYD04_L2) platforms, monitor aerosol type, aerosol optical thickness, cloud fraction, particle size distribution, aerosol mass concentration, optical properties, and radiative forcing.

2.4.3. Surface Albedos Derived from ETM+

The methodology for estimating broadband albedos based on empirical relations between surface total shortwave albedo measurements and ETM+ observations was introduced by Liang (2001) and validated in Liang et al. (2003). Using high spatial resolution scenes, this technique requires a series of processing steps as illustrated on Figure 2.2 and summarized here:

1. Top-of-atmosphere (TOA) spectral reflectances are derived from radiometric calibration of Level 1 Digital Numbers (DNs) by using solar irradiance tables and determining the view and illumination conditions at the ETM+ overpass.
2. Directional surface reflectances are then produced by atmospherically correcting the TOA spectral reflectances using the 6Sv4.1 radiative transfer code (Vermote et al. 1997) as well as ground or satellite retrievals of aerosol optical properties measured at the ETM+ overpass.

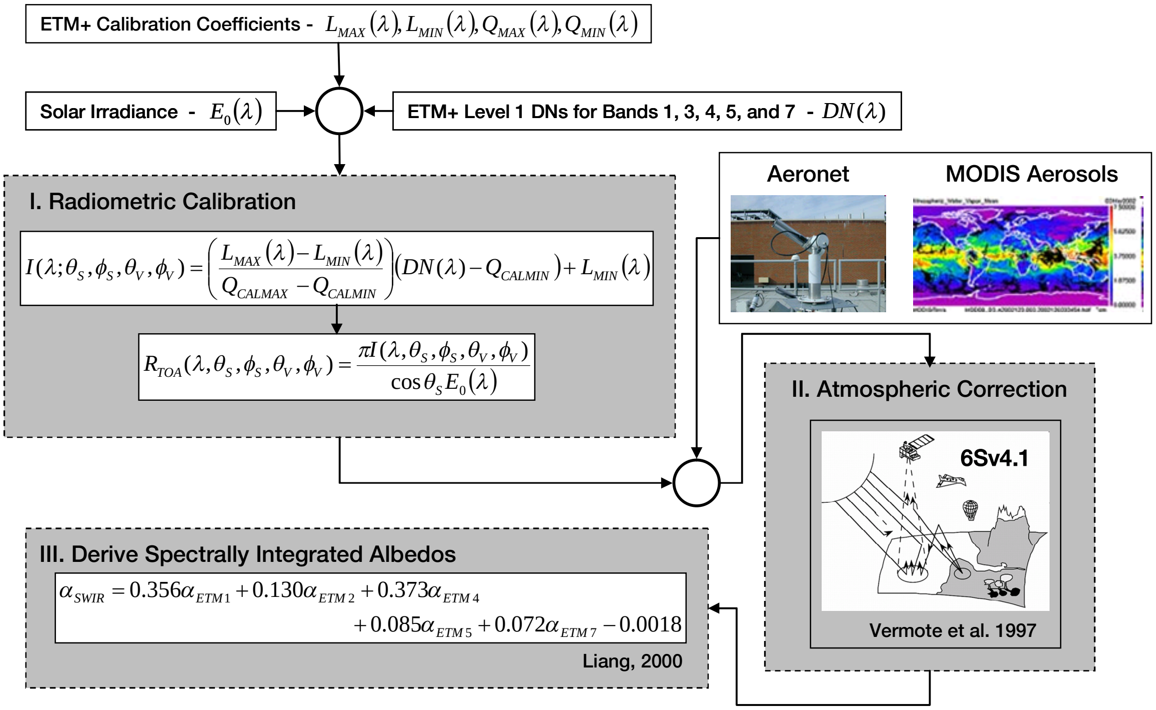

Figure 2.2. Processing and data flow diagram illustrating the production of spectrally integrated shortwave albedos (0.3-5.0 μm) from Landsat 7 ETM+ Level 1 data.

3. Narrowband-to-broadband (NTB) albedo conversions (Liang 2001; 2003) were used to produce surface albedos equivalent to those measured by MODIS and field albedometers.

2.5. Assessment of Spatial Representativeness

Recent advances in spatially-explicit environmental research have been increasingly aided by the field of geostatistics. One of the most efficiently used geostatistical tools for describing the spatial continuity of primary biophysical properties is the semivariogram (Carroll and Cressie 1996; Davis 1986; Isaaks and Srivastava 1989; Materon 1963). Remote sensing data enables efficient monitoring of the properties of semivariograms and its most important characteristics, namely the sill, range, and nugget-effect, and can further reveal highly interesting patterns of spatial variability and scaling information. Accordingly, we have created a number of geostatistical attributes derived from the principles of traditional variography, using Enhanced Thematic Mapper Plus (ETM+) retrievals of surface albedo as an intermediate step between our ground and MODIS estimates, to quantify the spatial representativeness of each of the measurement sites over the spatial scales of MODIS observations. In order to obtain these measures, the following procedures were carried out: (1) create high resolution (30 m) subsets of surface albedo, at each measurement site, using ETM+ retrievals at separated seasonal periods throughout the year (i.e. leaf-on and leaf-off); (2) derive semivariogram attributes (i.e. range, sill, and nugget-effect) and document their changes at increased fields of view; and (3) calculate geostatistical attributes of spatial representativeness.

2.5.1. Semivariogram Attributes (Range, Sill, and Nugget)

After creating subsets of spectrally integrated albedos from ETM+ scenes, we computed the semivariogram values (i.e. nugget-effect, sill, and range) for each subset. The methodology for deriving isotropic (or omnidirectional) variograms to analyze surface albedos using ETM+ subsets as intermediaries between ground and MODIS footprints was recently introduced by Susaki et al. (2007). In this work, the variogram estimator is used to obtain half the average-squared-difference between albedo values that are within certain distance classes or bins defined by multiples of 30 m (i.e. the nominal resolution of ETM+):

$$\gamma_E(h) = 0.5 \cdot \frac{\sum_{i=1}^{N(h)} \left(z_{xi} - z_{xi+h}\right)^2}{N(h)} \tag{2.14}$$

where z_x is the surface albedo at pixel location x and z_{x+h} is the surface albedo at another pixel within a lag distance h. As a rule of thumb, the maximum lag distance used in each semivariogram is constrained by the half maximum distance of the prescribed subset and must be a factor of the minimum lag (i.e. 30 m). Thus, for a 1.0 km subset h_{max} = 690 m, for a 1.5 km subset h_{max} = 1050 m, and for a 2.0 km subset h_{max} = 1410 m. The spatial attributes – range (a), sill (c), and nugget effect (c_0) – can then be modified to fit a spherical model to the variogram estimator:

$$\gamma_{sph}(h) = \begin{cases} c_0 + c \cdot \left(1.5 \cdot \frac{h}{a} - 0.5\left(\frac{h}{a}\right)^3\right) & for\ \ 0 \le h \le a \\ c_0 + c & for\ \ h > a \end{cases} \tag{2.15}$$

A description of isotropic variogram functions and the relevant spatial attributes is presented on Figure 2.3. The variogram range (a) defines the distance from a point beyond which there is no further correlation of a biophysical property associated with that point. It has also been described as the average patch size of the landscape (Cooper et al. 1997); i.e., a region that differs from its surroundings, but is not necessarily internally homogeneous. The variogram sill (c) is the ordinate value of the range at which the semivariogram levels off to an asymptote. Thus, the sill describes the overall variance of the data, while the range describes the separation distance at which this occurs.

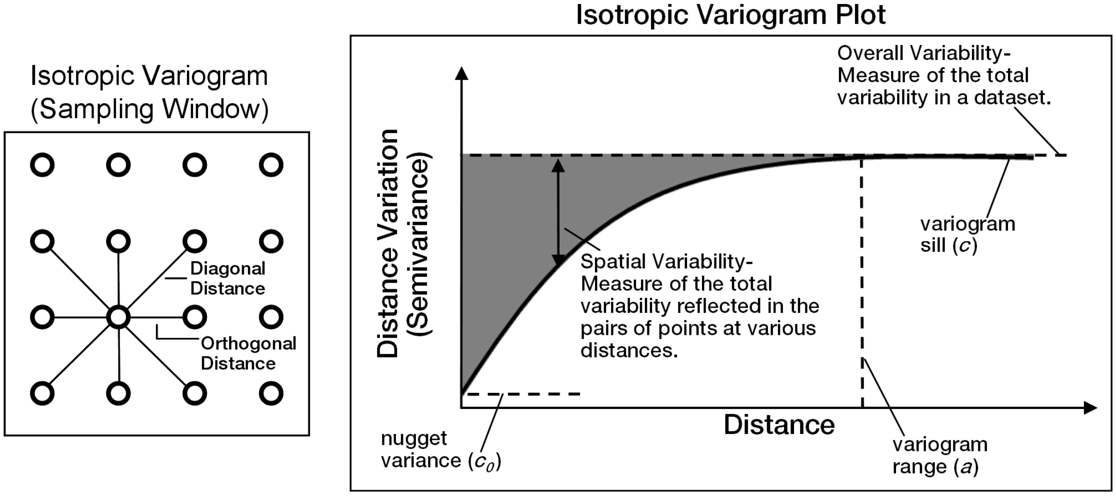

Figure 2.3. Isotropic variogram models are produced by specifying the terms for three model parameters – nugget variance (c_0), sill (c), and range (a).

If it appears that the variogram does not reach zero variance at $h = 0$, the apparent positive intercept is called the nugget variance (c_0). This is equivalent to the variance of lags smaller than that of the sampling distance. This in turn depends on variance associated with small scale variability, measurement errors, or a combination of these (Noreus et al. 1997).

While the MODIS V005 BRDF/Albedo product is reported on a 500 m grid, the retrievals used to obtain the BRDF (and thus the albedo) are based on many observations. Even in the best case scenario of a nadir retrieval centered directly on a 500 m pixel, the MODIS point spread function for just the sensor in the across track direction includes an area as wide as 1km (Tan et al. 2006). Thus, MODIS observations are not necessarily centered on the precise location of the pixel in question. Such retrievals may actually be from a larger spatial domain, depending on sensor view geometry:

$$P \approx \frac{w \cdot d}{\cos(\theta_v)^{1.5}} \tag{2.16}$$

where *P*, is the size of a MODIS pixel [m], *w* is the MODIS instantaneous field of view for the reflective bands (0.6571 mrad), *d* is the altitude of the sensor (705 km), and θ_v is the sensor's view zenith angle. Accordingly, we have extended the routines presented in Susaki et al. (2007) by analyzing the response of semivariogram functions at increased fields of view. Thus, we have created a spatial threshold using 1.0 km, 1.5 km, and 2.0 km subsets to account for all possible areas surrounding the tower that may contribute to the actual BRDF estimate of a single MODIS retrieval. This added feature, i.e. a comparison of semivariogram functions at increasing scales (i.e. 1.0 – 1.5 km), provides an assessment of the spatial characteristics of a given measurement site, and allows us to ultimately examine whether the observed landscape for the albedometers measurements is a representative sample of the area being sensed by the MODIS observations contributing to the albedo retrieval. This is conservative in the sense that it ensures that the albedometer measurements are representative of a fairly large area. Thus, it makes sure that tower sites are representative over relatively large areas to make sure they are suitable for evaluating the MODIS albedo retrievals. One reason this approach is conservative is that the MODIS algorithm has been shown to be a good outlier detector, and internally employs a quality assurance routine that discards the furthermost outliers from retrievals since they are obviously contaminated or of a different ground location than the rest (Schaaf et al. 2002).

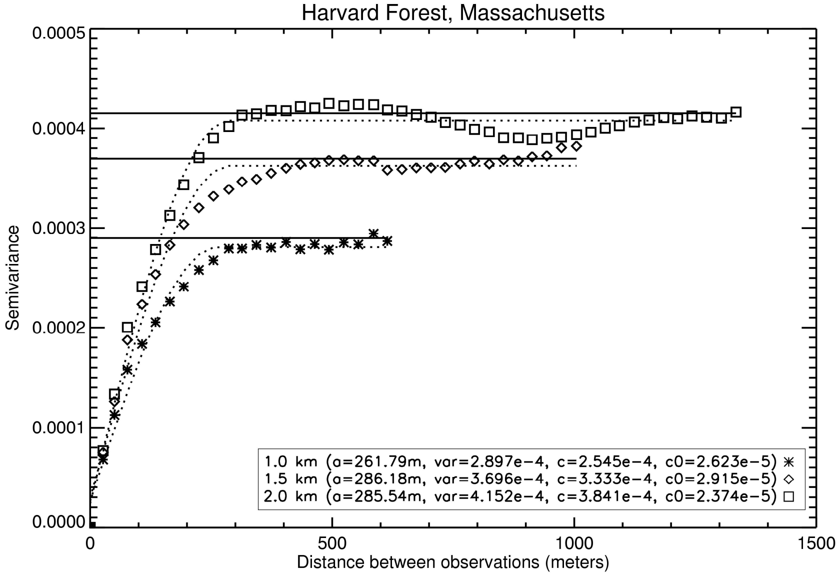

Figure 2.4. Variogram estimator (points), spherical model (dotted curves), and sample variance (solid straight lines) obtained over Harvard Forest using surface albedos derived from an ETM+ scene retrieved in 8 September, 2002 using regions of 1.0 km (asterisks), 1.5 km (diamonds), and 2.0 km (squares).

An example of the semivariogram functions and the relevant spatial attributes (range, sill, nugget-effect) for three ETM+ subsets of size 1.0 km, 1.5 km, and 2.0 km are shown in Figure 2.4 for the Harvard Forest Environmental Measurement Site (HFEMS). The vegetation surrounding the HFEMS is predominantly a mosaic of transitional hardwoods including red oak and red maple; together with some hemlock stands, including white pine and red pine. The relatively sparse understory contains primarily red maple, yellow birch and hemlock saplings plus woody shrubs such as blueberry, and witch hazel. Notice on Figure 2.4 that the point values of the variogram estimator for each of the squared areas are more closely aligned over shorter separation distances (*h*).

The spatial variability over HFEMS, as described by the slope of the ascending limb of the variogram estimator, is also more pronounced over the larger squared regions (1.5 – 2.0 km), since the chances of locating significantly different land cover types at longer separation distances are much higher. Finally, note that, for each of the subsets, the variogram estimator reaches an asymptote, or a constant variance among spatially uncorrelated samples, near the sample variance (*var*) (solid straight lines).

2.5.2. Geostatistical Attributes of Spatial Representativeness

A number of theoretical, empirical, and statistical approaches have been presented by previous studies with the common goal to characterize the spatial dependency of landscape patterns and processes (Cooper et al. 1997; Dent and Grimm 1999; Isaaks and Srivastava 1989; Journel and Huijbregts 1978). Analogously, our main focus is to characterize the spatial representativeness of tower albedo measurements by producing a number of geostatistical attributes that describe the overall variability, spatial extent, strength, and temporal structure of surface albedo patterns for a given measurement site (Figure 2.5). The following sections discuss each of these measures in further detail.

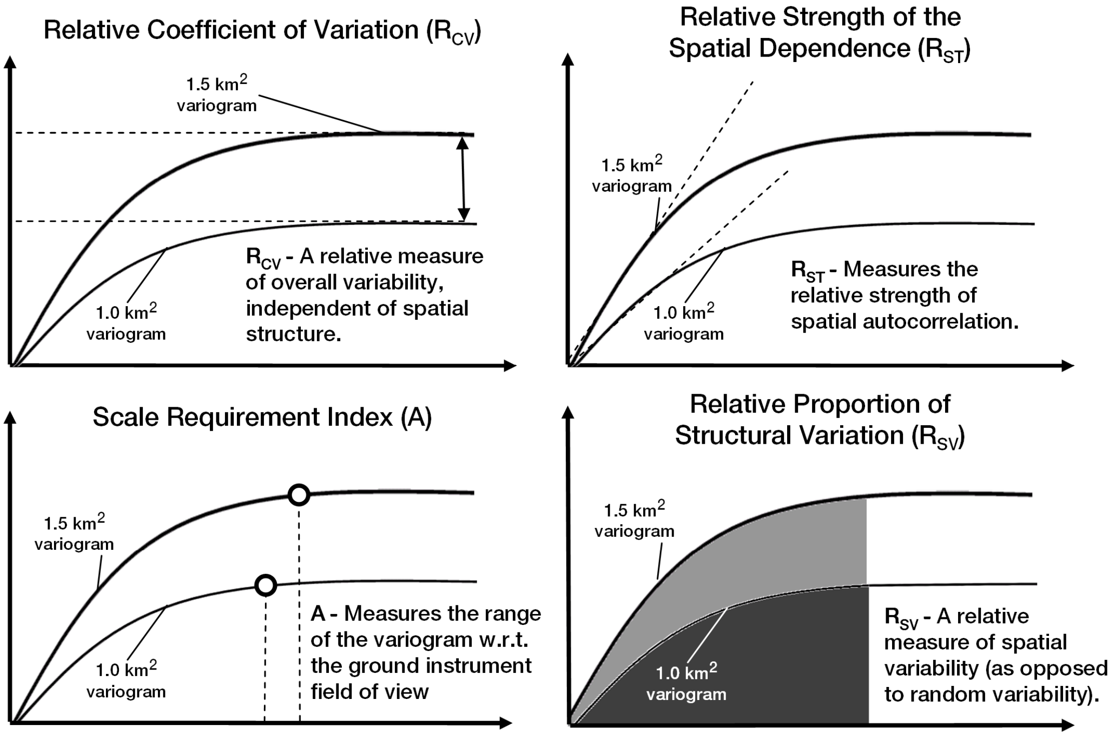

Figure 2.5. The geostatistical attributes of spatial representativeness can be used to describe the overall variability, spatial extent, strength, and temporal structure of surface albedo patterns for a given site. These measures improve our understanding of product uncertainty both in terms of the representativeness of the field data and its relationship to the larger MODIS pixel.

2.5.2.1. Relative Coefficient of Variation - R_{CV}

The coefficient of variation (CV) is defined by the ratio of the standard deviation to the mean. It is a useful measure of the relative spread in the data and provides an estimate of overall variability that is independent of spatial scale. A good way to utilize this measure, for the purposes of this study, is to measure the change in CV as a function of increased field of view. Accordingly, we now define the relative coefficient of variation (R_{CV}):

$$\mathrm{R}_{\mathrm{CV}} = \frac{CV_{1.5x} - CV_x}{CV_x};\ x = 1.0km \tag{2.17}$$

R_{CV} is the difference between two major terms: (1) CV_x, which is the coefficient of variation obtained from a 1 km^2 ETM+ albedo subset that is centered on a given measurement site; and (2) $CV_{1.5x}$, which is the coefficient of variation obtained over a footprint that is 1.5 times the size of CV_x (1.5 km^2). If a measurement site is spatially representative, then the overall variability between the internal components of the measurement site and the adjacent landscape should be similar in magnitude and R_{CV} should approach zero. Conversely, a large positive or negative value for R_{CV} would correspond to higher variance within the 1 km^2 area immediately surrounding the tower than the larger 1.5 km^2 area. The sign of R_{CV} thus provides a first-order estimate of the primary sources that drive the overall variability, i.e. negative for internal variations associated to CV_x and positive for external variations associated to $CV_{1.5x}$. Note that R_{CV} decreases systematically with sample mean (Downing 1991). By providing measures relative to their areal mean value, comparisons at different spectral ranges (e.g. VIS 0.3-0.7 μm and NIR 0.7- 5.0 μm) or between other vegetation parameters (e.g. NDVI, LAI, and LST), will produce comparable measures of overall variability. Figure 2.6 shows eight ETM+ subsets, each of them with a close-up image that shows the circular footprint of each tower and their respective 1.0 km^2 and 1.5 km^2 boundaries. Results for R_{CV} for each of these cases, and all other study locations, are summarized on Table 2.2. Figure 2.7 also shows the corresponding semivariogram functions using 1.0 km^2, 1.5 km^2, and 2.0 km^2 albedo subsets. This work focuses on the use of variogram functions over the spatial scales of MODIS observations. Thus, geostatistical attributes like R_{CV}, are defined by information extracted from variograms functions in the range of 1.0 – 1.5 km^2. Nonetheless, we have preserved the variogram responses using 2.0 km^2 subsets on Figure 2.7 to further demonstrate the utility of this technique for analyses at other spatial scales.

The first two rows, on Figure 2.6 and Figure 2.7, show a selection of UCI sites that are a chronological series of stations representative of secondary succession growth stages after large stand replacement fires. Black spruce trees undergo a slow growth process enabling the accurate determination of the chronosequence of stand age disturbance (Goulden et al. 2006). Additionally, boreal forests make up approximately 25% of forest ecosystems on Earth. With both of these in mind, the UCI sites provide an excellent location to study the impacts of surface albedo as a function of sequential wildfires.

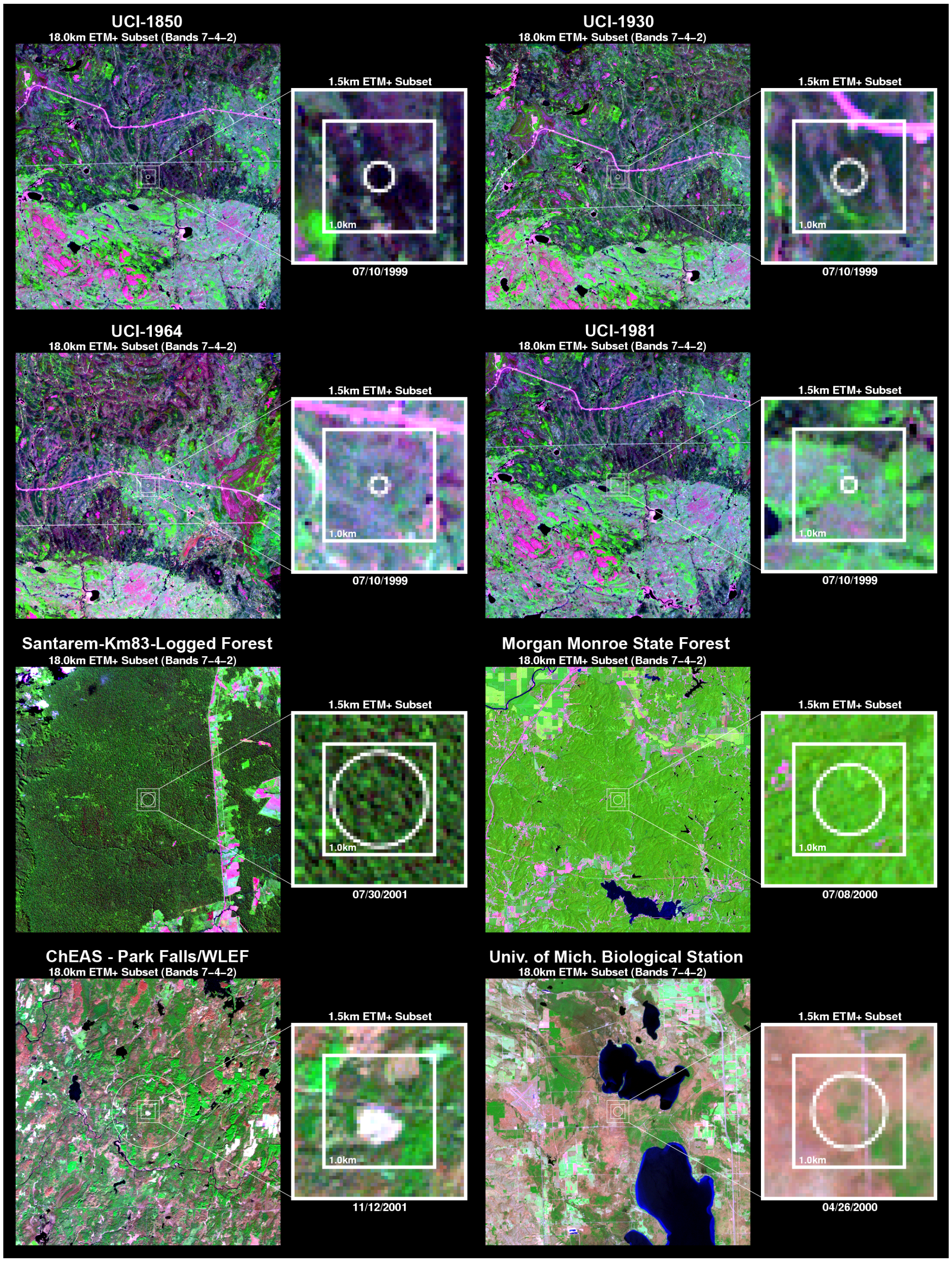

Figure 2.6. Top-of-Atmosphere (TOA) shortwave reflectance composites (ETM+ Bands 7-4-2) centered over a select number of AmeriFlux stations. Trees are in shades of green (both light and dark tones) and purple, bare areas are seen in light-pink, light-lavender, magenta, and pale-pink, and water is seen in dark-blue and black.

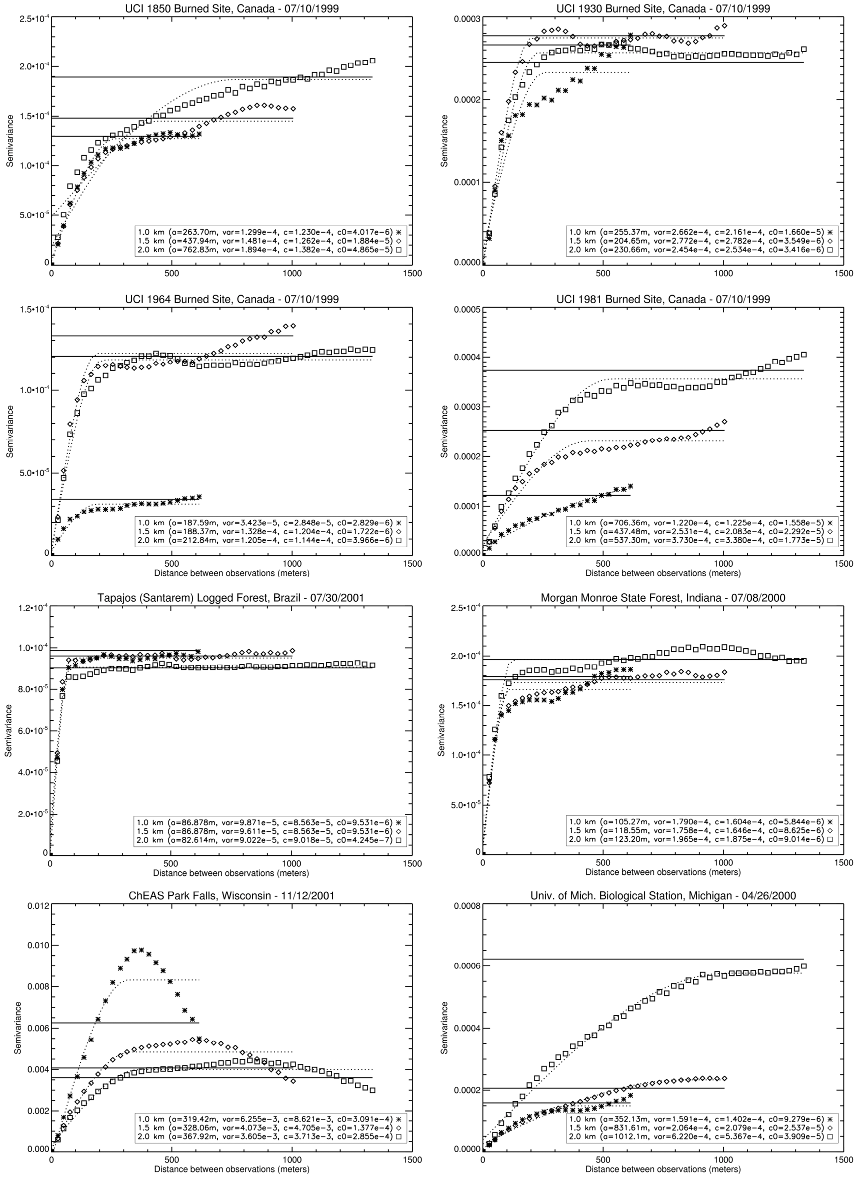

Figure 2.7. Variogram estimator (points), spherical model (dotted curves), and sample variance (solid straight lines), obtained over the AmeriFlux sites presented in Figure 2.6, using squared areas of 1.0 km (asterisks), 1.5 km (diamonds), and 2.0 km (squares). The point values of the variogram estimators for each of the squared areas are more closely aligned over shorter separation distances than for longer ones. When measurement sites are spatially uniform at increased scales, (e.g. Santarem Km-83 and Morgan Monroe State Forest) the three spatial subsets reach an asymptote near the sample variance.

Table 2.2. Geostatistical attributes of spatial representativeness from field measurements used from the network-wide AmeriFlux database.

Site Name	**ETM+ Overpass Time**	**Seasonal Period**	**Ground Footprint**	**1 km Range***	**1.5 km Range***	**R_{CV}***	***A****	**R_{ST}***	**R_{SV}***
Santarem-Km83	30-Jul-01	Leaf-On	820.80m	161.15m	693.28m	-1.86%	0.00%	4.21%	5.48%
	22-Nov-02	Leaf-Off		111.93m	101.84m	-4.95%	0.00%	0.04%	0.00%
UCI-1850 Burn Site	10-Jul-99	Leaf-On	252.60m	263.70m	437.94m	3.79%	32.70%	6.79%	60.05%
	7-Oct-00	Leaf-Off		129.47m	177.40m	-2.47%	8.94%	-2.34%	10.32%
UCI-1930 Burn Site	10-Jul-99	Leaf-On	277.80m	255.37m	204.65m	-1.06%	17.56%	32.26%	-19.04%
	7-Nov-02	Leaf-Off		214.17m	251.93m	13.77%	18.22%	84.97%	12.93%
UCI-1964 Burn Site	10-Jul-99	Leaf-On	151.50m	187.59m	188.37m	90.82%	31.98%	303.62%	1.48%
	7-Nov-02	Leaf-Off		305.88m	172.59m	35.84%	36.49%	108.86%	-44.17%
UCI-1981 Burn Site	10-Jul-99	Leaf-On	126.30m	703.36m	437.48m	48.28%	71.21%	50.80%	-23.73%
	7-Nov-02	Leaf-Off		503.31m	627.49m	23.85%	64.00%	55.32%	0.32%
Flagstaff-Managed	6-Jun-00	Leaf-On	290.43m	203.55m	210.37m	4.31%	13.73%	14.72%	18.40%
	11-Nov-99	Leaf-Off		183.65m	211.49m	11.45%	12.31%	27.06%	13.62%
Flagstaff-Unmanaged	6-Jun-00	Leaf-On	290.43m	164.64m	342.11m	21.28%	17.23%	63.97%	141.27%
	11-Nov-99	Leaf-Off		178.60m	433.58m	21.11%	14.11%	35.31%	85.31%
Morgan Monroe	8-Jul-00	Leaf-On	606.10m	105.27m	115.55m	0.03%	0.05%	3.46%	-4.60%
	21-Dec-02	Leaf-Off		141.18m	172.78m	3.82%	0.39%	-7.08%	14.49%
Harvard Forest	8-Sep-02	Leaf-On	378.83m	261.79m	286.18m	12.98%	14.07%	26.71%	11.19%
	26-Dec-01	Leaf-Off		387.90m	345.04m	24.53%	23.00%	35.06%	-6.78%
Howland Forest	2-Jul-00	Leaf-On	378.83m	568.69m	898.67m	22.59%	45.46%	94.08%	57.94%
	2-Mar-02	Leaf-Off		842.54m	1013.10m	21.97%	55.72%	114.78%	99.51%
UMBS	30-Jul-02	Leaf-On	631.40m	436.84m	1125.80m	21.27%	21.22%	99.71%	113.92%
	26-Apr-00	Leaf-Off		352.13m	831.61m	14.17%	14.26%	70.94%	133.87%
Ozark Site	6-Sep-00	Leaf-On	378.83m	231.94m	291.25m	6.39%	9.57%	3.92%	-2.34%
	7-Nov-99	Leaf-Off		225.35m	231.46m	-5.22%	12.39%	22.56%	-11.34%
Bartlett Forest	26-Aug-00	Leaf-On	315.69m	127.71m	499.20m	29.61%	7.80%	96.08%	201.91%
	27-Sep-00	*Senescence*		102.00m	185.00m	28.46%	2.96%	59.79%	54.77%
	20-Oct-00	Leaf-Off		192.73m	288.72m	18.42%	13.36%	39.47%	22.16%
Chestnut Ridge	10-Sep-99	Leaf-On	378.83m	389.26m	475.42m	23.14%	8.08%	38.68%	22.80%
	1-Dec-00	Leaf-Off		359.61m	404.06m	-0.90%	5.96%	-10.29%	4.51%
Walker Branch	10-Sep-99	Leaf-On	416.71m	185.35m	254.07m	17.21%	3.43%	41.28%	23.01%
	1-Dec-00	Leaf-Off		233.65m	307.37m	8.99%	6.61%	27.04%	37.92%
WLEF-ChEAS	26-May-03	Leaf-On	5000.50m	316.89m	354.96m	-10.54%	0.00%	-34.09%	5.52%
	12-Nov-01	Leaf-Off		319.42m	328.06m	-17.21%	0.00%	-48.01%	-4.12%

The first row on Figure 2.6 shows results for the UCI-1850 and UCI-1930 sites. These stations are surrounded by closed canopies of tall black spruce, nearly 100% feather moss cover, and an open understory with a few alders, Labrador tea, and willow (McMillan and Goulden 2008). As we varied the size of the ETM+ footprint from 1– 1.5 km, R_{CV} increased by 3.79% over UCI-1850 and decreased slightly by -1.06% over UCI-1930. These are reasonably stable changes associated with smaller landscape components in the contiguous regions. Note that a small road circumvents the northeastern section of UCI-1930 and just about crosses the boundary of the 1 km subset. Since both the internal (CV_{1km}) and external ($CV_{1.5km}$) regions include this road, its effect on the overall variability is negligible, hence the low value for R_{CV}. A similar degree of overall stationarity between regions was also found at the Morgan Monroe State Forest (MMSF), where R_{CV} increased slightly by 0.03%. This station is located over a secondary successional broadleaf forest within the maple-beech to oak hickory transition zone of the eastern deciduous forest, and is dominated by 60-80 year-old deciduous trees (e.g. sugar maple, tulip poplar, sassafras, white oak, and black oak) that have survived a selective logging period that ended over the past 10 years (Schmid et al. 2002).

The second row on Figure 2.6 and Figure 2.7 shows the UCI-1964 and UCI-1981 stations. These sites are surrounded by stands of smaller 2.0–7.0 m tall jack pine and aspen, various 1.0– 6.0 m tall black spruce trees, and ground cover of feather moss with sparse grass. As we increased the size of the footprint from 1– 1.5 km, R_{CV} increased by 90.82% over UCI-1964 and by 48.28% over UCI-1981. Unlike the older stations (UCI-1850 and UCI-1930), which have denser and taller canopies that extend beyond the 1 km limit, the contiguous regions surrounding UCI-1964 and UCI-1981 significantly differ from their internal footprint. Notice that the network of small roads that surrounds UCI-1964 is not being captured by the internal boundary of the 1 km subset, hence the large positive values for R_{CV}. The same issue applies to UCI-1981, which is externally exposed to lake water (and thus, lower albedos) on the west side of the measurement site.

2.5.2.2. Scale Requirement Index - *A*

While it is very challenging to resolve the footprint of a measurement site, it is essential to provide a measure of the range (*a*) of surface albedo with respect to both the ground instrument's field of view and its surrounding landscape. In principle, surface albedo retrievals that are sampled at distances greater than the range can be treated as spatially independent and can consequently be applied in direct assessments between ground measurements and MODIS retrievals (Susaki et al. 2007). Accordingly, we now define the scale requirement index (*A*):

$$A = \exp\left[-\sqrt{\left(\frac{g}{a_x}\right)^2 + \left(\frac{g}{a_{1.5x}}\right)^2}\right];\ x = 1.0\,km \qquad (2.18)$$

where

$$g = 2H\tan\left(FOV^\circ\right) \qquad (2.19)$$

a is the range of two ETM+ subsets of sizes *x* and 1.5*x* [m], *H* [m] is the height of the field albedometer, and *FOV* [degrees] is its field of view. In general, the three albedometer models used in this study all have nominal directional errors of 10% (or a

FOV = 81°). Measurement sites that are spatially representative would have values for *A* between [0.0– $e^{-\sqrt{2}} \approx$ (24.3%)], which would be the case for stations that cover a large circular footprint and have small and stable range parameters (i.e. $g \geq a_x$ and $g \geq a_{1.5x}$).

Results for *A* for each of the cases illustrated on Figure 2.6 and Figure 2.7, and all other study locations, are summarized on Table 2.2. At 396.0 m in height, the WLEF-ChEAS Park Falls tall tower has the largest instrument footprint of all the study sites. In the vicinity of the station, the forest is predominantly classified by a really mixed landscape, with 70% deciduous trees, including aspen, birch, maple, basswood, alder, and 30% conifers, including balsam fir, jack pine, black spruce, and white cedar. Upland areas are occupied by broadleaf deciduous and coniferous tree species, while the lowlands areas are occupied by tree species, shrubs, and a variety of grass and sedges. A further examination of the scale requirement index (*A*) using five ETM+ scenes over the ChEAS site, with overpass periods during 17 March, 2001, 8 April, 2003, 26 May, 2003, 12 September, 2002, and 12 November, 2001, resulted in all *A* values < 0.1%. These results suggest that a direct assessment between ground-based estimates and MODIS retrievals over the ChEAS site will be suitable throughout the seasons. A similar trend was also found at the Tapajos National Forest (TNF) KM83-Logged station, where *A* < 0.1%. This station was categorized as a closed tropical forest with canopy emergents (canopy height = 35–40 m) from flat, upland terrain (Hernandez-Filho et al. 1993). However, the site was selectively logged in September 2001, thus, the ground records available were made prior (while the forest was still considered old growth) and after the logging. The forest extended 5 km to the east, 8 km to the south, and 40 km to the north before reaching pasture (Miller et al. 2004), hence the low value for *A*.

The ground footprints of UCI-1850 and UCI-1930 are almost double the size of the younger stations (UCI-1964 and UCI-1981). It has been a common guideline among field programs to install tower albedometers at reasonable heights above the canopy (Loescher and Munger 2006). Since the tallest trees at UCI-1964 and UCI-1981 extend to no more than 7.0 m, the stations were consequently instrumented at much lower heights (10 – 12m). This arrangement constrains measurement of the surrounding landscape extending to a MODIS pixel. A spatial footprint analysis is even more challenging at UCI-1981, where the range of the measurement site varied from 437.48– 703.36 m. On the other hand, a slight increase in the instrument's height at UCI-1964, from 12 to 15 m, would be sufficient to decrease the value of *A* and capture the range over the measurement site.

2.5.2.3. Relative Strength of the Spatial Dependence - R_{ST}

Another good indicator of spatial variability is the strength of spatial dependence over the range (*SD*) (Cooper et al. 1997):

$$SD = \frac{\gamma_E(a) - c_0}{\gamma_E(h)_{\max}} \tag{2.20}$$

This quantity measures the slope of the ascending limb of the variogram estimator after standardizing the semi-variance by dividing through by its maximum value. By standardizing the semivariance before calculating the slope, we obtain a measure that depends on the range (*a*) and the nugget variance (c_0) (Cooper et al. 1997; Dent and Grimm 1999). In using *SD* as an indicator of spatial representativeness, our goal is to assess whether the primary source(s) that drive the spatial variability can be properly categorized as either leaning towards or away from the center point of each ETM+ subset (i.e. the measurement site). Accordingly, we now define the relative strength of the spatial dependence (R_{ST}):

$$R_{ST} = \left[\frac{ST_{1.5x} - ST_x}{ST_x} \right] \; ; \; x = 1.0\,km \tag{2.21}$$

where,

$$ST = \frac{\gamma_E(a) - c_0}{\gamma_E(a) - \gamma_E(0)} \tag{2.22}$$

Unlike *SD*, R_{ST} provides a spatially-explicit representation of where the most different source(s) of albedo variability (e.g. lakes, small ponds, clear-cuts, and bare areas) are likely to be situated with respect to the measurement site. Thus, a negative value for R_{ST} can be attributed to internal outliers associated to ST_x, whereas positive values are attributed to external outliers associated to $ST_{1.5x}$. Results for R_{ST} for each of the cases illustrated on Figure 2.6 and Figure 2.7 and all other study locations, are summarized on Table 2.2

At the University of Michigan Biological Station (UMBS) (Figure 2.6 and Figure 2.7, fourth row), results for R_{ST} show a very positive trend (70.94%). This station lies on lake-border plains in northern Lower Michigan, in the transition zone between mixed hardwoods and boreal forests. In the vicinity of the tower (within a 1 km radius), the forest canopy is predominantly bigtooth aspen and trembling aspen, but with significant representation by red oak, beech, sugar maple, white pine, and hemlock as well. The understory is dominated by bracken fern and saplings of red maple, red oak, beech, and white pine (Curtis et al. 2002). Looking closely at the semivariogram functions over UMBS (Figure 2.7), we can notice that the slope of the ascending limb at the 1.5 km threshold is slightly sharper than that of the 1 km subset. The primary source region that drives the strength of the variability can be attributed to a group of early greened-up trees and conifer stands that are spread about ~1.0 km southeast of the UMBS tower. For this particular ETM+ overpass (26 April, 2000), this sector appeared to have much darker albedos than the relatively dormant regions surrounding the station. An even more pronounced change in the strength of the variability can be observed at the 1.5 km to 2.0 km spatial threshold. However, unlike 1.0 km vs. 1.5 km case, these external differences of albedo are linked to the presence of lake water in the northeastern corner of the 2.0 km region.

2.5.2.4. Relative Proportion of Structural Variation - R_{SV}

Li and Reynolds (1995) introduced the proportion of structural variation:

$$SH = \frac{c - c_0}{c} \tag{2.23}$$

SH is a measure that describes the amount of landscape variability that is attributable to spatial (as opposed to random) effects. This measure can be obtained by subtracting the semivariogram nugget (c_0) from the sill (c) and then dividing by the sill. Since the sill represents the maximum (overall) variation, and the nugget represents pure random variation, subtracting both terms results in a measure of spatially-correlated variation. In order to provide a relative measure of structural variability, we have measured the relative change in *SH* as a function of increased field of view:

$$\mathrm{R}_{\mathrm{SV}} = \left[\frac{SV_{1.5x} - SV_x}{SV_x} \right] ;\; x = 1.0\,km \tag{2.24}$$

where,

$$SV = \int_0^a \left(\frac{\gamma_E(h) - c_0}{c} \right) dh \tag{2.25}$$

The relative proportion of structural variation (R_{SV}), is a function of the range (a), nugget (c_0), sill (c), and the variogram estimator ($\gamma_E(h)$). R_{SV} is also dependent on separation distance (h), which allows for a full depiction of spatial patterns that may emerge at distances smaller than the range.

Results for R_{SV} for each of the cases illustrated on Figure 2.6 and Figure 2.7, and all other study locations, are summarized on Table 2.2. Note that large positive values for R_{SV} are present over measurement sites where more patches or clumps of trees and bare areas are observed when measuring the surrounding landscape extending to a 1.5 km pixel. For example, by increasing the spatial footprint at the UCI-1850 site, the southwestern region merged with a green patch consisting of a combination of wetlands and/or an aspen grove. Both wetlands and aspen are deciduous covers which, in this particular region, reflects strongly in the NIR (0.7 – 5.0 μm). At UMBS, a cluster of early greened-up trees, just southeast of the station, also increased in size. These results suggest that R_{SV} can detect spatial patterns that go against the overall trends captured by R_{CV}.

By examining a measurement site at several time periods, R_{SV} can further identify how changing spatial patterns, within and across the landscape, are affecting the structural variability of a given measurement site. Thus, in using R_{SV} as an indicator of spatial representativeness, our goal is to resolve the relative magnitude of change patterns at different seasonal periods throughout the year.

Figure 2.8 shows ETM+ subsets over the Bartlett Experimental Forest for three time periods that illustrate seasonal variations of greenness (26 August, 2000), to early senescence (27 September, 2000), and dormancy (20 October, 2000). The Bartlett Experimental Forest is located within the White Mountain National Forest in north-central New Hampshire, USA. At low- to mid-elevations, vegetation is dominated by northern hardwoods (American beech, sugar maple, and yellow birch), with some red maple and paper birch also present. Conifers (eastern hemlock and eastern white pine) are occasionally found intermixed with the more abundant deciduous species but are generally confined to the lowest elevations and across the edges of the Albany Brook tributary, which crosses just west of the measurement site. In the vicinity of the tower, the forest is predominantly red maple, sugar maple, and American beech forest types (Jenkins et al. 2007).

The three ETM+ subsets in Figure 2.8 illustrate how the effects of the fall foliage can significantly affect the structural variability of the observed landscape. Notice that both the internal and external footprints of the Bartlett measurement site are covered by bare areas, caused by experimental clearcuts, as shown in light-pink patches. As the landscape entered into dormancy, these areas began to gradually merge with the fully dormant tree regions. Consequently, both R_{CV} and R_{SV} decreased as the landscape entered into dormancy. However, the magnitude of the change in R_{SV} (179.75%) was much larger than that of R_{CV}, (11.19%). These results suggest that R_{SV} was able to resolve the reduction in within-biome variability between the already existing bare areas and the now fully dormant trees.

A closer look at the variogram functions on Figure 2.8 also show that the range resolved at the 1 km limit was more stable (160 ± 33 m), throughout this 55-day period, than the 1.5 km subset (384 ± 115 m). Thus, the degree of "patchiness" – as indicated by the presence of distinct patches between trees and bare areas – was much stronger in the immediate region surrounding the measurement site.

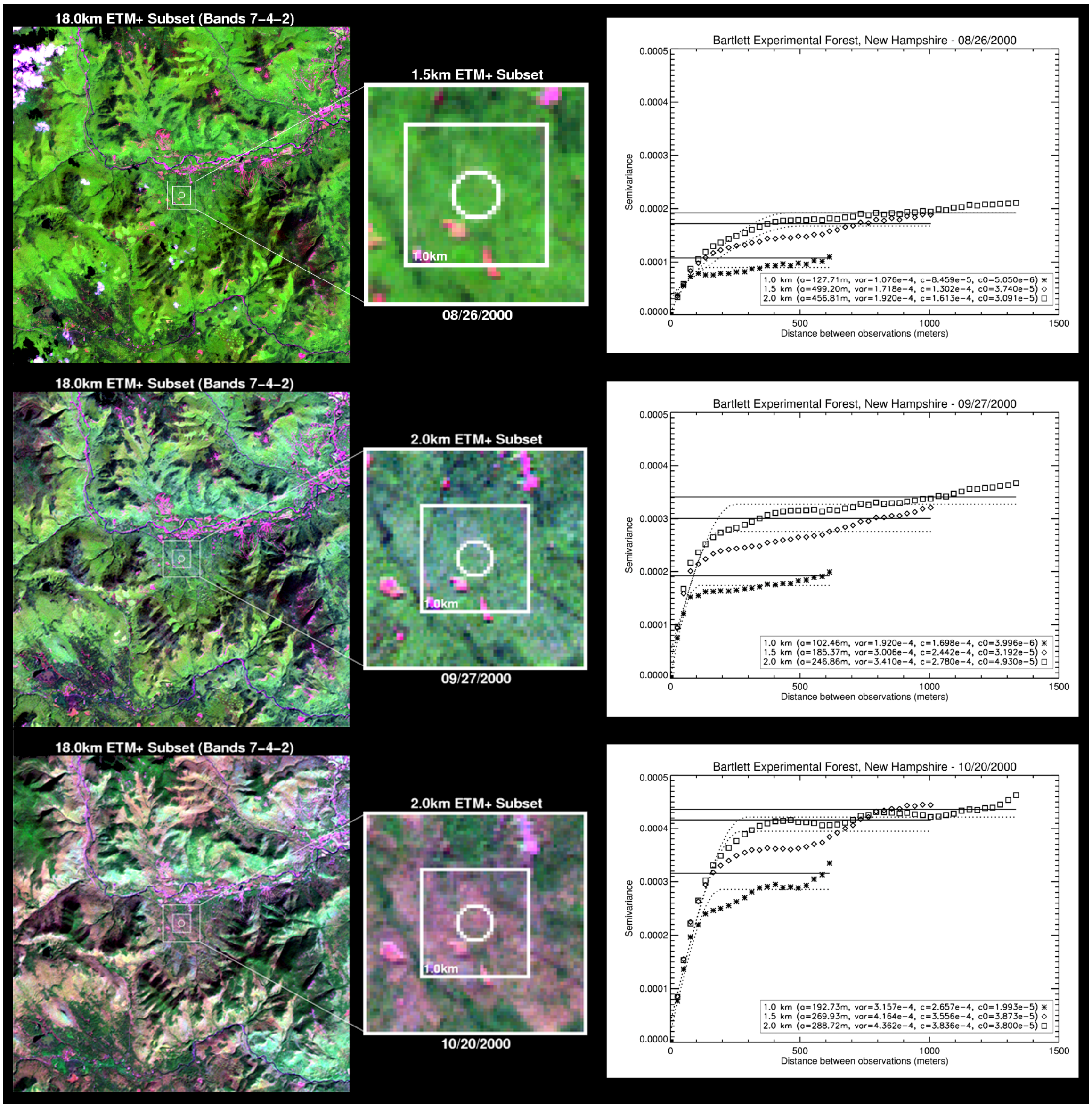

Figure 2.8. Top-of-Atmosphere (TOA) shortwave reflectance composites (ETM+ Bands 7-4-2), and the corresponding semivariogram functions, centered over Bartlett Experimental Forest for three time periods, illustrating conditions of greenness (26 August, 2000), early-senescence (27 September, 2000), and dormancy (20 October, 2000). Trees and bushes are in shades of green (both light and dark tones) and bare areas are seen in light-lavender, magenta, and pale-pink. Results for each geostatistical attribute (i.e. R_{CV}, *A*, R_{ST}, and R_{SV}) are presented on Table 2.2.

2.6. Validation Results and Discussion

Figure 2.9 to Figure 2.12 show a number of plots that evaluate the daily performance of the MODIS V005 BRDF/Albedo product (MCD43A3) against coincident ground data. Each figure has been divided into pairs of measurement sites that are in close proximity to each other and share the same multi-year retrieval periods. For each time series plot, the dark points with error bars are daily retrievals of surface albedo. These values were derived by calculating the mean and standard deviation of all ground retrievals available within a 2 hour window centered at Local Solar Noon (LSN). Ground retrievals with large error bars are linked to intra-daily variations in downwelling irradiance, usually resulting from periods of increased cloudiness. Since the MODIS V005 BRDF/Albedo product is routinely used as a clear-sky product, we have removed daily ground albedo records when estimates of cloud fraction were detected to be > 0.75.

The blue circles and red triangles, on the time series plots, indicate snow-free blue-sky albedo retrievals at LSN derived from MCD43A3 using the main (full-inversion) and backup algorithms, respectively. The blue and red asterisks, on Figure 2.11 and Figure 2.12, indicate snow-covered retrievals, as indicated by the snow flag in the MODIS V005 albedo product embedded QA (MCD43A2), using the main and backup algorithms, respectively. A series of scatter plots, located at the center of each figure, evaluate the daily blue-sky albedos from MCD43A3 against field measurements using four seasons: January-February-March (JFM) in blue, April-May-June (AMJ) in green, July-August-September (JAS) in red, and October-November-December (OND) in yellow. MODIS data from full inversion retrievals (in open shapes) were also separated from the “Full + Magnitude” inversion cases (in asterisks) to investigate the inversion quality differences when both methods are applied. The solid line is the one-to-one line and the dashed lines are ±0.02 and ±0.05 units. The statistical results for the absolute error (i.e. $\text{Ground}_{\text{mean}} - \text{MODIS}_{\text{mean}}$) and RMSE values calculated for the entire multi-year retrieval period are also displayed for each scenario (i.e. Full / Full+Magnitude). Table 2.3 provides summary statistics (RMSE values of Full / Full+Magnitude retrievals) for each seasonal class, plus a final assessment combining all data records from all measurement sites.

The daily retrievals from MCD43A3 agreed closely with the daily albedos over broadleaf forests, such as the Oak Ridge sites, Chestnut Ridge and Walker Branch (Figure 2.9) as well as evergreen needleleaf forest sites, such as the Flagstaff stations (Figure 2.10) and the UCI sites (Figure 2.11 and Figure 2.12). At the Oak Ridge forest sites, surface albedo was stable throughout the seasons, with consistently small peaks reached throughout the dry “snow-free” winter periods of 2006-2007. MODIS albedos were usually within ±16.5% of the ground measured seasonal average albedo during the spring and summer periods, and within ±17.0% during the fall and winter. Both the Walker Branch and Chestnut Ridge towers are located on one of East Tennessee’s long parallel ridges about 5 km away from each other.

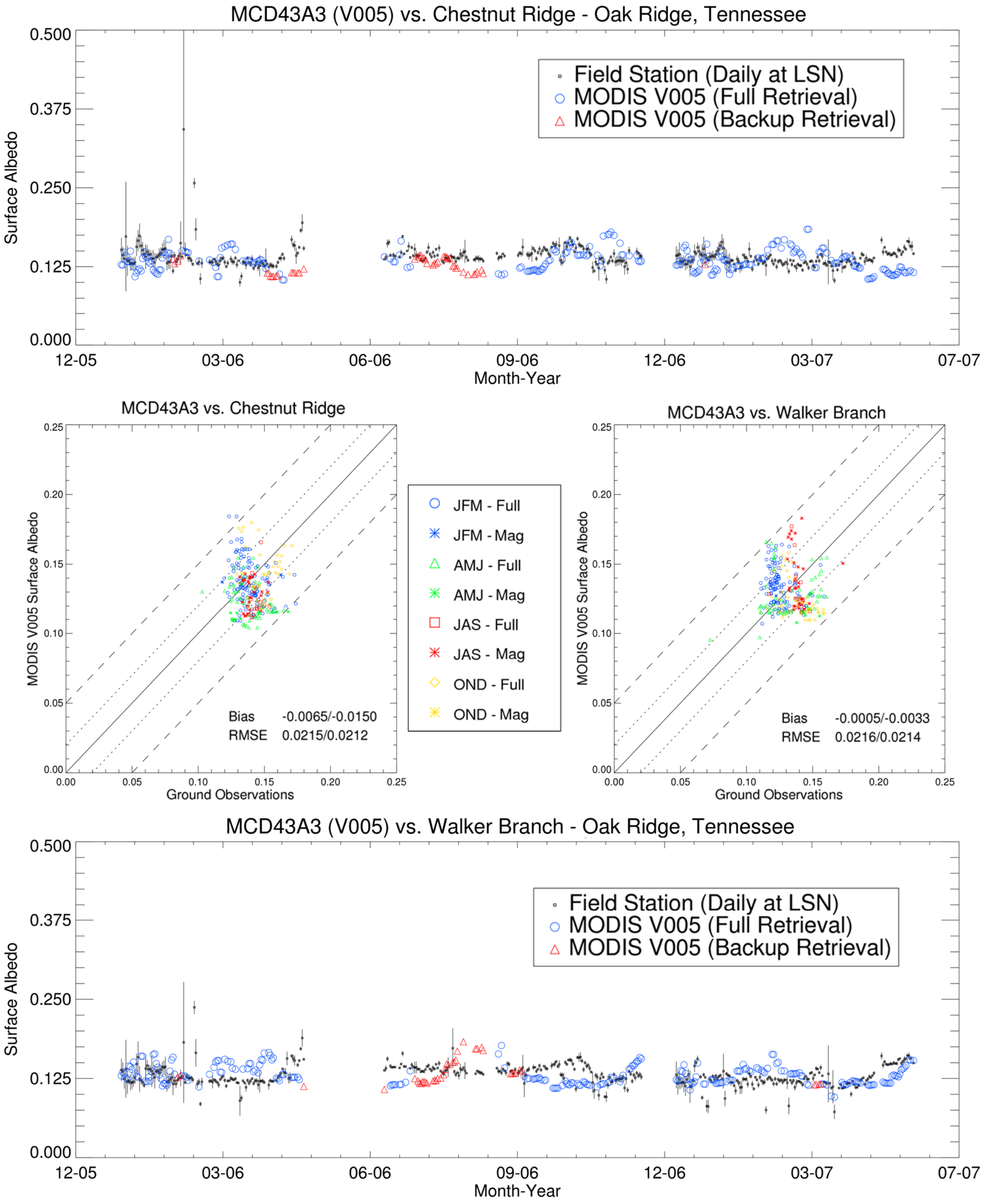

Figure 2.9. Time series of surface albedo at LSN for the Chestnut Ridge (above) and Walker Branch (below) stations during years 2006 and 2007. Two scatter plots (center) evaluate the daily blue-sky albedos from MCD43A3 against the Oak Ridge measurement sites using four seasons. The solid line is the one-to-one line and the dashed lines are ±0.02 and ±0.05 units. MODIS data from full inversion retrievals (in open shapes) were also separated from the "Full + Magnitude" inversion cases (in asterisks). The statistical results for the absolute bias and RMSE values are also displayed for each scenario (i.e. Full / Full+Magnitude).

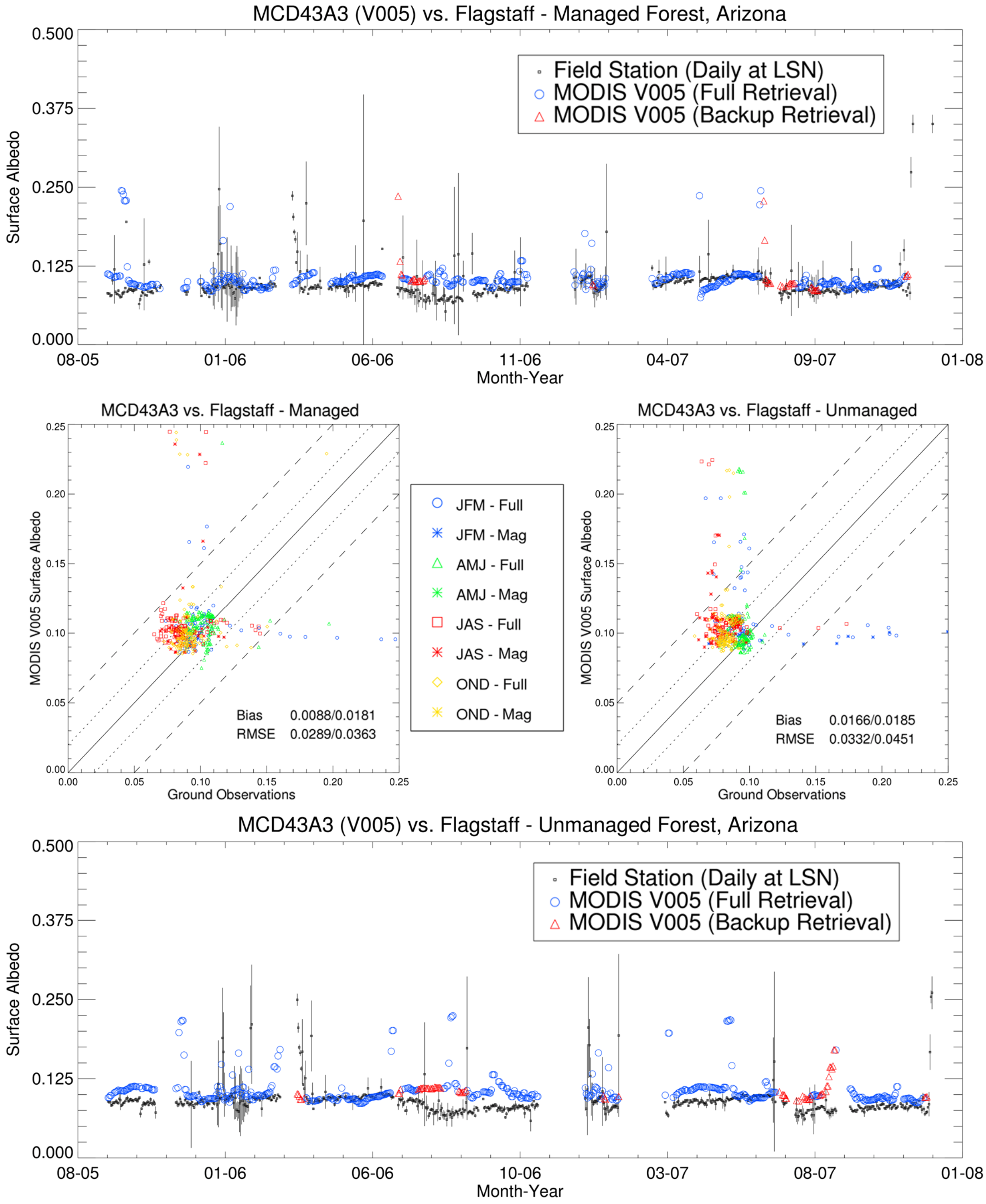

Figure 2.10. Time series and scatter plots of surface albedo at LSN for the Flagstaff Managed (above) and Unmanaged (below) stations from late 2005 to late 2007. Setup is the same as Figure 2.9.

The Flagstaff sites, located within Northern Arizona University's Centennial Forest, consist of a densely forested unmanaged site and a similar managed site that was partially restored to historical stand density conditions using mechanical thinning in September 2006 (Finkral and Evans 2008; Sullivan et al. 2008). The Flagstaff sites, located within Northern Arizona University's Centennial Forest, consist of a densely forested unmanaged site and a similar managed site that was partially restored to historical stand density conditions using mechanical thinning in September 2006 (Finkral and Evans 2008; Sullivan et al. 2008). The Flagstaff-Unmanaged (or control) site represents a typical dense ponderosa pine stand in northern Arizona, and has not experienced forest management in over a century. The Flagstaff-Managed site is located about 6.7 km north from the control site. The latter site was mechanically thinned in September 2006, reducing tree density by 67% (Finkral and Evans 2008; Sullivan et al. 2008).

MODIS albedos at the Flagstaff sites were usually within ±22.5% of the ground measured seasonal average albedo during the spring and summer periods, and ±28.0% during the fall and winter. Daily retrievals over the Flagstaff Managed site did not show a change in surface albedo associated with the thinning in September 2006. A comparison of the MODIS retrievals at the control site also denoted a consistent divergence from the ground measurements on both stations. The underling variations throughout this period were most likely caused by periods of increased cloudiness during the Arizona Monsoon. MODIS albedos were often greater than ground-measured albedos during the cloudy and rainy monsoon season (July through September). Since the MODIS V005 BRDF/Albedo product is routinely used as a clear-sky product, long-term periods of increased cloudiness usually cause an overestimation of the albedo. This happens because only a few number of retrievals obtained prior to the rain season were used to describe the underlying reflectance anisotropy, and thus the albedo, of subsequent periods. The MODIS algorithm performed much better during the same period in 2007, particularly over the Flagstaff Managed Forest station, where a series of full and backup retrievals followed the sudden dips in surface albedo.

The MODIS algorithm also performed well throughout the seasons at the UCI sites (Figure 2.11 and Figure 2.12). MODIS albedos were usually within ±16.5% of the ground measured seasonal average albedo during the spring and summer periods and within ±21.2% of the ground measured seasonal average albedo during the spring and summer periods. Over these older stations (UCI-1850 and UCI-1930), the percent tree cover was at least ~15% higher than the younger UCI-1964 and UCI-1981 sites. These marked differences in tree density had a significant effect in the magnitude of the albedo throughout the three recorded periods of snow-cover (i.e. 2002-2004). For instance, MODIS albedos over the older UCI sites remained under 0.25 throughout snow periods, while the younger UCI-sites reached a peak albedo of 0.45. Snow-cover periods were also consistently shorter, by 20-30 days, at the older UCI-sites. Thus, it appears that snow had less of an effect on albedo in the more mature forests.

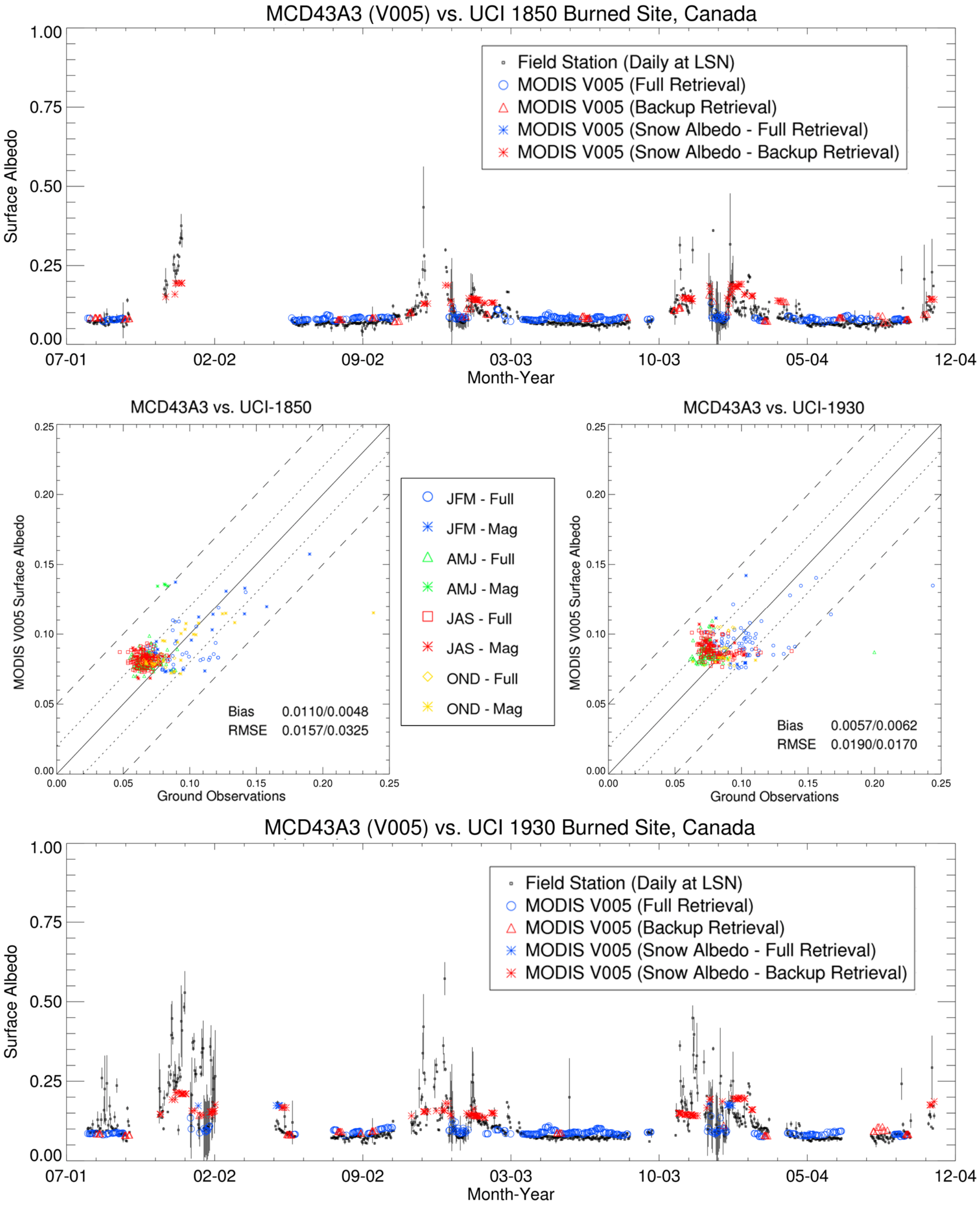

Figure 2.11. Time series and scatter plots of surface albedo at LSN for the UCI-1850 (above) and UCI-1930 (below) stations from late 2001 to late 2004. Setup is the same as Figure 2.9. In addition, the blue and red asterisks indicate snow-covered retrievals using the main and backup algorithms, respectively.

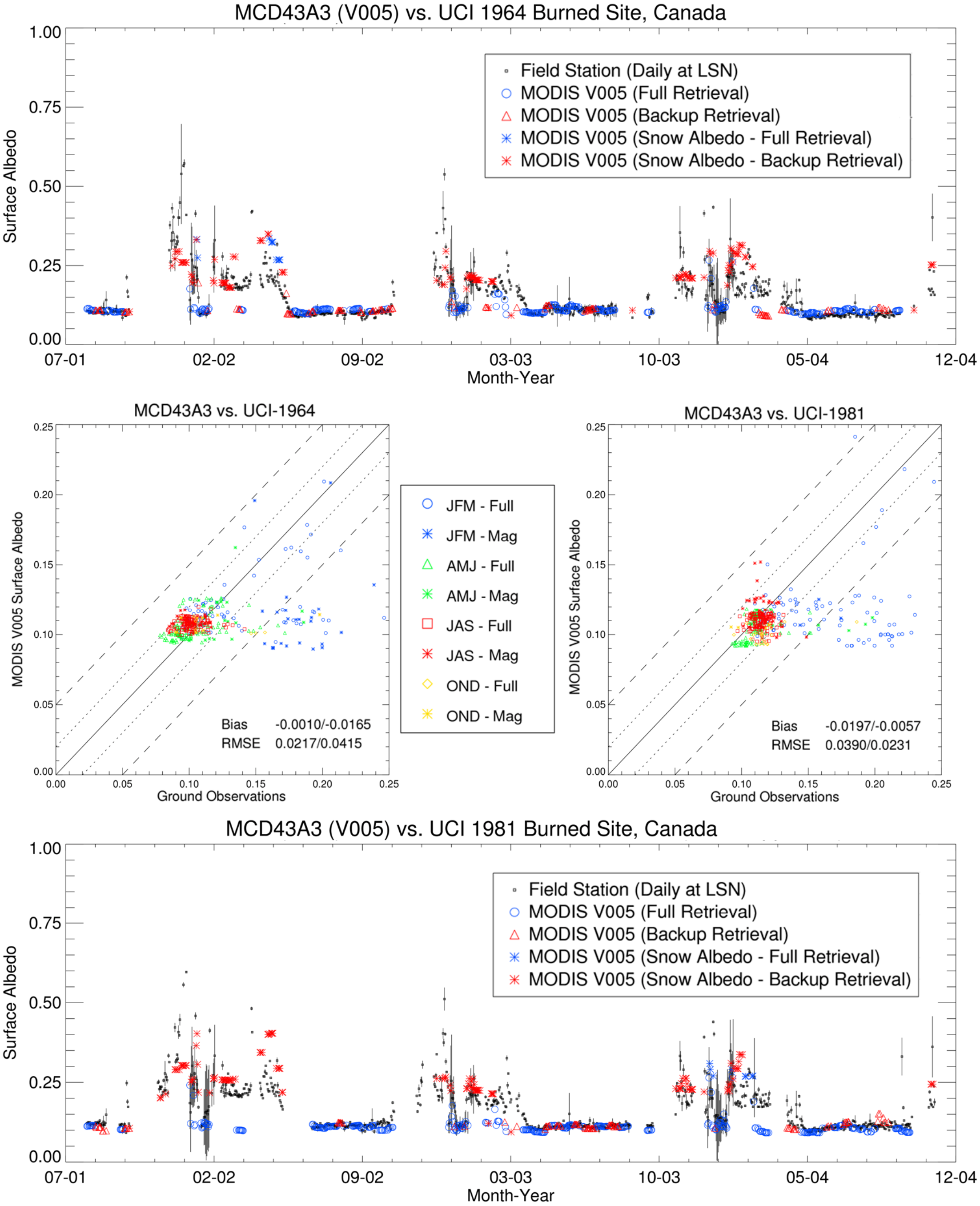

Figure 2.12. Time series and scatter plots of surface albedo at LSN for the UCI-1964 (above) and UCI-1981 (below) stations from late 2001 to late 2004. Setup is the same as Figure 2.9. In addition, the blue and red asterisks indicate snow-covered retrievals using the main and backup algorithms, respectively.

Table 2.3. RMSE (Full/Full+Mag) between field-measured albedos at LSN and MODIS V005 albedos (MCD43A3) sites, using the SWIR (0.3-5.0μm) broadband, for four seasonal classes: January-February-March (JFM), April-May-June (AMJ), July-August-September (JAS), and October-November-December (OND).

Field Station	**JFM**	**AMJ**	**JAS**	**OND**
Santarem-Km83	0.0675/0.0695	0.0368/0.0387	0.0264/0.0300	0.0143/0.0364
UCI-1850 Burn Site	0.0170/0.0179	0.0148/0.0178	0.0165/0.0168	0.0091/0.0390
UCI-1930 Burn Site	0.0231/0.0234	0.0171/0.0165	0.0161/0.0162	0.0117/0.0126
UCI-1964 Burn Site	0.0356/0.0486	0.0163/0.0185	0.0117/0.0114	0.0391/0.0332
UCI-1981 Burn Site	0.0634/0.0626	0.0128/0.0169	0.0086/0.0110	0.0437/0.0404
Flagstaff-Managed Forest	0.0342/0.0339	0.0187/0.0187	0.0336/0.0347	0.0298/0.0297
Flagstaff-Unmanaged Forest	0.0373/0.0427	0.0295/0.0294	0.0412/0.0398	0.0294/0.0293
Morgan Monroe State Forest	0.0326/0.0337	0.0287/0.0288	0.0278/0.0283	0.0299/0.0303
Harvard Forest	0.0330/0.0312	0.0280/0.0241	0.0253/0.0267	0.0484/0.0438
Howland Forest	0.0348/0.0336	0.0326/0.0313	0.0264/0.0320	0.0419/0.0378
U. Mich. Biological Station	0.0511/0.0552	0.0711/0.0541	0.0312/0.0769	0.0049/0.0164
Ozark Site	0.0288/0.0288	0.0276/0.0260	0.0268/0.0272	0.0253/0.0271
Bartlett Experimental Forest	0.0340/0.0536	0.0208/0.0359	0.0196/0.0235	0.0256/0.0274
Chestnut Ridge-Oak Ridge	0.0203/0.0202	0.0307/0.0289	0.0259/0.0202	0.0214/0.0213
Walker Branch Watershed	0.0196/0.0247	0.0222/0.0234	0.0278/0.0632	0.0216/0.0305
WLEF-ChEAS Park Falls	0.0330/0.0320	0.0162/0.0184	0.0207/0.0198	0.0669/0.0636
Total RMSE	**0.0331/0.0366**	**0.0246/0.0257**	**0.0306/0.0312**	**0.0334/0.0331**

Table 2.4 shows two correlation matrixes, for leaf-on and leaf-off conditions, comparing the geostatistical attributes of spatial representativeness (R_{CV}, A, R_{ST}, and R_{SV}) and the absolute RMSEs obtained for MODIS retrievals using all data records from each measurement site. The correlation matrixes provide an indication of the relationship of the geostatistical attributes to one another. By further including the RMSEs, we can investigate which geostatistical attributes are playing a major role in explaining the differences in RMSE between tower and MODIS albedos. A first look at the results shows a lot of colinearity between R_{CV}, A, and R_{ST}. These correlations become even more pronounced during leaf-off conditions, where they also show a higher correspondence

with the RMSE results. This appears to be the case when comparing the RMSE results between pairs of measurement sites.

Given their close proximity, matching temporal records, and comparable landscape features between stations, the Oak Ridge, Flagstaff, and UCI sites provide a convenient setting to investigate whether the means of the RMSEs of the measurement sites identified as the most spatially representative are lower than the means for the less representative sites. For instance, the scale requirement index (A), was on average, 26.47% higher at the younger UCI-sites during leaf-on conditions, and 36.67% higher during leaf-off conditions. Conversely, the RMSE levels at the UCI-sites were consistently lower (by ~0.0133) at the older UCI-1850 and UCI-1930 sites.

This degree of correspondence with the average RMSEs was also apparent over the Flagstaff sites, where the geostatistical attributes at the Unmanaged site were on average 48.15% higher during leaf on conditions and 22.85% higher during leaf-off conditions. Conversely, the RMSEs at the Managed site were consistently lower by ~0.0053 RMSE units. Finally, at the Oak Ridge sites, the geostatistical attributes at Chestnut Ridge were similar in magnitude for those at Walker Branch during leaf-on conditions (by ~2.0%), but were much lower (by 20.32%) during leaf-off conditions. The RMSEs at Chestnut Ridge were also consistently lower throughout the year (by 0.0018 when compared to Walker Branch), and were even lower during leaf-off conditions (by ~0.007).

Table 2.4. RMSE (Full/Full+Mag) between field-measured albedos at LSN and MODIS V005 albedos (MCD43A3) sites, using the SWIR (0.3-5.0μm) broadband, for four seasonal classes: January-February-March (JFM), April-May-June (AMJ), July-August-September (JAS), and October-November-December (OND).

Leaf-On Conditions

	R_{CV}	*A*	R_{ST}	R_{SV}	*Abs. RMSE*
Rcv	1.0000				
A	0.5407	1.0000			
Rst	0.9142	0.3570	1.0000		
Rsv	0.0856	-0.0869	0.1934	1.0000	
RMSE	-0.0034	0.0056	-0.0092	0.1160	1.0000

Leaf-Off Conditions

	R_{CV}	*A*	R_{ST}	R_{SV}	*Abs.RMSE*
Rcv	1.0000				
A	0.6918	1.0000			
Rst	0.8252	0.7249	1.0000		
Rsv	0.1592	0.0976	0.3044	1.0000	
RMSE	0.0837	0.1405	0.0165	0.4085	1.0000

A closer look at the ETM+ subsets over the Oak Ridge forest sites (Figure 2.13 - top two rows) shows a very similar spatial distribution of landscapes across Oak Ridge Forest. Despite the fact that the ground footprint over Chestnut Ridge was 50% larger (by ~250m) than the footprint over at Walker Branch, the average patch size, as defined by the range of the variogram at the station (Figure 2.14), was consistently higher by 82.35%. This resulted in similar magnitudes between the geostatistical attributes of both stations during the leaf-on periods, but more favorable results for Chestnut Ridge during leaf-off periods. Note that if the ground instrument setting between the Oak Ridge sites were to be the same, the results would have potentially favored the Walker Branch station as the most spatially representative landscape throughout the year.

A closer comparison of the remaining measures at the Flagstaff stations (Table 2.2) suggests that while the magnitudes of the scale requirement index (*A*) were almost the same throughout the year, the differences in R_{CV}, R_{ST}, and R_{SV} were as equally consistent in predicting which site (i.e. Flagstaff Managed) was the most representative of its underlying landscape. Thus, using a combination of geostatistical attributes, with *A* as the primary marker of spatial representativeness and applying the other geostatistical measures as appropriate on a case by case basis, should allow users of tower measurements to determine how the intrinsic spatial and seasonal trends within each site are being captured at the satellite footprint. A simple ranking procedure can be used to compare the spatial representativeness between measurement sites throughout the seasons:

$$R_{score} = \left(\frac{|R_{CV}| + |R_{ST}| + |R_{SV}|}{3} + A \right) \tag{2.26}$$

Table 2.5 provides the rankings for R_{score} using all study locations. Note that three of the top-five stations (i.e. Morgan Monroe State Forest, Santarem-Km83, and WLEF-ChEAS) were ranked as the most spatially representative during leaf-on and leaf-off conditions. The same applies to the least representative sites (UMBS, UCI-1964, UCI-1981, and Howland Forest West Tower), which where ranked in the bottom five throughout the year.

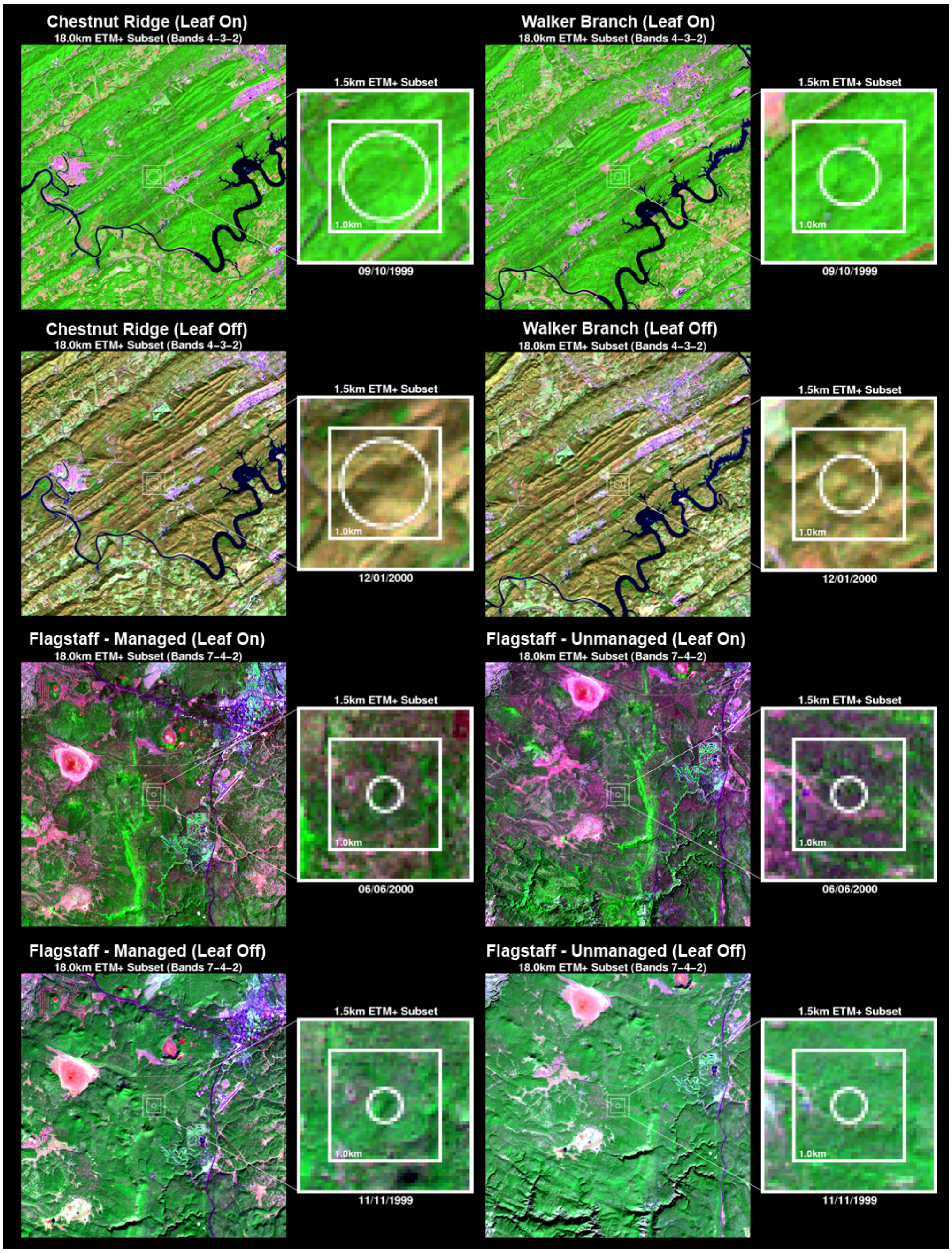

Figure 2.13. Top-of-Atmosphere (TOA) shortwave reflectance composites (ETM+ Bands 7-4-2), centered over the Oak Ridge forest sites (top two rows) and the Flagstaff forest sites (bottom two rows) for two representative time periods illustrating conditions of greenness and dormancy. Trees and bushes are in shades of green (both light and dark tones) and purple, and bare areas are seen in light-lavender, magenta, and pale-pink.

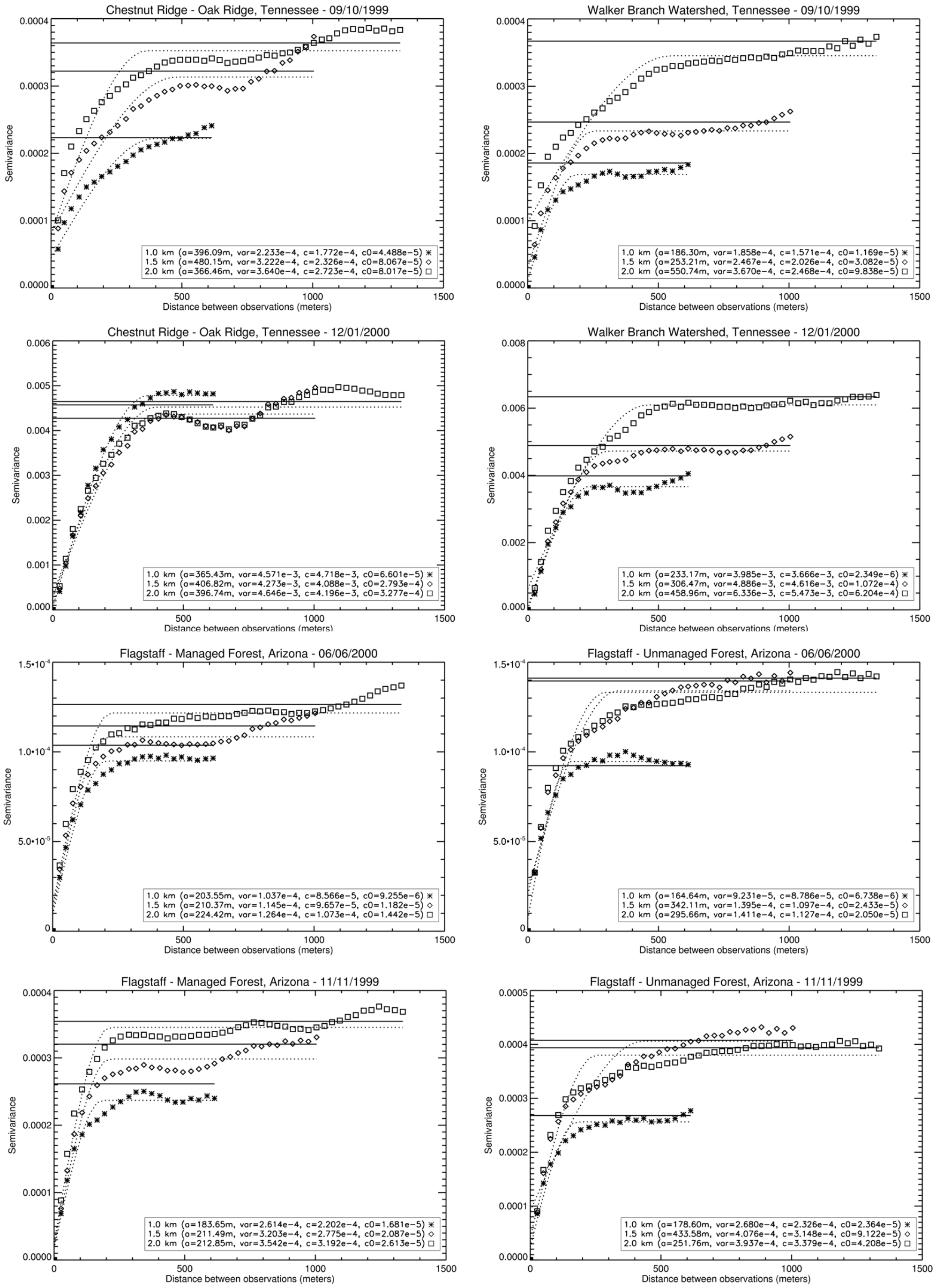

Figure 2.14. Variogram plot obtained over the Oak Ridge forest sites (top two rows) and the Flagstaff forest sites (bottom two rows). Setup is the same as Figure 2.7

Table 2.5. Ranking the spatial representativeness of AmeriFlux measurement sites based on R_{score} (see Eq. 2.26) during leaf-on and leaf-off conditions.

Rank	**Field Station**	**R_{score} - Leaf On**
1	Morgan Monroe State Forest	2.75%
2	Santarem-Km83	3.85%
3	Ozark Site	13.79%
4	WLEF-ChEAS Park Falls	16.72%
5	Flagstaff-Managed Forest	26.21%
6	Walker Branch Watershed	30.60%
7	Harvard Forest	31.03%
8	UCI-1930 Burn Site	35.01%
9	Chestnut Ridge-Oak Ridge	36.29%
10	UCI-1850 Burn Site	56.24%
11	Flagstaff-Unmanaged Forest	92.74%
12	U. Mich. Biological Station	99.52%
13	Howland Forest West Tower	103.66%
14	UCI-1981 Burn Site	112.15%
15	Bartlett Experimental Forest	117.00%
16	UCI-1964 Burn Site	163.95%

Rank	**Field Station**	**R_{score} - Leaf Off**
1	Santarem-Km83	1.66%
2	Morgan Monroe State Forest	8.85%
3	Chestnut Ridge-Oak Ridge	11.19%
4	UCI-1850 Burn Site	13.98%
5	WLEF-ChEAS Park Falls	23.11%
6	Ozark Site	25.43%
7	Flagstaff-Managed Forest	29.69%
8	Walker Branch Watershed	31.26%
9	Bartlett Experimental Forest	40.04%
10	Harvard Forest	45.12%
11	UCI-1930 Burn Site	55.44%
12	Flagstaff-Unmanaged Forest	61.35%
13	U. Mich. Biological Station	87.25%
14	UCI-1981 Burn Site	90.50%
15	UCI-1964 Burn Site	99.45%
16	Howland Forest West Tower	134.47%

2.7. Conclusions

A new validation framework for the estimation of the spatial representativeness of tower albedo measurements can successfully indicate whether tower albedo measurements are properly capturing the albedo retrievals over a large enough area to be suitable for use in direct “point-to-pixel” comparisons to the co-located satellite data. The approach combines knowledge of biophysical, spatial, and seasonal signatures of the measurement site and its surrounding landscape by utilizing multispectral high-resolution imagery as an intermediate step between ground and satellite retrievals. The resulting product is a set of geostatistical measures derived from the principles of traditional variography that can be used to quantify the degree of spatial representativeness between the prescribed footprint and its surrounding landscape at different seasonal periods throughout the year. By first establishing semivariogram attributes of the locale at multiple fields of view from high spatial resolution imagery, the geostatistical measures of spatial representativeness can be generated. If a measurement site is spatially representative, then the overall variability between the internal components of the measurement site and the adjacent landscape should be similar in magnitude and relative coefficient of variation (R_{CV}) should approach zero. Similarly, the scale requirement index (A) provides a measure of the spatial extent (or range) of surface albedo with respect to both the ground instrument’s field of view and its surrounding landscape. A measure of the relative strength of the spatial dependence (R_{ST}) captures the maximum variance in the surrounding landscape and identifies the primary sources that drive the spatial variability over a given measurement site. Finally, the relative proportion of structural variation (R_{SV}) describes the amount of landscape variability that is attributable to spatial (as opposed to random) effects, and can further identify how seasonal changes, within and across the landscape, are affecting the structural variability of a given measurement site. Results suggest that tower-based albedo measurements acquired over a broad range of forested landscapes are generally capturing the footprint of MODIS observations. However, measurement sites that were fitted with tower albedometers at very low heights (< 20 m) above ground level (e.g. UCI-1964 and UCI-1981) or in close proximity to significantly different surface conditions (e.g. UMBS) will confront difficulties in capturing the albedo retrievals from a satellite footprint > 1.0 km.

The geostatistical measures of spatial representativeness have broad utility, but are particularly useful for: (1) identifying measurement sites that are appropriately representative of a large enough footprint to validate satellite-derived retrievals of albedo; and, if needed, recommend a series of instrumental upgrades (e.g. increasing the height of the tower and instrument field of view) to improve their utility for evaluating satellite-derived retrievals of albedo; (2) producing a pixel-specific measure of product uncertainty both in terms of the quality of the algorithm inversions (e.g. given a limited number of satellite retrievals), and their ability to capture the underlying spatial and seasonal variability at local (< 1.0 km) scales. By closing the scaling gaps between the local (or point-based) and regional retrievals of surface albedo, this approach ensures that the intrinsic spatial and seasonal features of surface albedo are being resolved at the satellite footprint, thus quantifying the spatial representativeness and improving the confidence of the validation results.

Chapter 3

3. Airborne Measurements of Surface Anisotropy at the SGP Site

3.1. Introduction

Both aircraft and ground retrievals of the BRDF and albedo serve as important validation sources for land surface satellite products. Unlike surface albedo, which can be measured instantaneously by field albedometers, the BRDF cannot be measured directly, but it can be estimated using models of surface scattering in conjunction with directional reflectance data acquired at different view and solar angles. For example, ground-based PARABOLA (Portable Apparatus for Rapid Acquisition of Bidirectional Observations of Land and Atmosphere) data have been used to validate MISR retrievals (Abdou et al. 2001). On the other hard, airborne radiometers such as CAR data have been used to validate MODIS and MISR retrievals (Abdou et al. 2006; Gatebe et al. 2003), while airborne POLDER has been used to validate POLDER retrievals (Leroy and Hautecoeur 1999). The PARABOLA data have the advantage of being able to control the angular sampling of directional reflectances (such as the principal solar plane) and are less influenced by atmospheric interference. The disadvantages of the PARABOLA data include low angular resolutions (~15°) and relatively smaller spatial footprints than that of satellite and airborne datasets. Conversely, although aircraft measurements have higher angular resolutions and larger spatial coverages than PARABOLA data, making them suitable for validation of land surface satellite products, airborne sensors must also contend with issues such as geolocation, gridding, and atmospheric correction.

In the past, there have been several efforts to compare MODIS V005 albedo and BRDF retrievals to ground radiometer data at the Department of Energy's (DOE) Atmospheric Radiation Measurement (ARM) Program Southern Great Plains Central Facility (SGP-CF) in North-Central Oklahoma, USA (Luo et al. 2003; Salomon et al. 2006; Yang 2006), and to other ground radiometers around the station ((Jin et al. 2003b; Liang et al. 2002; Liu et al. 2009)). Additional studies have evaluated BRDF retrievals obtained from airborne sensors, such as Research Scanning Polarimeter (RSP) (Knobelspiesse et al. 2008) and airborne POLDER (Chen et al. 1997; Leroy and Hautecoeur 1999) against coincident ground and satellite data. However, the vast differences in spatial resolution, measurement methodologies, and atmospheric effects create a number of technical and logistical challenges for such direct "point-to-pixel" comparisons. Previous studies, e.g. (Chen and Leblanc 1997; Leblanc et al. 1999) have implemented a number of geometric-optical models to investigate the causes of such differences in relation to the effects of various scales of canopy architecture on the BRDF. These assessments, however, have thus far been restricted to forested landscapes and require accurate estimates of tree architecture (e.g. leaf area index, leaf optical properties, and tree algometry) to simulate the non-random tree distribution and sub-canopy architecture.

Because of its ability to obtain directional signatures at several heights above ground level (e.g. 200 m, 600 m, 2.0 km, and ~4.0 km), the Cloud Absorption Radiometer (CAR) (Gatebe et al. 2003; King et al. 1986), can provide independent estimates of surface BRDFs, and the albedos derived from them, at multiple scales of resolution (~ 4– 300 m, depending on view angle and aircraft height above ground). The current BRDF retrieval method applied to CAR data generally acquires representative BRDFs of the underlying surface, for each CAR spectral channel, as defined by a circular flight track ~ 3 km in diameter. These data are then averaged together to smooth out surface inhomogeneities of the reflected solar radiation signal (Gatebe et al. 2003).

One of the key features of the CAR instrument is that it can resolve the finer-scale features of the various surface covers along and across its flight and scan tracks. Most importantly, and unlike most airborne sensors, the CAR is actively stabilized by a sophisticated navigation system. Thus, each scan is accompanied by high frequency navigation data, which allows for excellent geolocation accuracy (< 1m). Accordingly, this paper presents a new spatial transformation and scaling method, whereby directional surface reflectances acquired by the CAR are allocated into the most frequently sampled spatial domains as observed by the instrument during a particular flight. This technique allows for a consistent recreation of the measurement methodology, spatial coverage, and data processing protocols adopted by the MODIS V005 BRDF/Albedo algorithm. This enables us to investigate the aforementioned issues and, consequently, improve our understanding of product uncertainty, vis-à-vis MODIS, both in terms of the quality of the BRDF model inversions (e.g. given a limited number of cloud-free retrievals), and their ability to capture the residual spatial dependence of the underlying landscape.

This chapter is organized as follows. First, we provide (1) an overview of the CAR instrument, (2) a summary of the ARM-CLASIC campaign, including its goals and experimental support, a description of the ARM-SGP Central Facility, flight segment details, and ancillary data layers. We implemented the proposed method in the CAR measurements from CLASIC as follows: (1) The directional measurements obtained by the CAR were radiometrically corrected, (2) then transformed and scaled into mapping space, and (3) the at-sensor radiances were atmospherically-corrected using aerosol retrievals directly obtained from inversion of CAR and ground-based sunphotometer data. (4) Next, the semiempirical RTLSR BRDF model was inverted using all the directional reflectances available from the CAR instrument over each individual grid cell and the inverted models run in a forward fashion to compute, within each CAR channel, the white-sky, black-sky and actual (or blue-sky) albedo quantities, using (for the latter) the fractions of direct beam and diffuse illumination calculated for the optical depth and solar zenith angle range observed throughout the flight. (5) Finally, after applying a set of narrowband to broadband (NTB) conversion routines to the multispectral results provided by CAR, the diurnal cycle of three broadband albedos, i.e. visible (0.3 - 0.7 μm), shortwave infrared (0.7 - 5.0 μm), and full solar range (0.3 - 5.0 μm), was derived using the black-sky, white-sky, and blue-sky albedo quantities. A validation exercise over the ARM-SGP Central Facility and surrounding landscape is then presented in the results section including; first, an assessment of narrowband BRDF model parameters of archetypal landscapes; second, a comparison of BRDF model parameters from CAR and MODIS; and third, an assessment of intra-daily variations in surface albedo as seen from CAR, MODIS, and ground observations. This greatly helps the interpretation of the results since it recognizes the various degrees of difficulty and sources of uncertainty associated with the quality of the CAR and MODIS algorithm inversions and their ability to respond to the underlying atmospheric conditions as well as the spatial and temporal variability of the landscape. The results are summarized at the end.

3.2. The Cloud Absorption Radiometer: Instrument Description

A complete description of the CAR instrument is given by King et al. (1986), and updated by Gatebe et al. (2003) following an upgrade of the instrument in 2000. This brief overview, however, highlights some aspects of the instrument, as illustrated in Figure 3.1 and presented in Table 3.1, and summarizes the characteristics of the CAR sensor, platform, and scanning system as applicable during CLASIC. The CAR is a 14-channel airborne scanning radiometer (with a spectral range from 0.331 – 2.345 μm) that can perform several functions including: (1) determining the single scattering albedo of clouds at selected wavelengths in the UV, visible, and near-infrared (King 1981; King et al. 1990), (2) acquiring imagery of clouds and the Earth’s surface, and (3) measuring the angular distribution of scattered radiation of various surfaces types (Gatebe et al. 2003).

Table 3.1. Current CAR Specifications. Adopted from Gatebe et al. (2003).

Platform	Jetstream-31 (J-31) research aircraft
Ground speed	80 m s^{-1}
Total field of view	190
IFOV	17.4 mrad (1°)
Imaging modes	4 (zenith, BRDF, starboard, and nadir)
Pixels per scan line	382
Scan rate	1.67 scan line per second (100 rpm)
Spectral channels (mm; bandwidth (FWHM))	14 (8 continuously sampled and last 6 in filter wheel), 0.340 (0.009), 0.381 (0.006), 0.472 (0.021), 0.682 (0.022), 0.870 (0.022), 1.036 (0.022), 1.219 (0.022), 1.273 (0.023), 1.556 (0.032), 1.656 (0.045), 1.737 (0.040), 2.103 (0.044), 2.205 (0.042), 2.302 (0.043)
Output channels	9 channels at 16 bits
Data rate	61.85 MB hr^{-1}
Instrument Mass	42 kg
Radiometric Calibration	Laboratory integrating sphere measurements before and after research mission

The first eight channels of the CAR instrument are continuously and simultaneously sampled, while the ninth registered channel is selected from among six channels on a filter wheel. For this study, the ninth channel (the filter wheel channels) was not used because of a problem with the detector. The CAR was designed to operate from a position mounted on an aircraft, either the tail or the nose or wing, so that its scan is unimpeded as it samples the sky and surface from zenith to nadir. The instantaneous field-of-view of the radiometer is 1° (or ~17.4 mrad) and scans through a wide angle defined by an aperture of 190° and perpendicular to the plane's velocity vector.

The instrument can be positioned to image any direction perpendicular to the flight track, but it is mostly used to image the surface or sky from horizon to horizon or in the starboard from aircraft zenith to nadir, 95° on either side of the aircraft horizon. This permits observations of both zenith and nadir directions with as much as a 5° aircraft roll.

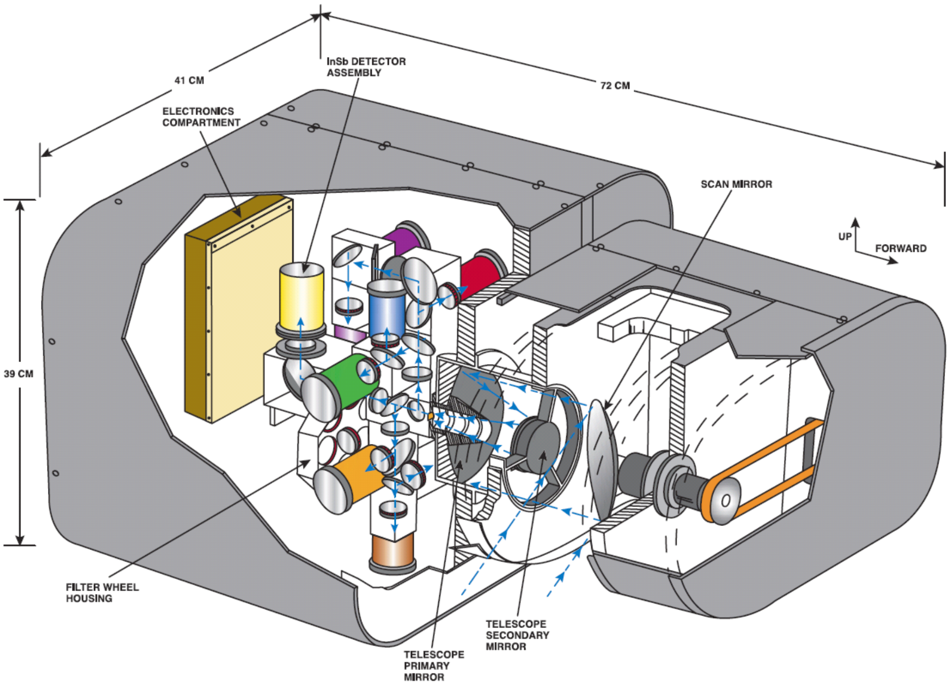

Figure 3.1. The CAR has 14 narrow spectral bands between 0.340 and 2.30 um. It images the sky and surface at an IFOV of ~1° through any plane defined by 190°. Adopted from Gatebe et al. (2003).

Figure 3.2 shows a typical flight pattern whereby the aircraft, with the CAR in the nose cone, flies a clockwise circular pattern above the surface repeatedly, drifting with the wind, scans the underlying surface and much of the transmitted solar radiation from above, and makes radiometric observations about every 1° in zenith angle. To measure the BRDF, multiple circular orbits over a particular surface can be acquired under clear sky conditions to smooth out small scale surface and atmospheric variations. These data are then averaged together to obtain a representative BRDF of the underlying surface within ~3 km domain defined by the flight circles. During post processing, the CAR data is carefully georectified and calibration coefficients applied (Gatebe et al. 2005).

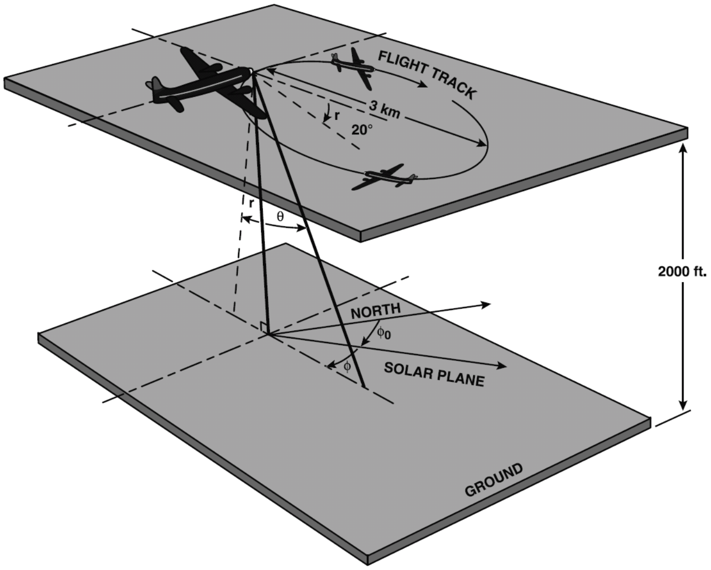

Figure 3.2. Schematic illustration of a clockwise circular flight track for measuring surface bidirectional reflectance from nadir to the horizon as well as much of the transmittance pattern from near zenith to the horizon. The plane banks at a roll angle of about 20° as it circles a target of interest. Each orbit takes ~2.5 min to complete and consists of a circle of about 3 km in diameter. Adapted from the study of King, (1992).

The selected surface BRDF data is screened to achieve low noise level, a sufficient number of clear retrievals, and a roughly even sampling of directional space. Using CAR in this way is therefore the most mobile and efficient way of measuring a representative surface BRDF, although it is still necessary to correct for atmospheric scattering effects both above and below the aircraft in order to isolate the reflectance properties of the underlying surface in the absence of an atmosphere.

3.3. ARM-CLASIC Campaign

3.3.1. Campaign Goals and Experimental Support

Fundamental to the objectives of CLASIC is the understanding of the interactions between the atmosphere and the land surface. With this goal in mind, an extensive field campaign was conducted in the summer of 2007 to obtain the necessary measurements, with a primary emphasis on the US Southern Grain Plains (SGP) encompassing field stations in Oklahoma and Kansas. CLASIC measurements for the intense observing period were taken between June 9-30, 2007 with main operations based in Ponca City, Oklahoma. The measurements were conducted with a wide range of instruments located at ground sites, on aircraft, and satellites. Surface measurements were primarily retrieved over four stations in the SGP with dominant land uses/covers such as winter wheat/stubble at the Central Facility (36.60°N, 97.48°E), grasslands at the Little Washita Watershed (35.044°N, 97.914°W), irrigated crops at the Fort Cobb Watershed (35.15°N, -98.47°E), and broadleaf deciduous canopies at the Forest Site (35.615°N, -96.07°E) (Cosh 2007). Each of these “super sites” dominated a specific geographic area; e.g. winter-wheat crops in the east and north, forests in the east, irrigated crops in the west, and grasslands in the south and west of the SGP. CLASIC field stations were also selected to include the geographic/land use distribution, considering existing resources.

The harvest of winter-wheat is particularly interesting in the SGP region, as during this period, most of the land is converted from waist- high winter wheat to bare soil in a matter of hours. The timing of this harvest occurs in early June and depends, among several factors such as seasonal climate trends, recent precipitation, and the availability of migrating harvesting equipment. Human induced changes in the land surface structure associated with plowing, crop rotations, and irrigation can induce changes in the surface latent heat flux, sensible heat flux, albedo, and carbon flux. Drastic changes in surface albedo associated to these impulse-like surface perturbations have important implications for the structure and occurrence of cumulus convection; which tend to trigger other feedback effects (e.g. increases in evapotranspiration and stomatal resistance) on these intensive agricultural landscapes.

3.3.2. ARM-SGP Central Facility

The heavily instrumented ARM-Southern Great Plains Central Facility (SGP-CF) (Figure 3.3) is located at the heart of the SGP on 160 acres of cattle pasture and wheat fields southeast of Lamont, Oklahoma. This station is situated at an elevation of 1014 m with temperatures averaging 34.7º C in the summer and -5.0º C in the winter seasons. The climate is classified as sub-humid with an average annual rainfall of 750 mm. During CLASIC, surface characteristics at the SGP-CF were typical for the rural mid-west of the United States in the summer.

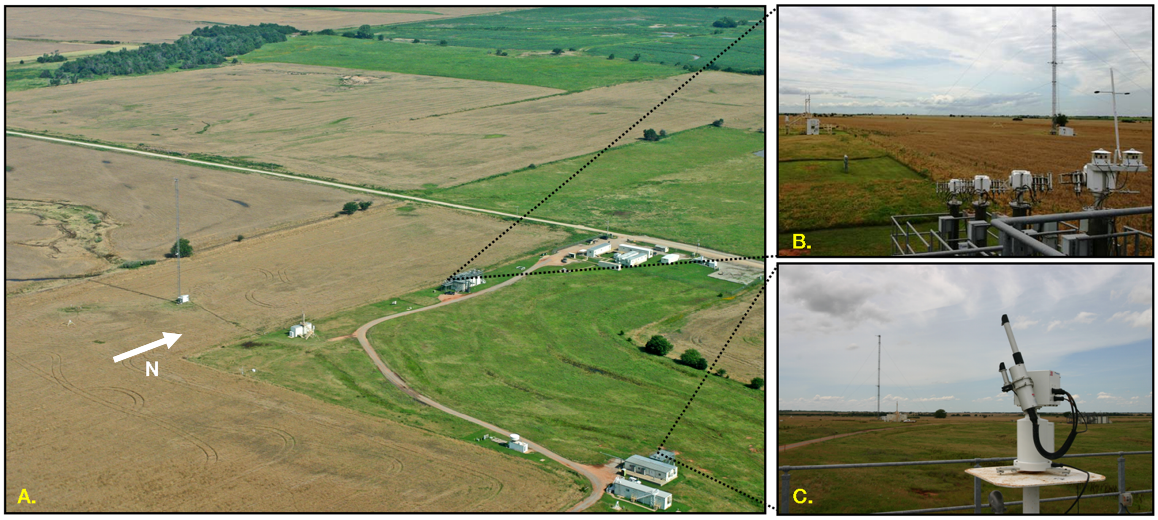

Figure 3.3. (A) Bird's eye view of the ARM-Southern Great Plains Central Facility (SGP-CF) taken during CAR-CLASIC Flight #1922 (19 June 2007); (B) facing southwest atop the Radiometric Calibration Facility, overlooking the upward-facing pyranometers and the 60 meter radiation tower (20 June 2007); and (C) facing west atop the Guest Instrument Facility, overlooking the AERONET sun photometer (20 June 2007).

The ground at the SGP-CF is relatively flat and covered by a patchwork of winter-wheat, corn fields, bare soil exposed by spring harvesting, and mixtures of pasture fields and trees. There are a few buildings and the occasional paved and dirt roads. A downward-facing pyranometer has been installed at the Central Facility’s 60 m radiation tower, while a series of upward-facing pyranometers (both clear and sun-shaded) have been installed at nearby Radiometric Calibration Facility (RCF). These instrument setup follows a strict set guidelines as established by the Baseline Surface Radiation Network (BSRN) (McArthur 2004); with local staff maintaining the upward-facing sensors throughout the year. These instruments are outfitted with clear domes to collect broadband albedo and radiation fluxes in the shortwave (SW) (0.3- 2.8 µm) waveband.

Two additional instruments atop the RCF, a normal incidence pyrheliometer mounted on an automatic sun tracker and a shaded pyranometer riding on top of the sun tracker, measure direct and diffuse solar radiation incident upon the field stations. We also utilized estimates of cloud fraction as viewed from the skyward-looking pyranometers. We used the mean values provided at 30 minute intervals for the period of CLASIC from the Clouds and the Earth's Radiant Energy System (CERES) ARM Validation Experiment (CAVE) archive (http://snowdog.larc.nasa.gov/cave/) (Rutan et al. 2001).

3.3.3. Flight Segment Details

There were a total of eleven CAR flights accomplished as part of CLASIC. Only data from CLASIC Flight #1928 (the 10th flight out of Ponca City on 24 June 2007) was used in this study. A complete description of this and other CAR flights, including flight summaries (i.e. path, timing, and measurements), imagery, and mission details can be found at the CAR web site (http://car.gsfc.nasa.gov/data/).

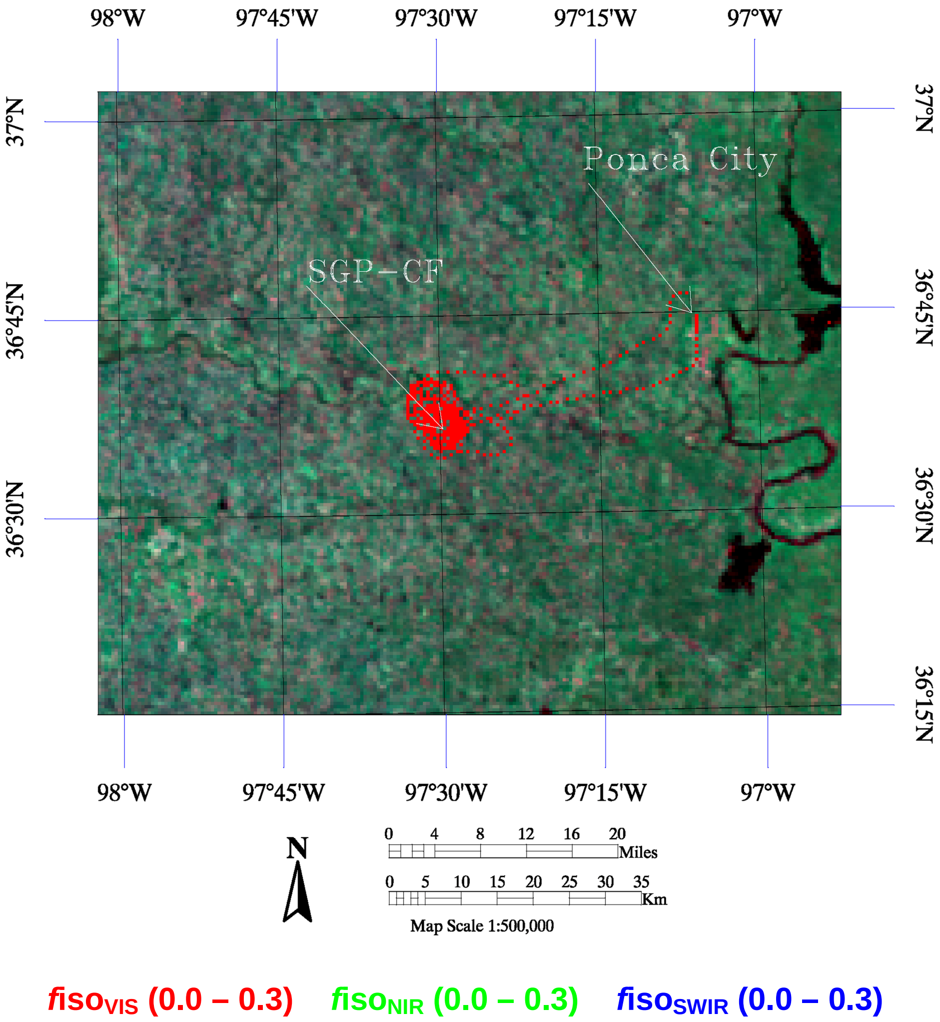

Figure 3.4. MODIS Collection V005 500 m BRDF model parameters overlaid with J-31 flight track. The BRDF model parameters are used to reconstruct surface anisotropic effects and thus correct directional reflectances to a common view geometry and compute integrated albedos. The colors describe isotropic weighting parameters (i.e. R-G-B → $f_{iso,VIS}$ - $f_{iso,NIR}$ - $f_{iso,SWIR}$) for data acquired between June 18 to July 4, 2007 over the ARM Program's Southern Great Plains Central Facility (SGP-CF). Arrows point to Ponca City, OK and the Central Facility. The red line denotes the path of the J-31 aircraft throughout Flight #1928 (24 June 2007).

CLASIC Flight #1928 experienced favorable weather conditions and followed a flight pattern that was optimal for BRDF measurements over the SGP Central Facility (CF) (Figure 3.4). BRDF measurements were also taken at several heights above ground level (i.e. 200 m, 600 m, 2000 m, and ~4000 m) under clear-sky conditions during the entire flight period, with the exception of a small cluster of clouds, visually spotted faraway from the station at ~30° from the southern horizon.

3.3.4. Land Cover Characterizations

A number of intensive manual land cover surveys, vegetation measurements, and surface characterizations were conducted during CLASIC to obtain detailed vegetation land cover information. Several Advanced Wide Field Sensor (AWiFS) scenes, at 56 m spatial resolution, were acquired to map the vegetation and land cover over the SGP domain. While there was little cloud-free imagery available for the actual CLASIC study period, a complex algorithm based upon a decision tree developed using previous studies (Doraiswamy et al. 2004; Friedl and Brodley 1997; Jackson et al. 2004), in combination with the available land survey data from April through September 2007, was used to create a land cover dataset with an overall accuracy of 82.66%. Figure 3.5 shows a 8 km x 8km subset of the CLASIC-AWiFS land cover dataset showing the areas that were sampled by the CAR during Flight #1928. The CAR collected data over a number of sections, hereafter defined by a series of letters from *A* to *N*.

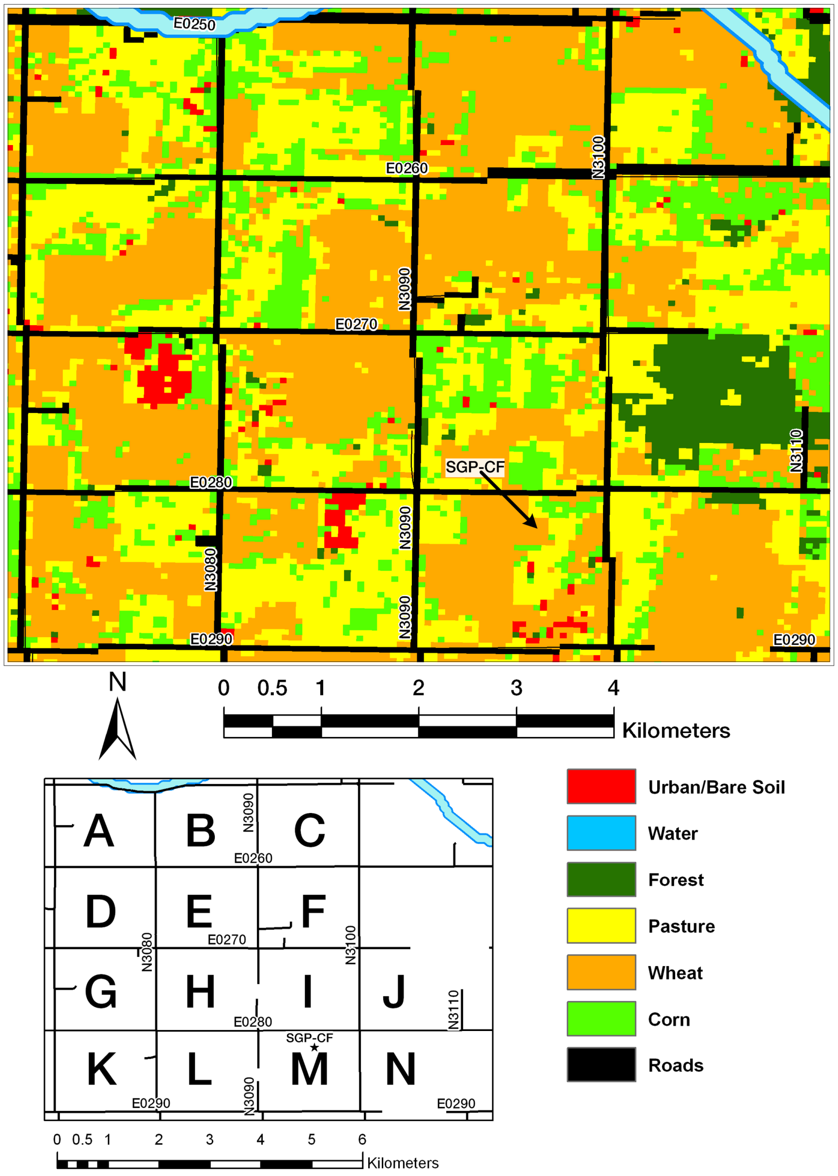

Figure 3.5. CLASIC-AWiFS land cover subset of the areas surrounding the ARM-SGP Central Facility that were sampled by the CAR during Flight #1928. A total of 14 equally separated sections (from A to N), were identified to directly compare retrievals from the CAR and MODIS sensors during the period of CLASIC.

These 1.6 km x 1.6 km regions are equally separated by a same network of county roads. The ARM Central Facility is located in quadrant M. In order to improve the classification accuracy over each of these sections, a Quickbird scene acquired just 8 days after Flight #1928 (1 July 2007) was used. By manually examining each of these regions, we were able to correct for any apparent errors in the classification.

3.4. Methods

3.4.1. CAR Data Processing

The current CAR BRDF retrieval algorithm uses between ~76,400–114,600 directional measurements of radiance per channel per complete orbit to obtain a representative BRDF of the underlying surface as defined by a flight circle of ≈ 3 km in diameter (Gatebe et al. 2003). These data are then averaged together to smooth out small scale surface inhomogeities in the reflected solar radiation signal. Because of its ability to obtain BRDF measurements at several heights above ground level (e.g. 200 m, 600 m, 2.0 km, and ~4.0 km), the CAR can further provide independent estimates of surface BRDFs at multiple scales of resolution (~4.0 - 300 m – depending on view angle and altitude). Finally, unlike most airborne radiometers, the CAR is actively stabilized by a sophisticated navigation system. Thus, each CAR scan is accompanied by high frequency navigation data, which allows for excellent geolocation of CAR retrievals. In order to maximize the full technical capabilities of the CAR instrument, we have developed a new BRDF and albedo retrieval algorithm, as illustrated in Figure 3.6 and presented in sections 3.4.1.1 - 3.4.1.5.

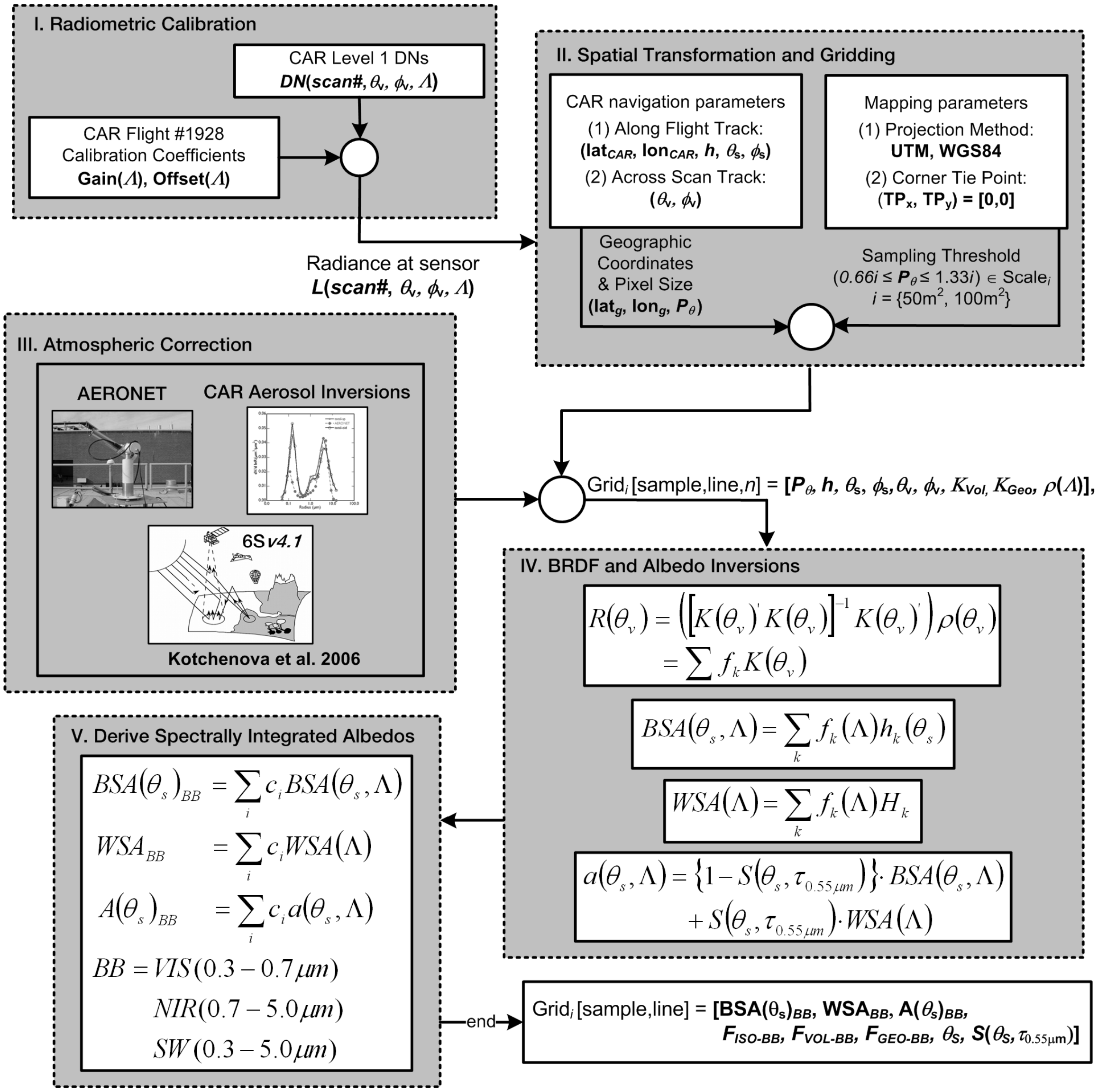

Figure 3.6. Processing and data flow diagram illustrating the production of broadband retrievals of surface albedo and reflectance anisotropy from NASA's Cloud Absorption Radiometer (CAR).

3.4.1.1. Radiometric Calibration

Radiometric calibration of the CAR spectral channels was made at the NASA Goddard Space Flight Center Radiometric Calibration Facility (GSFC-RCF). A description of the calibration scheme, using a series of integrating spheres with diameters of 1.83, 1.22, and 0.51 m, covering all of the CAR's spectral channels, can be found in Gatebe et al. (2007). The conversion from CAR Digital Numbers (DNs) to Level 1 at sensor radiances is determined from the instrument's response for at least two known radiance levels and then determining the instrument gain (slope) and offset (intercept) for each wavelength across the sensor band pass. The estimated errors associated with this radiometric conversion vary from ±1% to ±3% for all spectral channels (Gatebe et al. 2007; 2003). Radiometric calibration was performed prior to and after the CLASIC campaign. In the past to determine a suitable calibration for a given flight during the experiment, a linear change between the preflight and postflight calibration was assumed and as a function of only the number of flights flown during an entire campaign. But for the CLASIC experiment, which had a total of 11 flights, we averaged pre- and post-calibration coefficients. We found this to be representative and made it easier to account for uncertainties in calibration. We note that the calibration ratios, postflight/preflight, varied between 0.9691 (at $\Lambda = 0.472$ μm) and 1.1845 (at $\Lambda = 0.340$ μm).

3.4.1.2. Geometric Correction and Scaling of CAR Retrievals

The CAR navigation system provides the required parameters to perform geometric correction of the acquired retrievals from each flight. At the beginning of each mirror scan cycle, the system records the current UTC time, the instrument's latitude (lat$_{CAR}$), longitude (lon$_{CAR}$), altitude above mean sea level (h), aircraft heading as well as the current solar zenith (θ_s) and solar azimuth (ϕ_s) angles. The instrument's azimuthal angle is derived from the aircraft heading by adding 90° to the heading. As the instrument scans from zenith to nadir, the CAR also registers the pixel viewing zenith angle (θ_v) for each of the ~382 pixels obtained across a scan line. Given these parameters, we can derive the geographic coordinates of a ground target (lat_g, lon_g):

$$lat_g = \sin^{-1}\left(\sin(lat_{CAR})\cdot\sin\left(\frac{d}{R_\otimes}\right)+\cos(lat_{CAR})\cdot\sin\left(\frac{d}{R_\otimes}\right)\cdot\cos(\phi_v)\right)\left(\frac{\pi}{180^\circ}\right) \tag{3.1}$$

$$lon_g = \left(-\operatorname{mod}(a,360^\circ)+180^\circ\right), \tag{3.2}$$

where

$$d = h\tan(\theta_v) \tag{3.3}$$

$$a = lon_{CAR} - dlon + \pi \tag{3.4}$$

$$dlon = \begin{Bmatrix} 0, & \cos(lat_g) = 0 \\ \psi, & \cos(lat_g) \neq 0 \end{Bmatrix} \tag{3.5}$$

$$\psi = \arctan\left(\sin(\phi_v)\cdot\sin\left(\frac{d}{R_\otimes}\right)\cdot\cos(lat_{CAR}),\cos\left(\frac{d}{R_\otimes}\right)-\sin(lat_{CAR})\cdot\sin(lat_g)\right) \tag{3.6}$$

$d/R_\otimes$ is the angular distance (in radians), where d [km] is the distance to the ground target and $R_\otimes$ is the earth's radius ≈ 6,378.13 km.

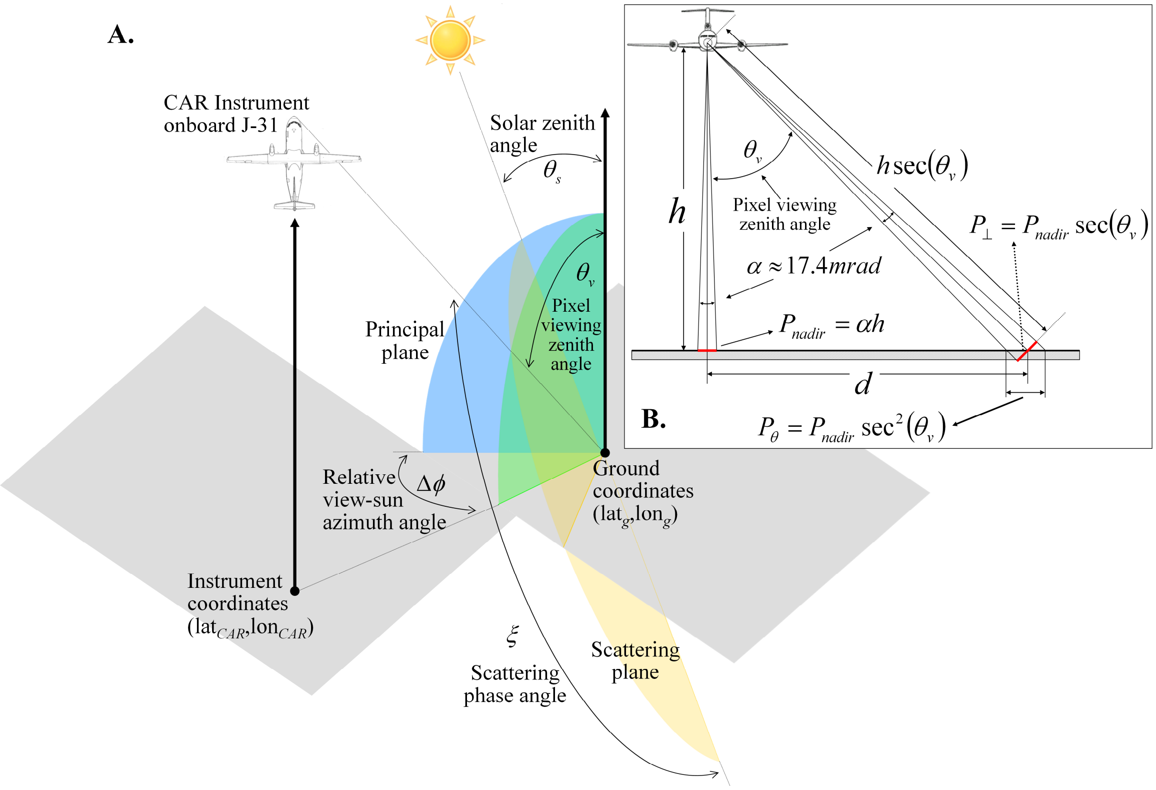

Figure 3.7. (A) The CAR's position (lat$_{CAR}$, lon$_{CAR}$) relative to a ground target (lat$_g$, lon$_g$) and the Sun is conventionally represented by the pixel viewing zenith angle (θ_v), solar zenith angle (θ_s), relative azimuth angle ($\Delta\phi$), and scattering phase angle (ξ). (B) The effects of the CAR's viewing geometry on image pixel size.

Assuming a circular flight path, a small bank angle and an aircraft speed of ~150 m/s, the CAR instrument can make radiometric observations about every 1° in azimuth and about 1° in zenith angle. Thus, the image pixel width will directly increase as a function of pixel viewing zenith angle (θ_v). This geometric distortion can be accounted for by the geometric relationships represented in Figure 3.7 (B). The size of a nadir-looking CAR pixel (p_{nadir}) is a function of the altitude above ground level (h) as well as the instrument field of view (α in radians):

$$P_{nadir} = \alpha \cdot h \tag{3.7}$$

Off-nadir pixel widths (p_θ) are then calculated based on the relationship:

$$P_\theta = P_{nadir} \cdot \sec^2 \theta_v \tag{3.8}$$

with θ_v representing the pixel viewing zenith angle at a particular instant across the scan track.

In order to establish a relationship between the position of each ground target as measured by the CAR and their corresponding coordinates in image space, the geographic locations of each ground target pixel (i.e. lat_g, lon_g) were transformed into the Universal Transverse Mercator (UTM) coordinate system using the World Geodetic System–84 (WGS-84) datum. By converting the projection units from degrees to meters, the image coordinates of each retrieval were then obtained by referencing their position to that of the UTM coordinates of the upper left-most corner of the image, known as the tie point (*TP*), and the desired pixel scale ($scale_i$):

$$[CAR_{sample}, CAR_{line}]_i = \left[\frac{(UTM_x - TP_x)}{scale_i}, \frac{(UTM_y - TP_y)}{scale_i} \right] \tag{3.9}$$

where

$$TP_x = TP_{x0} + (scale_i \cdot 0.5) \tag{3.10}$$

$$TP_y = TP_{y0} - (scale_i \cdot 0.5) \tag{3.11}$$

Note that a one-half pixel must be added in both the easting and northing directions of *TP* to accurately represent the center location of the corner pixel [0,0].

Each CAR flight undergoes a unique retrieval scenario depending on the number and size of the BRDF circles, and the altitude reached throughout the flight. Thus, an efficient transformation of CAR retrievals into image space should be applied at the appropriate scales at which the instrument is capturing the highest number of observations per grid (#obs/grid). By varying $scale_i$ using retrievals from CLASIC Flight #1928, we created a cumulative histogram function that measures the number of CAR pixels, within spatial grids separated by pixel intervals of size *i*, with a limited number of observations (Figure 3.8). A spatial threshold of (2/3)*i* to (4/3)*i* was used to group all the directional signatures available for a particular grid cell. For instance, a grid defined by 50.0 m pixels uses all available CAR retrievals at each point that are within a spatial threshold of 33.0 to 66.0 m to define each grid cell. This pixel range closely follows the more routine retrievals obtained by the MODIS sensors throughout a multi-date period (Wolfe et al. 2002). Figure 3.8 is a cumulative function in that it acts as a logical filter between the limits established by the #obs/grid. Thus, the number of CAR pixels with >16 obs/grid, for any given spatial grid, will always be greater than the number of CAR pixels with >32 to >128 obs/grid. Notice that when scaling the CAR data using 40.0 m spatial grids, the CAR obtained more than 7500 pixels with >8 obs/grid, but less than 100 pixels with >16 obs/grid. However, by slightly decreasing the spatial resolution, from 40.0 m to 50.0 m grid cells, the number of CAR pixels with >16 obs/grid increases by ~3500 pixels.

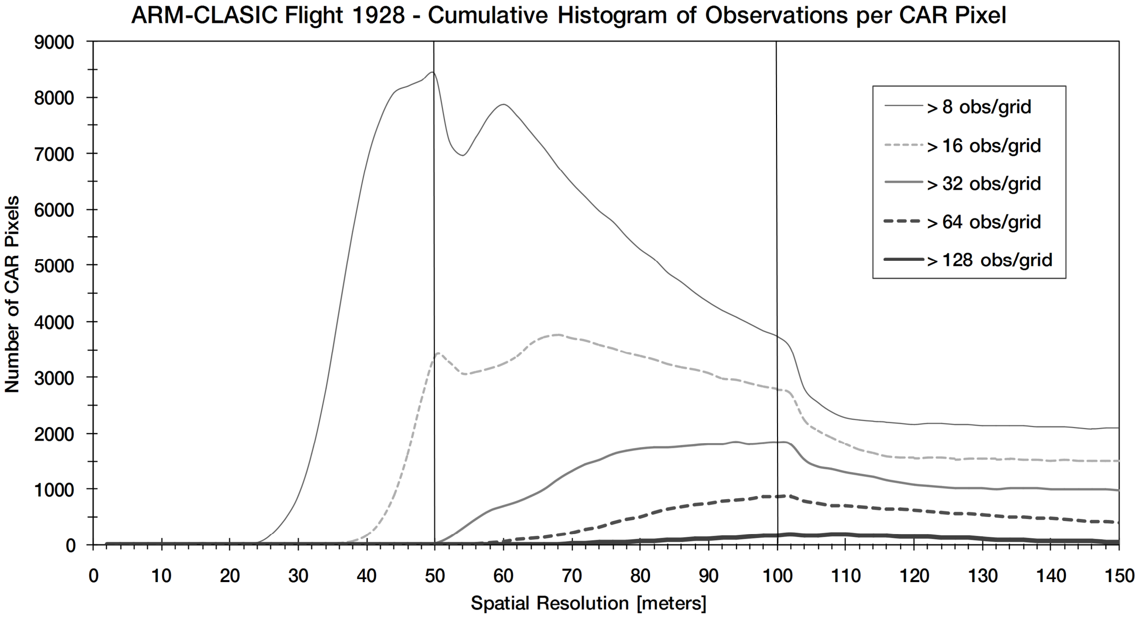

Figure 3.8. Cumulative histogram of observations per CAR pixel, for CLASIC Flight #1928. This histogram measures the number of CAR pixels obtained when using variable spatial grids from 4.0 m to 150 m. Five limits are defined (from top to bottom) for CAR pixels with >8, >16, >32, >64, and >128 observations/grid. Spatial grids defined by pixels of size 50 m and 100 m (defined by solid vertical lines) reached a peak number of CAR pixels for most observation limits.

For CLASIC Flight #1928, a spatial domain defined by 50 m grid cells significantly increases the #obs/grid and, consequently, increases the likelihood of obtaining high-quality inversions of the BRDF. The same outcome applies to spatial domains defined by 100 m grid cells. When compared against a range of spatial scales of similar size, these two scales achieve a peak #obs/grid for most observation limits.

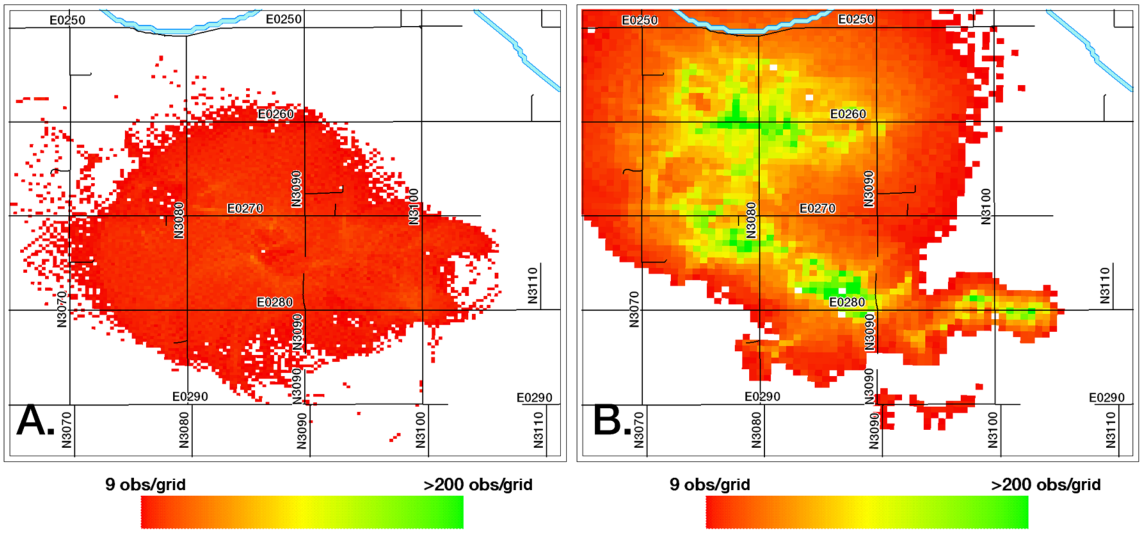

Figure 3.9. Frequency maps (in units of #obs/grid) indicating the number of retrievals per grid for two grid sizes (A.) 50 m and (B.) 100 m.

Figure 3.9 shows maps indicating the #obs/grid obtained when using spatial domains defined by 50 m and 100 m image pixels (left and right, respectively). Note that the spatial coverage and number of retrievals (ranging from 9 obs/grid to 311 obs/grid for both the 50 m and 100 m grids, respectively) vary significantly. The differences in the centroid location (i.e. the ground location with the highest #obs/grid) may have been favored by drifting of the aircraft at high altitudes, where the winds are usually stronger.

Although more directional observations are gained by scaling the CAR data using spatial domains defined by 50 m and 100 m grid cells, a portion of these retrievals may still occupy a small or extreme part of the viewing and illumination hemisphere; thus causing uncertainties in the BRDF model inversions. Accordingly, Figure 3.10 shows maps indicating the total #obs/grid that do not deviate more than 10° from the principal plane.

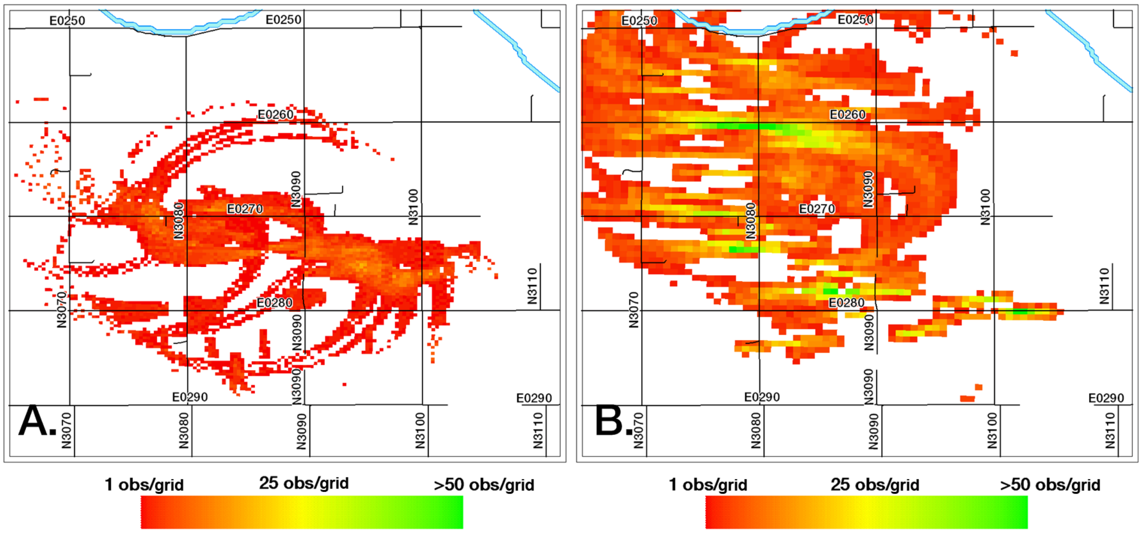

Figure 3.10. Spatial distribution of (A.) 50 m (B.) 100 m grid cells over the SGP-CF site for points within 10° from the principal plane. For most locations, the #obs/grid is less than 25.

For the 50-m CAR grid, these retrievals were clustered across a single row of sections (i.e. *G*, *H*, and *I*). There's also a gap in the number of retrievals available over the upper sections (*A*, *B*, and *C*). Conversely, the 100 m CAR grid obtained a higher number of retrievals near the solar plane, but with some noted gaps in the southern-most sections (i.e. *K*, *L*, *M*, *N*). Figure 3.11 shows the average #obs/grid (as from Figure 3.9) for all the pixels available over each of the 14 sections measured by the CAR, as well as the average #obs/grid near the solar plane (as from Figure 3.10).

Average Number of Retrievals per CAR Pixel

CAR (50m)			
9	10	9	-
12	17	12	-
15	20	18	14
13	13	12	10

CAR (100m)			
87	80	27	-
85	68	20	-
65	84	30	44
0	0	9	0

Quadrants			
A	B	C	-
D	E	F	-
G	H	I	J
K	L	M	N

Average Number of Retrievals per CAR pixel
Near the Principal Plane

CAR (50m)			
0	0	0	-
2	1	0	-
1	2	4	2
1	1	1	3

CAR (100m)			
12	18	4	-
11	4	3	-
2	9	5	9
0	0	0	0

Figure 3.11. (Top Arrays) Average number of retrievals per CAR pixel obtained from all the pixels available over each of the 2 km (*A*-*N*) sections that define the ARM-Southern Great Plains Central Facility study domain (see Figure 3.5). (Bottom) average number of CAR retrievals, over the same sections that are near the solar plane.

As expected, the 100 m CAR grid obtained the highest number of retrievals, both overall and near the solar plane. However, only the 50 m CAR grid obtained a sufficient number retrievals over the lower sections. BRDF and albedo retrievals were thus derived over each of these sections using both CAR grids to address the spatial gaps between datasets.

3.4.1.3. Atmospheric Correction

Directional surface reflectances were obtained by removing the effects of atmospheric absorption and scattering using the 6SV4.1 radiative transfer code (Kotchenova et al. 2006), in combination with ground and airborne retrievals of aerosol optical properties obtained in-situ throughout CLASIC Flight #1928. The 6SV model allows us to determine the attenuation of solar irradiance under clear-sky conditions at the surface. The code is based on the method of successive orders of scattering approximations and its current vector version is also capable of accounting for radiation polarization. 6SV removes the effects of Rayleigh scattering, aerosol attenuation, and ozone and water vapor absorption, provided we know the key characteristics of the atmosphere, such as the atmospheric optical thickness, aerosol model, and absorbing gas concentration.

The 6SV computation was performed assuming a homogenous surface with a Lambertian reflectance, a solar zenith angle range of 48.1° - 74.0° (depending on flight time), and an aerosol optical thickness $\tau_{0.55\mu m}$ = 0.1638 (0.1405 above the aircraft when flying at ~200 m above the surface). These results were acquired using Level 2 aerosol optical depth data from an AERONET sunphotometer (Holben et al. 2001) that is based at the SGP-CF and available throughout CLASIC Flight #1928.

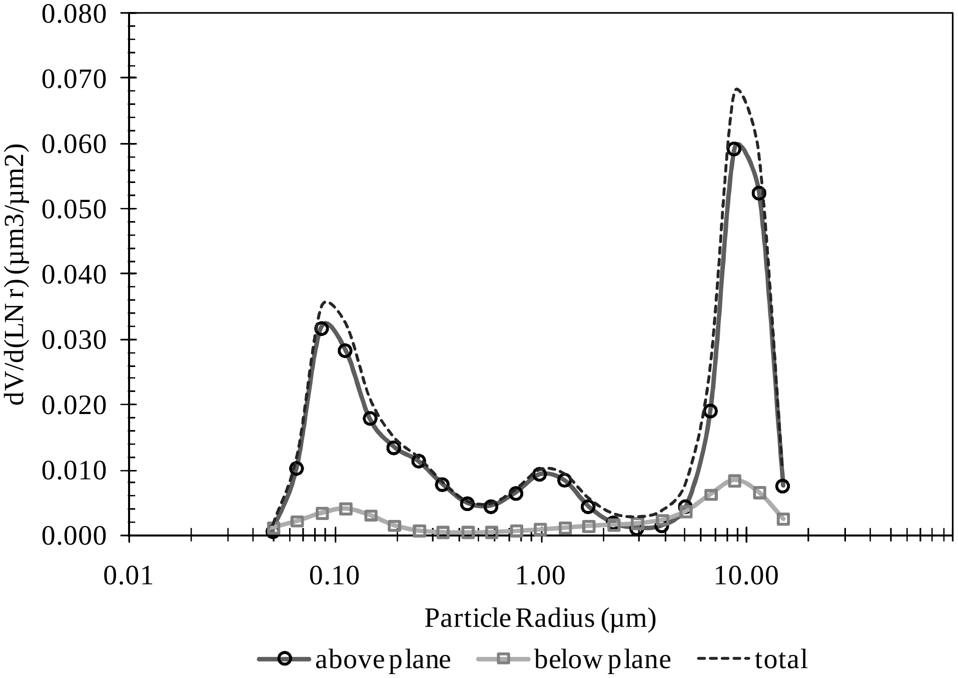

Figure 3.12. Aerosol column particle volume size distribution retrieved from the CAR at an altitude of 200 m above ground level at the SGP-CF during CLASIC Flight #1928 on 24 June 2007 (Gatebe et al. 2009).

Aerosol retrievals were also obtained at flight level by applying a sun photometric size distribution, which was derived using a flexible inversion algorithm that uses simultaneous retrievals of aerosol and surface optical properties from direct and diffuse radiometric measurements available from both the CAR and AERONET instruments (Dubovik and King 2000; Gatebe et al. 2009). We thus estimated a complex refractive index $n(\lambda) = 1.3606 - 0.021i$ and obtained aerosol column particle size parameters at 22 levels (Figure 3.12).

The total column water vapor $q = 1.42$ g cm^{-2} (0.62 g cm^{-2} above the aircraft) was also obtained from ground-based and airborne sun photometer measurements, and an O_3

column amount was assumed to be 344 m atm cm. Due to the technical limits of 6SV in performing robust atmospheric correction for data acquired at very large view angles, we constrained our own retrievals from CLASIC Flight #1928 to data collected at pixel viewing zenith angles $\theta_v < 75°$.

3.4.1.4. RossThick-LiSparseReciprocal BRDF Model Inversions

The RTLSR BRDF kernel model parameters were obtained by iterating between the directional reflectance retrievals available for each CAR pixel, and the RossThick volume scattering (K_{VOL}) and LiSparse-Reciprocal geometric scattering (K_{GEO}) kernel values, until the modeled calculated reflectances $R(\theta_v)$ matched the observed retrievals $\rho(\theta_v)$ (Strahler et al. 1999). The kernel fit to the directional surface reflectance data uses a least mean square estimate of the kernel coefficients; thus, a vector of kernel coefficients, f_k, can be expressed by using a simple matrix inversion:

$$\begin{aligned} R(\theta_v) &= \left(\left[H_k(\theta_v)' H_k(\theta_v) \right]^{-1} H_k(\theta_v)' \right) \rho(\theta_v) \\ &= \sum f_k H_k(\theta_v) \end{aligned} \tag{3.12}$$

$$e^2 = \frac{\sum_n \left(\rho(\theta_v) - R(\theta_v) \right)^2}{n} \tag{3.13}$$

Where $\rho(\theta_v)$ is a *1 x n* matrix, representing the column vector of *n* measured directional surface reflectances and *H* is an *m x n* matrix, representing the column vectors of the *m* kernels values for each of the *n* measurement geometries. The iteration was repeated a number of times for each CAR band until $e^2 < 10^{-5}$. Note that H_k, f_k, R, and ρ depend on the same set of wavelength (Λ) and geometric parameters (θ_s, $\Delta\phi$), so those subscripts have been omitted from the above equations.

3.4.1.5. Narrowband to Broadband Conversion

The spectral acquisitions from the CAR can be combined via Narrowband-to-broadband (NTB) conversion routines to provide broadband anisotropy information and thus broadband albedos similar to those that are routinely collected by field albedometers over the visible (0.3 - 0.7 μm), shortwave infrared (0.7 - 5.0 μm), and full solar range (0.3 - 5.0 μm). In MODIS data processing, the methodology for estimating broadband albedo and reflectance anisotropy retrievals are based on empirical relations between surface total shortwave albedo measurements and MODIS observations was introduced by Liang (2001) and validated in Liang et al. (2003). Using the same principle, narrowband spectral albedos were generated for each of the CAR's spectral response functions by determining the downward fluxes (i.e. direct and diffuse) using a selection of surface reflectance spectra under specific atmospheric conditions, at several heights above ground level (e.g. 200 m, 600 m, 2.0 km, and ~4.0 km), and solar zenith angles corresponding to CLASIC Flight #1928. Broadband albedos were then derived by calculating the ratio of broadband upwelling radiative flux to broadband downwelling flux *D*,

$$F(\theta_s)_{BB} = \frac{\int_{\lambda_1}^{\lambda_2} a(\theta_s,\lambda)D(\theta_s,\lambda,\tau_{0.55\mu m})d\lambda}{\int_{\lambda_1}^{\lambda_2} D(\theta_s,\lambda,\tau_{0.55\mu m})d\lambda} . \quad (3.14)$$

We used a library of 50 surface reflectance spectra from representative land covers of the SGP region and employed the Santa Barbara DISORT Atmospheric Radiative Transfer (SBDART) code (Ricchiazzi et al. 1998) to perform the model simulations. This particular scheme produced ~56000 scenarios. Regression analyses were then conducted using these samples to generate a set of conversion formulae applied uniformly to the broadband albedo and reflectance anisotropy retrievals derived from the CAR:

$$F(\theta_s)_{BB} = \sum_i c_i a(\theta_s,\lambda_i). \quad (3.15)$$

3.5. Results from Observations at the ARM-SGP Central Facility

3.5.1. Narrowband BRDF Retrievals of Archetypal Landscapes

Figure 3.13 shows spectral response curves of the RTLSR BRDF model parameters, $f_{iso}(\Lambda)$, $f_{vol}(\Lambda)$, and $f_{geo}(\Lambda)$, for each of the representative land covers that encompass the region surrounding the ARM-Southern Great Plains Central Facility (SGP-CF). These retrievals were collected by superimposing each of the land cover fields (Figure 3.5) against geo-referenced retrievals from the CAR using the 50 m and 100 m spatial grids. Image filtering functions were used to identify samples, for each land cover class, where a coincident number of high-quality retrievals were obtained at both spatial scales.

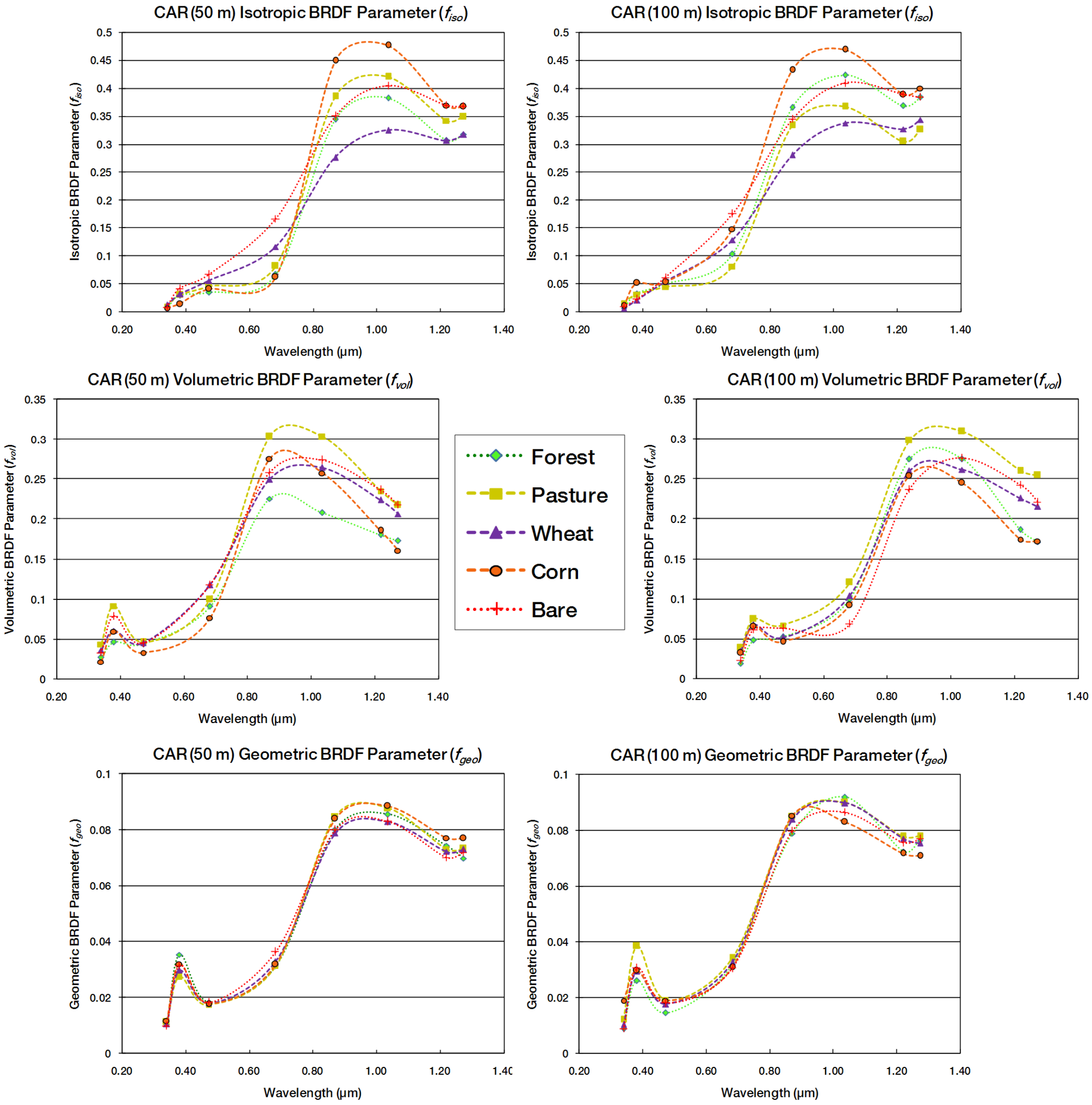

Figure 3.13. Spectral curves of the RTLSR BRDF model parameters over selected CAR channels for each of the representative land covers across the SGP-CF region. The BRDF inversions were derived at different spatial scales using independent retrievals from 50 m and 100 m spatial grids (left and right, respectively).

Results indicate that the corn and pasture classes exhibited the most anisotropic behavior, with notable increases in the volumetric and geometric parameters across all wavelengths. The spectral shapes of the RTLSR BRDF model parameters appear to be consistent at increased scales of resolution, with only a few sensitivities in the NIR for the pasture and forest class, and some changes in the visible domain for the corn class.

Figure 3.14 shows polar plots of the spectral BRDFs for CAR channels #4 (Λ = 0.682 μm), #5 (Λ = 0.870 μm), and #7 (Λ = 1.219 μm) using the same spatial grids and land cover schemes as Figure 3.13. The viewing zenith angle is represented as the radial distance from the center and the azimuth angle as the length of the arc on the respective zenith circle. The principal plane resides in the 0° – 180° azimuthal plane with the Sun located in the 0° azimuthal direction. With this definition, the upper half circle represents the backscattering (or hot-spot) region and the lower half circle represents the forward scattering region. A solar zenith angle, $\theta_s = 30°$, was used to generate the geometric (or kernel) functions (i.e. K_{VOL} and K_{GEO}) for each of the representative BRDFs. The hot-spot region is a common feature observed over all land cover classes. This effect occurs when canopy components (e.g. leaves, stems, and trunks) hide their own shadows; thus, making the scene appear bright due to maximal single scattering (Wanner et al. 1997). Conversely, the forward scattering region appears darker due to increase of mutual shadowing and shadow-casting between surface elements (Lucht et al. 2000). Note that the wheat class did not reflect strongly in the backscattering direction. This is because the majority of the winter-wheat fields that were sampled (~89%) had already been harvested at the time of Flight #1928. However those regions identified as the bare class actually did exhibit an increase in reflectance in the backscattering direction. Further investigations surmises that these effects are mostly due to sampling of furrowed soils as well as mixing of small clumps of vegetation (e.g. weed and grass) (see Figure 3.15). Results, indicate a small increase in the backscattering direction for most land covers. With the exception of the corn class at $\Lambda = 0.682$ μm, the BRDF was nearly invariable in the forward scattering plane. Table 3.2 shows comparisons between the 50 m and 100 m spectral BRDF retrievals from the CAR. The absolute RMSE (in reflectance units) and relative RMSE were calculated for each case. The 100 m retrievals of the representative BRDFs in the SGP-CF were consistently within the range of the 50 m retrievals by 0.0298, 0.0232, 0.0312 units of absolute RMSE (in reflectance units) for CAR channels #4, #5, and #7, respectively.

The highest difference between scales was recorded on CAR channel #4 for the corn class, where the 100 m BRDF retrievals overestimated the 50 m retrievals by 0.0879 RMSE. This trend appears to have been caused by a sudden change in the isotropic parameter, which nearly doubled in magnitude as the scales increased (see Figure 3.13). These differences are caused by a mixed signal between corn fields at different growth stages. In particular, the taller corn fields appear to be more dominant when the corn class is resolved at lower spatial resolutions (100 m).

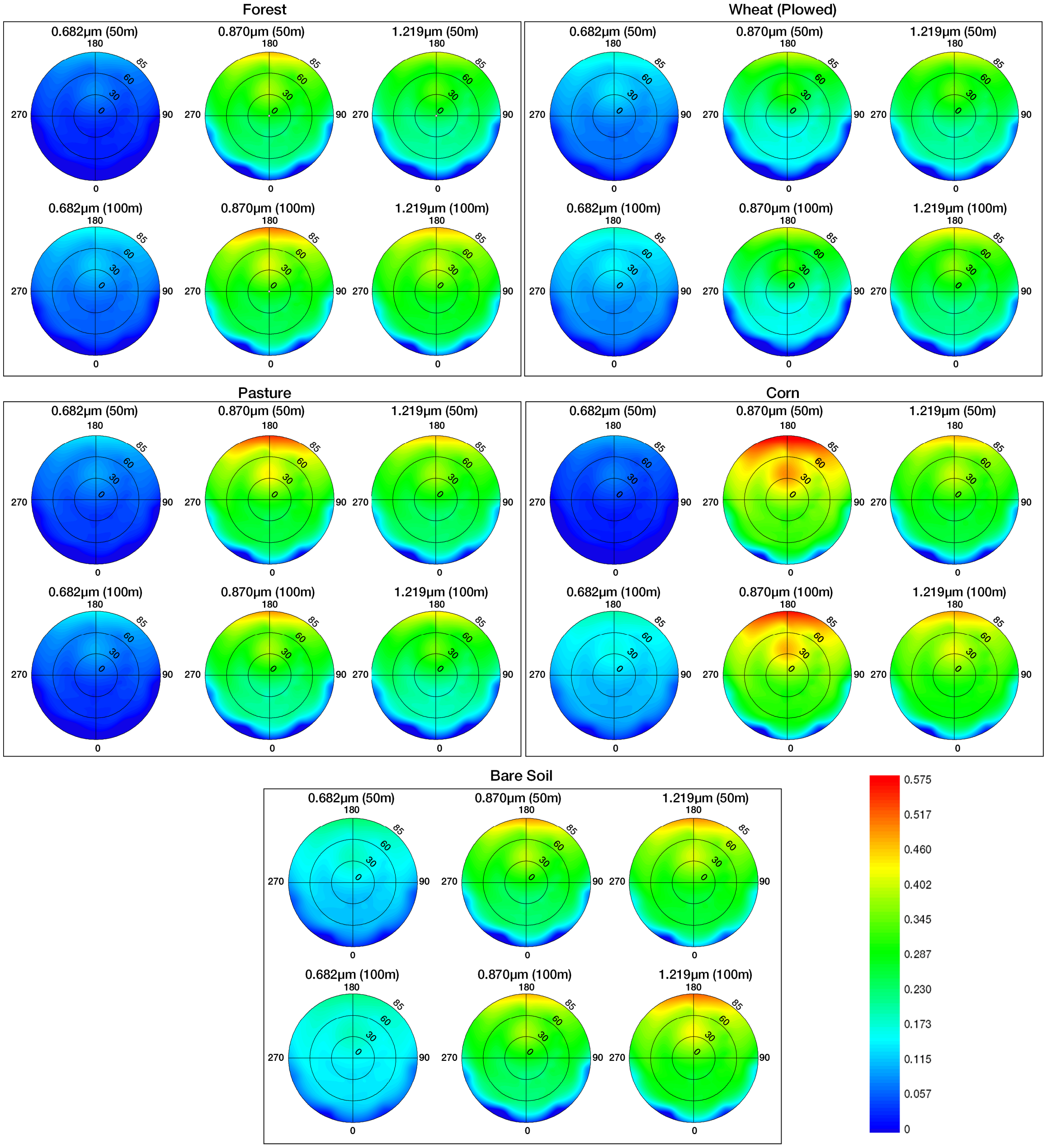

Figure 3.14. Spectral BRDFs for selected CAR channels #4 (Λ = 0.682 μm), #5 (Λ = 0.870 μm), and #7 (Λ = 1.219 μm), obtained at 50 m and 100 m over each of the representative land covers across the SGP-CF region. In all polar plots, the solar zenith angle $\theta_s = 30°$, the view zenith angle is represented as the radial distance from the center, and the azimuth as the length of arc on the respective zenith circle. The principal plane resides in the 0° – 180° azimuthal plane with the Sun located in the 180° azimuthal direction.

Table 3.2. Comparative results between CAR channels #4 ($\Lambda = 0.682$ μm), #5 ($\Lambda = 0.870$ μm), and #7 ($\Lambda = 1.219$ μm) using 50 m and 100 spatial grids over the representative land covers across the SGP-CF region. The absolute RMSE is in units of reflectance.

50m vs. 100m (0.682 μm)		
ID	Abs. RMSE	Rel. RMSE
Forest	0.0365	18.86%
Pasture	0.0038	6.79%
Wheat	0.0118	13.39%
Corn	0.0879	24.13%
Bare	0.0155	11.55%

50m vs. 100m (0.870 μm)		
ID	Abs. RMSE	Rel. RMSE
Forest	0.0247	9.04%
Pasture	0.0521	16.64%
Wheat	0.0032	1.54%
Corn	0.0196	5.22%
Bare	0.0070	2.49%

50m vs. 100m (1.036 μm)		
ID	Abs. RMSE	Rel. RMSE
Forest	0.0635	26.45%
Pasture	0.0407	14.61%
Wheat	0.0162	6.64%
Corn	0.0246	8.22%
Bare	0.0148	4.80%

3.5.2. Broadband BRDF Retrievals from CAR and MODIS

Figure 3.15 shows CAR reflectance anisotropy subsets, using 50 m spatial grids, alongside a matching set of true-color subsets from a 2.4 m QuickBird scene acquired on 1 July, 2007 over selected areas within the SGP-CF study sections. The colors on each of the CAR subsets describe the isotropic weighting of the RTLSR BRDF parameters in the visible (VIS) (0.3 - 0.7 μm), shortwave infrared (NIR) (0.7 - 5.0 μm), and full solar range (SWIR) (0.3 - 5.0 μm) (i.e. R-G-B → $f_{\text{iso,VIS}}$ - $f_{\text{iso,NIR}}$ - $f_{\text{iso,SWIR}}$) using BRDF model inversions from data acquired during CLASIC Flight #1928. Red arrows point to road intersections between the mapped positions and the QuickBird scene, as well as the location of the Central Facility’s 60 m radiation tower (bottom-right). For the 50 m CAR subsets, pasture and corn fields are seen in shades of blue-green (both light and dark tones), bare areas and plowed fields are seen in light-pink, winter wheat (unplowed) fields are seen in dark red, and data gaps are seen in white.

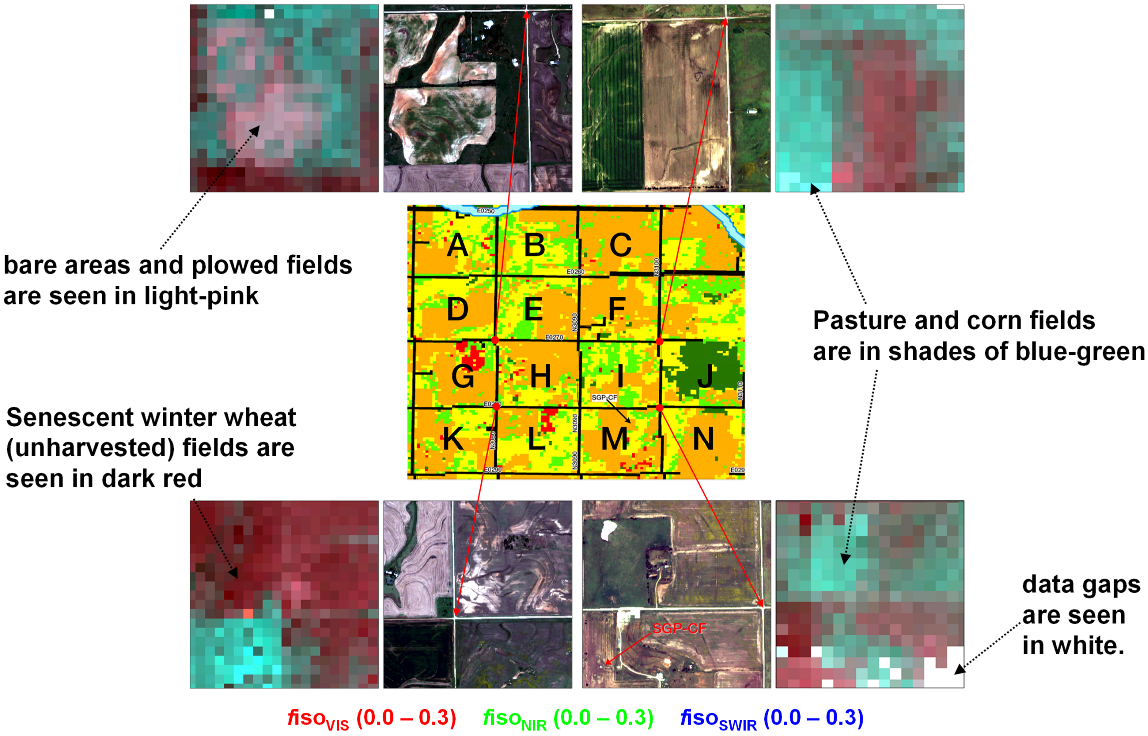

Figure 3.15. CAR 50 m reflectance anisotropy subsets, from BRDF model inversions derived using data acquired during CLASIC Flight #1928, displayed alongside true-color subsets from a 2.4 m QuickBird scene acquired on 7/1/2007, for selected areas within the SGP-CF study domain.

The degree of convergence between the CAR retrievals, as seen at local (~2.4 m) scales, suggests that the processing of CAR BRDFs, including the geometric correction, scaling, and narrowband to broadband conversions, was consistent throughout the study area. Table 3.3 and Table 3.4 provide results for the broadband BRDF model inversions derived from the CAR, using both 50 m and 100 m spatial grids, as well as the MODIS (V005) 500 m BRDF retrievals (MCD43A1), for each of the 14 sections that were sampled during Flight #1928.

Table 3.3. RTLSR BRDF model parameters [$f_{iso}(\Lambda)$, $f_{vol}(\Lambda)$, $f_{geo}(\Lambda)$] derived from the CAR, using 50 m and 100 spatial grids, and MODIS V005 retrievals in the visible (0.3 - 0.7 μm), NIR (0.7 - 5.0 μm), and full solar range (SWIR) (0.3 - 5.0 μm), for the upper-level sections (*A* – *F*) that were sampled during Flight #1928.

	QUAD A	**QUAD B**	**QUAD C**
	CAR-BRDF (50 m)	**CAR-BRDF (50 m)**	**CAR-BRDF (50 m)**
$BRDF_{VIS}$	N.A.	N.A.	N.A.
$BRDF_{NIR}$	N.A.	N.A.	N.A.
$BRDF_{SWIR}$	N.A.	N.A.	N.A.
	CAR-BRDF (100 m)	**CAR-BRDF (100 m)**	**CAR-BRDF (100 m)**
$BRDF_{VIS}$	[0.0113, 0.0279, 0.0087]	[0.0133, 0.0220, 0.0093]	[0.0149, 0.0261, 0.0098]
$BRDF_{NIR}$	[0.3004, 0.0912, 0.0158]	[0.3073, 0.0921, 0.0162]	[0.2555, 0.0922, 0.0167]
$BRDF_{SWIR}$	[0.2034, 0.0676, 0.0141]	[0.2079, 0.0600, 0.0151]	[0.1773, 0.0640, 0.0161]
	MODIS (500 m)	**MODIS (500 m)**	**MODIS (500 m)**
$BRDF_{VIS}$	[0.0151, 0.0450, 0.0151]	[0.0125, 0.0450, 0.0125]	[0.0202, 0.0426, 0.0202]
$BRDF_{NIR}$	[0.2822, 0.1484, 0.0395]	[0.2700, 0.1598, 0.0372]	[0.2735, 0.1474, 0.0461]
$BRDF_{SWIR}$	[0.1872, 0.0891, 0.0264]	[0.1798, 0.0951, 0.0241]	[0.1885, 0.0867, 0.0321]

	QUAD D	**QUAD E**	**QUAD F**
	CAR-BRDF (50 m)	**CAR-BRDF (50 m)**	**CAR-BRDF (50 m)**
$BRDF_{VIS}$	[0.0135, 0.0253, 0.0093]	[0.0133, 0.0258, 0.0093]	[0.0141, 0.0331, 0.0096]
$BRDF_{NIR}$	[0.2780, 0.0942, 0.0160]	[0.2808, 0.1384, 0.0167]	[0.2523, 0.1321, 0.0169]
$BRDF_{SWIR}$	[0.1875, 0.0615, 0.0151]	[0.1849, 0.0754, 0.0149]	[0.1690, 0.0699, 0.0153]
	CAR-BRDF (100 m)	**CAR-BRDF (100 m)**	**CAR-BRDF (100 m)**
$BRDF_{VIS}$	[0.0158, 0.0182, 0.0086]	[0.0143, 0.0212, 0.0081]	[0.0121, 0.0289, 0.0083]
$BRDF_{NIR}$	[0.3215, 0.0633, 0.0165]	[0.2897, 0.0672, 0.0161]	[0.2536, 0.0826, 0.0166]
$BRDF_{SWIR}$	[0.2153, 0.0430, 0.0141]	[0.1917, 0.0506, 0.0134]	[0.1675, 0.0576, 0.0131]
	MODIS (500 m)	**MODIS (500 m)**	**MODIS (500 m)**
$BRDF_{VIS}$	[0.0161, 0.0488, 0.0161]	[0.0155, 0.0404, 0.0154]	[0.0156, 0.0300, 0.0138]
$BRDF_{NIR}$	[0.2857, 0.1618, 0.0384]	[0.2955, 0.1332, 0.0467]	[0.2447, 0.0919, 0.0392]
$BRDF_{SWIR}$	[0.1899, 0.1027, 0.0254]	[0.1977, 0.0820, 0.0305]	[0.1664, 0.0596, 0.0231]

Table 3.4. RTLSR BRDF model parameters $[f_{iso}(\Lambda), f_{vol}(\Lambda), f_{geo}(\Lambda)]$ for the lower-level sections (*G* – *N*) that were sampled during Flight #1928. Setup is the same as Table 3.3.

	QUAD G	**QUAD H**	**QUAD I**	**QUAD J**
	CAR-BRDF (50 m)	**CAR-BRDF (50 m)**	**CAR-BRDF (50 m)**	**CAR-BRDF (50 m)**
BRDF_{VIS}	[0.0142, 0.0249, 0.0096]	[0.0171, 0.0251, 0.0085]	[0.0143, 0.0185, 0.0084]	[0.0123, 0.0236, 0.0086]
BRDF_{NIR}	[0.2761, 0.0894, 0.0147]	[0.2849, 0.0908, 0.0139]	[0.2973, 0.0747, 0.0159]	[0.3286, 0.1231, 0.0267]
$\text{BRDF}_{\text{SWIR}}$	[0.186, 0.0602, 0.0152]	[0.1926, 0.0574, 0.0138]	[0.1987, 0.0487, 0.0137]	[0.2170, 0.0776, 0.0159]
	CAR-BRDF (100 m)	**CAR-BRDF (100 m)**	**CAR-BRDF (100 m)**	**CAR-BRDF (100 m)**
BRDF_{VIS}	[0.0375, 0.0644, 0.0334]	[0.0180, 0.0348, 0.0096]	[0.0132, 0.0593, 0.0215]	[0.0092, 0.0304, 0.0075]
BRDF_{NIR}	[0.3829, 0.1822, 0.0361]	[0.3273, 0.0888, 0.0170]	[0.2792, 0.1406, 0.0258]	[0.2686, 0.0779, 0.0148]
$\text{BRDF}_{\text{SWIR}}$	[0.2559, 0.1179, 0.0460]	[0.2245, 0.0718, 0.0156]	[0.1860, 0.1216, 0.0337]	[0.1708, 0.0696, 0.0129]
	MODIS (500 m)	**MODIS (500 m)**	**MODIS (500 m)**	**MODIS (500 m)**
BRDF_{VIS}	[0.0155, 0.0491, 0.0155]	[0.0197, 0.0350, 0.0196]	[0.0134, 0.0514, 0.0132]	[0.0108, 0.0543, 0.0108]
BRDF_{NIR}	[0.2953, 0.1446, 0.0489]	[0.2942, 0.1569, 0.0442]	[0.2800, 0.1468, 0.0349]	[0.2462, 0.1548, 0.0226]
$\text{BRDF}_{\text{SWIR}}$	[0.1925, 0.0940, 0.0309]	[0.2001, 0.0904, 0.0294]	[0.1860, 0.0914, 0.0230]	[0.1649, 0.1028, 0.0161]

	QUAD K	**QUAD L**	**QUAD M**	**QUAD N**
	CAR-BRDF (50 m)	**CAR-BRDF (50 m)**	**CAR-BRDF (50 m)**	**CAR-BRDF (50 m)**
BRDF_{VIS}	[0.0082, 0.0139, 0.0086]	[0.0141, 0.0285, 0.0087]	[0.0182, 0.0343, 0.0095]	[0.0133, 0.0335, 0.0081]
BRDF_{NIR}	[0.2692, 0.0896, 0.0170]	[0.2935, 0.1184, 0.0151]	[0.3053, 0.1426, 0.0177]	[0.3624, 0.1373, 0.0230]
$\text{BRDF}_{\text{SWIR}}$	[0.1733, 0.0524, 0.0139]	[0.1930, 0.0765, 0.0139]	[0.2034, 0.0908, 0.0153]	[0.2373, 0.0980, 0.0147]
	CAR-BRDF (100 m)	**CAR-BRDF (100 m)**	**CAR-BRDF (100 m)**	**CAR-BRDF (100 m)**
BRDF_{VIS}	N.A.	N.A.	N.A.	N.A.
BRDF_{NIR}	N.A.	N.A.	N.A.	N.A.
$\text{BRDF}_{\text{SWIR}}$	N.A.	N.A.	N.A.	N.A.
	MODIS (500 m)	**MODIS (500 m)**	**MODIS (500 m)**	**MODIS (500 m)**
BRDF_{VIS}	[0.0156, 0.0469, 0.0156]	[0.0162, 0.0504, 0.0162]	[0.0178, 0.0491, 0.0178]	[0.0142, 0.055, 0.0142]
BRDF_{NIR}	[0.2816, 0.1607, 0.0388]	[0.2847, 0.1697, 0.0376]	[0.2837, 0.1845, 0.0343]	[0.2754, 0.1839, 0.031]
$\text{BRDF}_{\text{SWIR}}$	[0.1876, 0.0967, 0.0266]	[0.1886, 0.1021, 0.0258]	[0.1913, 0.1071, 0.0259]	[0.1841, 0.1114, 0.022]

Table 3.5. RTLSR BRDF model parameters $[f_{iso}(\Lambda), f_{vol}(\Lambda), f_{geo}(\Lambda)]$ derived using areal-mean estimates representative of the highest-quality sample sections within the SGP-CF region (see Figure 3.11). Setup is the same as Table 3.3.

	ALL SECTIONS (Areal Mean)		
	CAR-BRDF (50 m)	**CAR-BRDF (100 m)**	**MODIS-BRDF (500 m)**
BRDF_{VIS}	[0.0141, 0.0253, 0.0090]	[0.0141, 0.0298, 0.0105]	[0.0147, 0.040, 0.0146]
BRDF_{NIR}	[0.2827, 0.1101, 0.0162]	[0.2818, 0.0898, 0.0176]	[0.2543, 0.1407, 0.0351]
$\text{BRDF}_{\text{SWIR}}$	[0.1878, 0.0666, 0.0145]	[0.1967, 0.0670, 0.0169]	[0.1703, 0.0833, 0.0235]

Table 3.5 also provides results for the RTLSR BRDF model parameters derived using areal-mean estimates representative of all the sample sections within the SGP-CF region that have the highest number of directional signatures near the principal plane (see Figure 3.11); and Figure 3.16 shows the respective polar plots for this particular case. A solar zenith angle, $\theta_s = 30°$, was used to generate the kernel functions for each of the representative BRDFs.

As in the previous section, image filtering functions were used to locate all the samples, within each individual quadrant and for the entire study area, where a coincident number of high-quality retrievals were being resolved at both the CAR 50 m and 100 m scales. Given the large size of the sampled sections (ranging from 1.6 km^2 – 2.0 km^2), a direct comparison between the CAR and MODIS (500 m) retrievals over these regions provides the opportunity to evaluate the ability of the MODIS data to reproduce areal-mean estimates of surface BRDFs that are representative of areas comparable to small image arrays consisting of 4-16 MODIS grids, and for the full study region. Table 3.6 to Table 3.8 provide results comparing the CAR and MODIS BRDF retrievals in the VIS (Table 3.6), NIR (Table 3.7) and SWIR (Table 3.8) broadbands, for each of the study sections that were sampled during Flight #1928, as well as the entire study area.

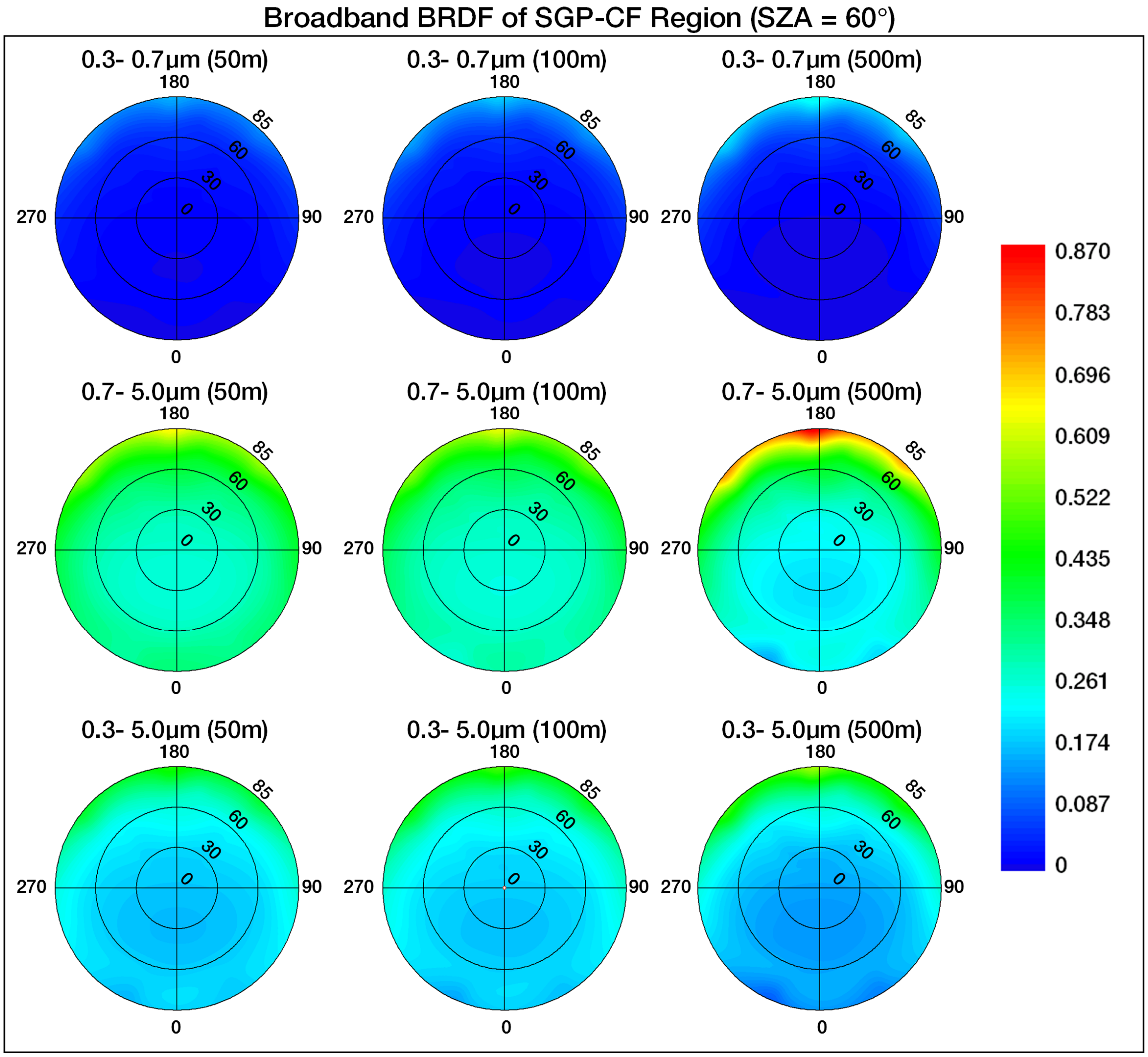

Figure 3.16. Broadband BRDFs (with solar zenith angle, θ_s = 30°) obtained at different spatial scales (i.e. 50 m, 100 m, and 500 m) for areal-mean estimates representative of the entire set of sections in the SGP-CF region.

Comparisons between the MODIS and 50 m CAR BRDFs suggest that the degree of correspondence between these two scales was slightly better (by 0.0005, 0.0052, and 0.0029 absolute RMSE for the VIS, NIR, and SWIR, respectively) than the equivalent estimates between MODIS and CAR retrievals at 100 m scales. However, MODIS results over study sections where the 100 m CAR grids obtained a much higher number of retrievals near the principal plane, e.g. *F*, and *I*, (see Figure 3.11), were more consistent by 0.0004, 0.0252, 0.0169 RMSE for the VIS, NIR, and SWIR, respectively.

While the results on Figure 3.16 appear to show an underestimation of the MODIS BRDF retrievals in the NIR and SWIR bands, this interpretation must be exercised with caution. Note that the absolute accuracy requirements of ±0.02-0.05 units for albedo, as proposed by Henderson-Sellers and Wilson (1983) and Sellers et al. (1995), are meant to evaluate the efficiency of surface albedo and reflectance anisotropy retrievals in the full solar range (i.e. 0.3 - 5.0 μm). However, when assessing BRDF results across different spectral ranges, the relative RMSE is a much more appropriate measure of accuracy, because it provides the error associated to differences in spatial scales relative to the mean reflectance value obtained for each band. On average, results for the representative BRDFs of the entire study area (Figure 3.16) show a relative RMSE of 21.16%, 13.54%, and 12.38% for the VIS, NIR, and SWIR broadbands; which suggests that the errors due to scaling of BRDF retrievals are more prone to be in the visible portion of the spectrum. Looking at the visible broadband results on Figure 3.16, it appears that the BRDF, becomes more sensitive to changes in the backscattering region and, consequently, to variations in solar zenith angle as we upscale to a MODIS grid.

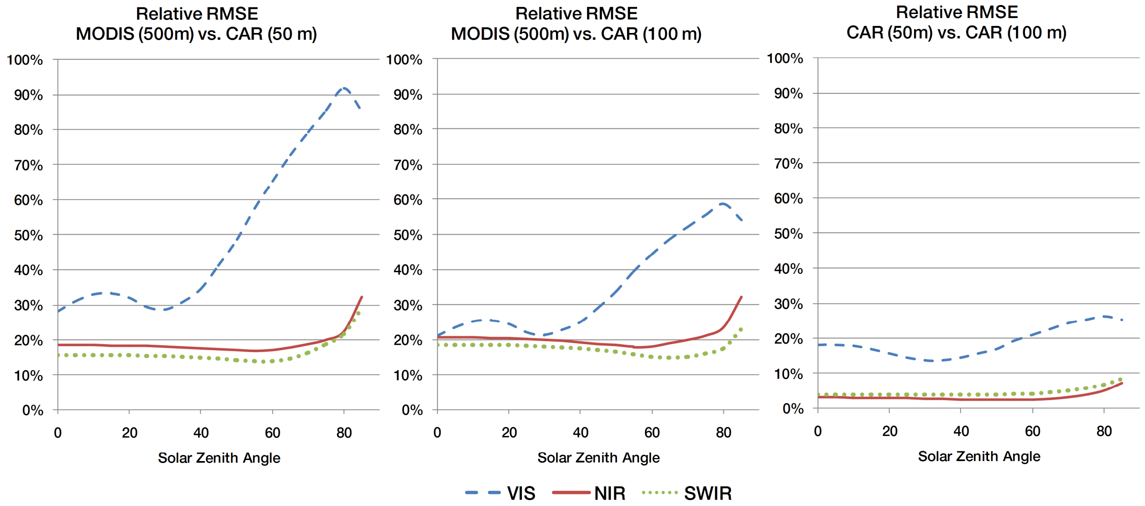

Figure 3.17. Comparisons between the relative RMSEs of BRDF retrievals at different scales of resolution, i.e. 500 m vs. 50 m (left); 500 m vs. 100 m (center); and 50m vs. 100 m (right), plotted as a function of solar zenith angle for the visible (dashed line), NIR (solid line), and SWIR (dotted line). The BRDFs were extracted from areal-mean estimates representative of the entire set of sections in the SGP-CF region (see Figure 3.15).

Figure 3.17 examines this relationship by comparing the relative RMSEs of BRDF retrievals obtained at different scales of resolution, (i.e. 500 m vs. 50 m, 500 m vs. 100 m, and 50m vs. 100 m) as a function of solar zenith angle. Note that both the NIR and SWIR broadbands hold on well as the underlying anisotropy is specified as a function of scale and solar geometry. The magnitude of the relative RMSE was further reduced at closer retrieval scales (i.e. 50m vs. 100m). However, the visible broadband exhibited a significant decline in accuracy, both as a function of retrieval scale and solar geometry. The fact that an increase in the magnitude of the directional reflectance is consistently being captured at different scales of resolution may further suggest the presence of a non-linear trend in the degradation of modeled reflectances; particularly in the visible domain.

Table 3.6. Comparative results between the broadband BRDFs derived from the CAR, using 50 m and 100 spatial grids, and MODIS retrievals in the visible (0.3 - 0.7 μm) broadband, over all sampled sections (*A* – *N*) and using all sections.

	50m vs. 500m (VIS)		100m vs. 500m (VIS)		50m vs. 100m (VIS)	
ID	Abs. RMSE	Rel. RMSE	Abs. RMSE	Rel. RMSE	Abs. RMSE	Rel. RMSE
A	-	-	0.0031	37.87%	-	-
B	-	-	0.0030	32.04%	-	-
C	-	-	0.0037	33.98%	-	-
D	0.0036	36.37%	0.0047	39.49%	0.0027	38.19%
E	0.0026	27.32%	0.0037	33.88%	0.0019	26.73%
F	0.0020	19.88%	0.0016	18.71%	0.0014	17.20%
G	0.0035	33.68%	0.0131	59.58%	0.0134	142.56%
H	0.0050	36.56%	0.0054	36.69%	0.0014	13.69%
I	0.0043	40.72%	0.0040	36.27%	0.0055	43.20%
J	0.0036	40.27%	0.0035	47.96%	0.0020	24.38%
K	0.0076	184.67%	-	-	-	-
L	0.0036	32.36%	-	-	-	-
M	0.0054	35.36%	-	-	-	-
N	0.0034	29.88%	-	-	-	-
ALL	0.0030	28.56%	0.0021	21.25%	0.0012	13.69%

Table 3.7. Comparative results between the broadband BRDFs derived from the CAR, using both 50 m and 100 spatial grids, and MODIS V005 retrievals in the NIR (0.7 - 5.0 μm) broadband, over all sampled sections (*A* – *N*) and using all sections.

	50m vs. 500m (NIR)		100m vs. 500m (NIR)		50m vs. 100m (NIR)	
ID	Abs. RMSE	Rel. RMSE	Abs. RMSE	Rel. RMSE	Abs. RMSE	Rel. RMSE
A	-	-	0.0441	15.31%	-	-
B	-	-	0.0585	19.86%	-	-
C	-	-	0.0244	10.06%	-	-
D	0.0217	8.19%	0.0575	18.70%	0.0419	15.77%
E	0.0280	10.40%	0.0327	11.85%	0.0112	4.14%
F	0.0371	15.41%	0.0360	14.98%	0.0063	2.64%
G	0.0291	11.00%	0.1030	29.13%	0.0907	34.24%
H	0.0300	10.93%	0.0619	19.73%	0.0392	14.28%
I	0.0373	13.13%	0.0107	4.15%	0.0275	9.69%
J	0.0770	25.14%	0.0292	11.37%	0.0507	16.54%
K	0.0189	7.41%	-	-	-	-
L	0.0344	12.16%	-	-	-	-
M	0.0391	13.33%	-	-	-	-
N	0.0936	27.16%	-	-	-	-
ALL	0.0487	18.00%	0.0552	19.88%	0.0074	2.74%

Table 3.8. Comparative results between the broadband BRDFs derived from the CAR, using both 50 m and 100 spatial grids, and MODIS V005 retrievals in the SWIR (0.3 - 5.0 μm) broadband, over all sampled sections (*A* – *N*) and using all sections.

	50m vs. 500m (SWIR)		100m vs. 500m (SWIR)		50m vs. 100m (SWIR)	
ID	Abs. RMSE	Rel. RMSE	Abs. RMSE	Rel. RMSE	Abs. RMSE	Rel. RMSE
A	-	-	0.0294	15.35%	-	-
B	-	-	0.0367	18.80%	-	-
C	-	-	0.0127	7.79%	-	-
D	0.0108	6.21%	0.0361	17.80%	0.0281	16.12%
E	0.0121	6.98%	0.0165	9.17%	0.0080	4.61%
F	0.0127	8.12%	0.0136	8.67%	0.0021	1.36%
G	0.0145	8.41%	0.0502	23.48%	0.0468	27.04%
H	0.0139	7.68%	0.0392	18.53%	0.0307	16.99%
I	0.0220	11.81%	0.0129	8.22%	0.0344	18.43%
J	0.0513	25.17%	0.0090	5.62%	0.0435	21.34%
K	0.0109	6.73%	-	-	-	-
L	0.0180	9.90%	-	-	-	-
M	0.0237	12.37%	-	-	-	-
N	0.0604	26.68%	-	-	-	-
ALL	0.0269	15.29%	0.0328	18.03%	0.0067	3.81%

3.5.3. Diurnal Patterns of Surface Albedo as seen by CAR, MODIS, and Ground (Tower) Measurements

At the same time as the J-31 was orbiting the Central Facility during CLASIC Flight #1928, ground measurements at the nearby Radiometric Calibration Facility (RCF) recorded estimates of cloud fraction = 0.01, the upward-facing pyranometers (both clear and sun-shaded) estimated a diffuse/total ratio, $S(\theta_{s,}\tau_{0.55\mu m})$ = 0.2243, and a solar zenith angle θ_s = 63.73°. Actual (or blue-sky) albedo retrievals (SWIR 0.3 - 5.0 μm) from both the CAR and MODIS were then reconstructed by combining the intrinsic broadband albedo quantities (i.e. black-sky and white-sky) as a function of these particular atmospheric and solar illumination conditions (see Section 2.4.1).

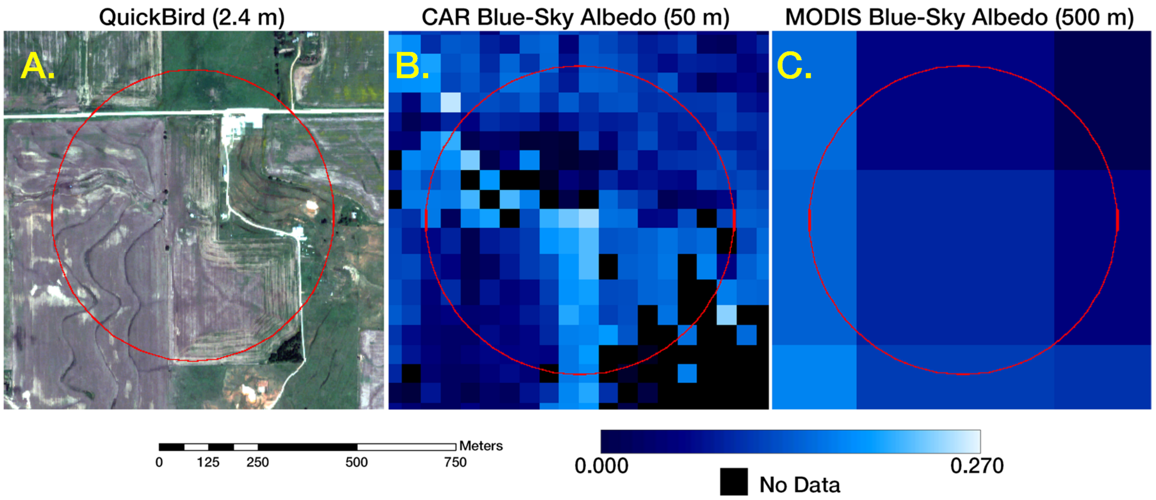

Figure 3.18. (A) A 1 km x 1 km Quickbird subset centered at the ARM-SGP Central Facility. Actual albedo retrievals at 50 m and 500 m from the CAR and MODIS (B and C, respectively), illustrate the specific conditions during CLASIC Flight #1928. The red circles denote the ground footprint as seen by the downward-facing pyranometer atop the 60 m radiation tower (≈ 750 m diameter).

Figure 3.18 (A) shows a 1 km x 1 km Quickbird subset, retrieved on 1 July 2007, centered at the ARM-SGP Central Facility. The retrievals of blue-sky albedo at 50 m and 500 m from the CAR and MODIS (B and C, respectively), illustrate the exact conditions when the CAR orbited the SGP-CF during CLASIC Flight #1928. The red circles denote the ground footprint as seen by the downward-facing pyranometer atop the 60 m radiation tower (≈ 750 m diameter). Results between the tower, CAR, and MODIS measurements, for the specific conditions observed at 7:30 AM (local time) during CLASIC Flight #1928, were 0.2150, 0.1918, 0.1793, respectively. For CAR and MODIS, the blue-sky albedos were determined based on the areally weighted averages of all retrievals within the circular footprint of the 60 m SGP-CF tower.

While the CAR obtained a BRDF retrieval over the SGP-CF in a manner of minutes, the MODIS retrievals were constructed based on a sparsely-filled estimate of the BRDF over a 16-day period that began on 18 June, 2007 (or 6 days before CLASIC Flight #1928). Accordingly, Figure 3.19 shows hourly retrievals of surface albedo acquired at the ARM-SGP Central Facility throughout the same 16-day period as the MODIS retrievals (i.e. 18 June, 2007 to 3 July, 2007). The tower albedo measurements (as seen in filled-diamonds) were compared against retrievals of blue-sky albedo derived from the CAR (open squares) and MODIS (filled triangles). These retrievals were also reconstructed by combining the black-sky and white-sky albedos as a function of the specific atmospheric and solar illumination conditions as seen in the ground for each of the 15-minute intervals. Since the MODIS V005 BRDF/Albedo product is routinely used as a clear-sky product, we also filtered the ground albedo records when estimates of cloud fraction at the SGP-CF were detected to be > 0.5.

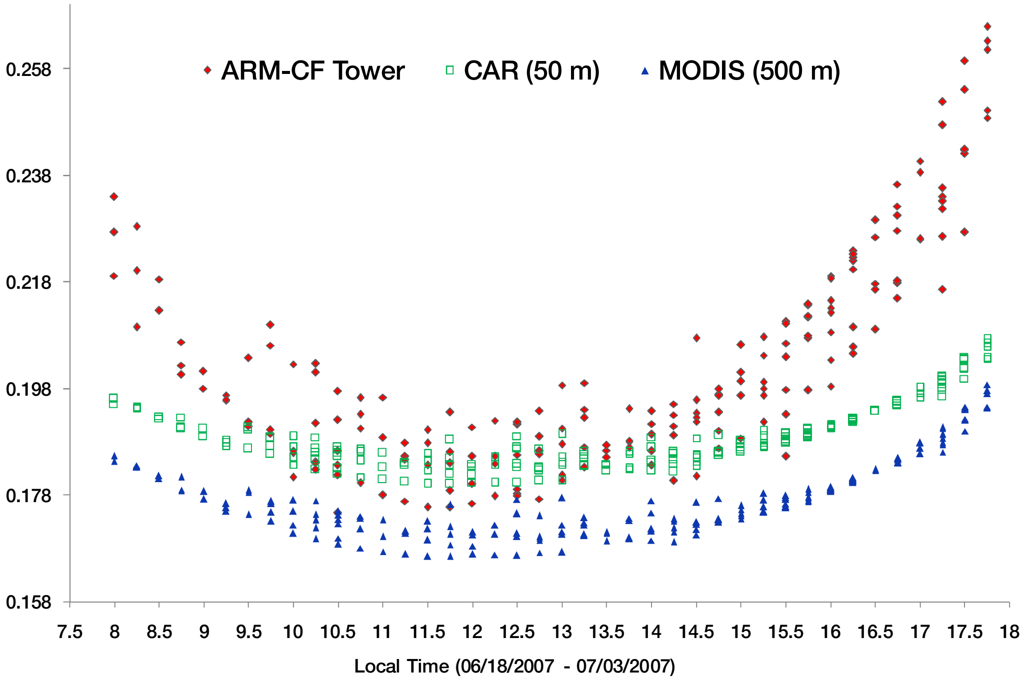

Figure 3.19. Comparisons between 15-minute retrievals of surface albedo derived from CAR 50 m retrievals (open squares), MODIS 500m retrievals (filled triangles), and tower measurements at the ARM Central Facility (filled diamonds) during a 16-day period from 06/18/2007 - 07/03/2007.

Results on Figure 3.19 show the usual “U-shaped” trend for albedo that reaches a minimum value around local solar noon time. Both the CAR and MODIS albedos performed very well at solar zenith angles < 70° (i.e. between the hours of 8:00 AM and 4:00 PM local time), but the retrievals consistently underestimated the tower albedo at SZA > 70° (or before 8:00 AM and after 4:00 PM local time). Overall, the CAR and MODIS retrievals for this 16-day period were within 0.0113 and 0.0168 units of absolute RMSE (for CAR and MODIS, respectively) for retrievals at SZA < 70°; and within 0.0417 and 0.0506 units of absolute RMSE for retrievals at solar zenith angles > 70°.

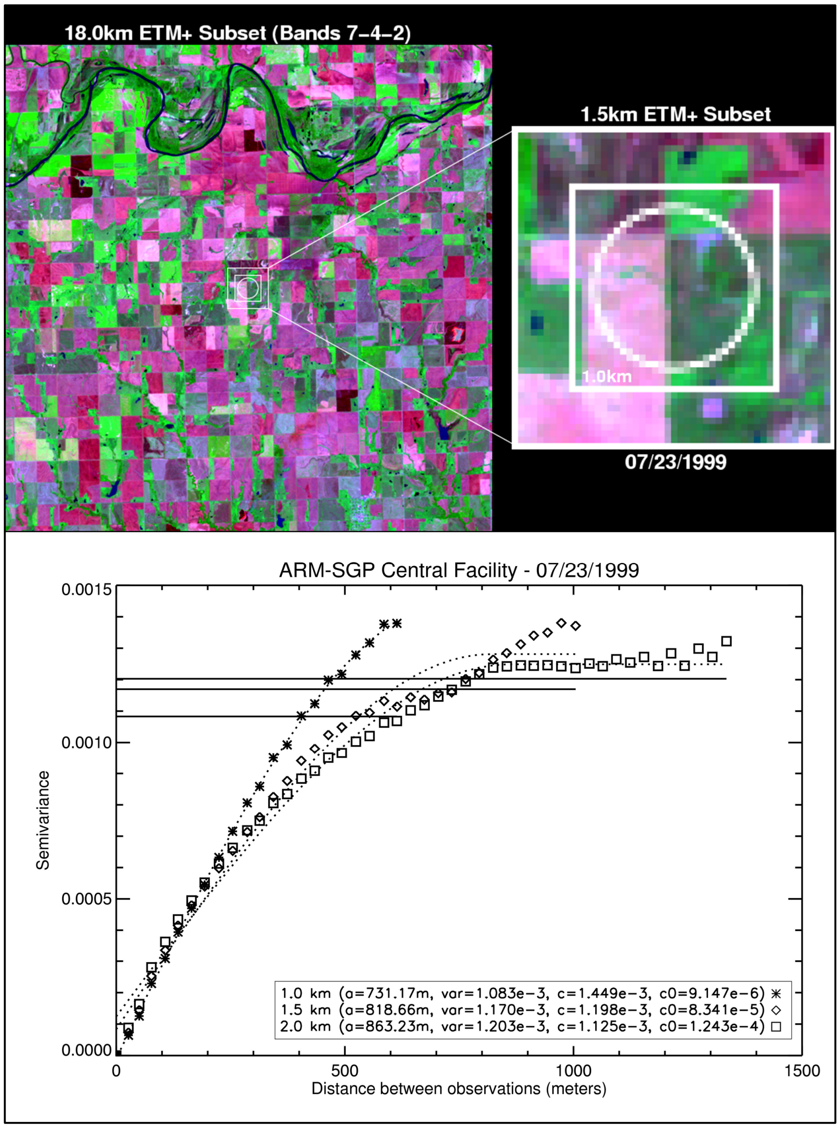

Figure 3.20. (Top) Top-of-Atmosphere (TOA) shortwave reflectance composites (ETM+ Bands 7-4-2) centered at the SGP-CF 60m radiation tower. Pasture fields and trees are in shades of green (both light and dark tones) and purple, crops and bare areas are seen in light-pink, light-lavender, magenta, and pale-pink, and water is seen in dark-blue and black. (Bottom) Variogram estimator (points), spherical model (dotted curves), and sample variance (solid straight lines) obtained over the ARM-SGP Central Facility using surface albedos derived from an ETM+ scene retrieved on 23 July, 1999 using regions of 1.0 km (asterisks), 1.5 km (diamonds), and 2.0 km (squares).

Unlike the CAR, which derives an albedo based on fine-scale retrievals of the BRDF, the MODIS V005 retrievals were reconstructed using a small array of larger pixels that are resolving, and are thus representative of, the landscapes surrounding the footprint of the SGP-CF. A recent assessment of the spatial representativeness over the SGP-Central Facility was performed by Román et al. (2009a). Results from this study indicate that the surface conditions inside the footprint of the SGP-CF 60 m radiation tower are slightly different from the surrounding region extending to the size of a MODIS grid cell. A further analysis of semivariogram functions at the ARM-SGP using a Landsat ETM+ scene retrieved on 23 July, 1999 resulted in an average path size (or range *a*) of 731 m (Figure 3.20). Since observations separated by distances larger than the range are spatially independent, these results suggest that a direct assessment between the tower albedos at the SGP-CF and MODIS retrievals at the native (500 m) resolutions could result in additional scaling errors. This may explain the negative biases of ~0.03 units seen in the MODIS albedo retrievals of as shown in Figure 3.19.

3.6. Conclusions

A new set of spatial transformation and scaling routines, whereby directional surface reflectances derived from NASA’s Cloud Absorption Radiometer (CAR) are efficiently transformed into image space, successfully recreate the measurement methodology, spatial coverage and data processing protocols employed by AVHRR-MODIS-NPP/NPOESS sensors. These characterizations provide a combination of one-of-a-kind maps of the underlying anisotropy and albedo of the land surface; hence providing a terrestrial perspective on applications of CAR data, in ways that have never been seen or understood before. Results over the ARM-SGP Central Facility during the 2007 Cloud and Land Surface Interaction Campaign (CLASIC), provide fine-scale retrievals of the BRDF, using 50 m and 100 m spatial grids for each of the representative land covers across the SGP-CF, over eight spectral bands, three broadbands, and including a number of quality assurance fields using a simple procedure that describes the confidence of a BRDF retrieval based on the total number of observations per CAR grid and the number of directional signatures obtained near the principal plane. These products are specifically useful for: (1) acquiring areally-weighted BRDFs and albedo retrievals from areas comparable to satellite footprints for shortwave radiation closure studies; (2) providing a ground-truth reference for validation and intercomparisons between current and future global surface albedo and reflectance anisotropy products derived from multiple satellite sensors; (3) exploring relationships between surface albedo and land-atmosphere interactions over the SGP-CF; and (4) improving specification of surface albedo for cloud property retrievals; all within a period when an intensive number of measurements from surface, airplane, and satellite platforms were performed.

Local upscaling results between the 50 m and 100 m BRDF retrievals from the CAR and the 500 m retrievals from MODIS show a good degree of correspondence between the three scales, with results being consistently under 0.05 absolute RMSE (in reflectance units) or 17% relative RMSE, for both the narrowband and broadband retrievals. However, results in the visible domain of the spectrum appear to be more sensitive to changes in the backscattering region of the BRDF hemisphere, and consequently, to solar zenith angle variations, particularly when a MODIS pixel (~ 500 m) is directly compared against the finer-scale retrievals from CAR.

The diurnal performance of the MODIS V005 BRDF/Albedo algorithm and CAR retrievals was evaluated using field measurements of albedo over the ARM-SGP Central Facility throughout the period of CLASIC. The overall accuracies of both the CAR and MODIS albedos were within 0.02 units of absolute RMSE, but show a decreasing trend with underestimation as the solar zenith angle increases to > 70°. These results confirm the untested prediction that the spatial degradation of modeled reflectances can be achieved through degradation of the RossThick-LiSparseReciprocal BRDF kernel model parameters. The spectral consistency of the BRDF model parameters, using both narrowband and broadband retrievals at increased scales of resolution, further suggests that the RTLSR model, and perhaps linear BRDF models in general, are capturing the underlying surface heterogeneities of the archetypal landscapes observed in this study.

Chapter 4

4. Development of a Confidence Layer for the MODIS BRDF/Albedo Product

4.1. Introduction

Thus far, this research has evaluated the ability of the MODIS V005 BRDF/Albedo products to capture the underlying spatial and seasonal variability on a per-pixel or single grid cell basis. In order to improve the parameterizations of albedo in regional and large-scale models, assessments are required at the multiple spatial scales at which MODIS data are commonly utilized. Use of ground measurements would require significant instrumental deployment in areas where in-situ data are scarce. Currently, there are few measurement sites with single tower albedometers or airborne retrievals that can be used for characterizing surface albedo and even fewer that provide a spatially representative number of field samples distributed across a single region. To address these challenges, this chapter focuses on both local and regional assessments based on daily comparisons between MODIS and surface albedo fields reconstructed using a combination of in-situ measurements. To further close the scaling gaps between the point-based and region-based assessments of spatial representativeness for surface albedo, a methodology has been developed to establish whether a given field station is spatially representative of the broader regional ecosystems. The approach produces a transition stage for the MODIS V005 BRDF/Albedo product based on linear weighting functions of the primary/secondary vegetation types that are resolved by the sensor over a given field station. These assessments are just as important as the local analyses presented in previous chapters, since tower albedo measurements are commonly used to scale up to the spatial scales at which regional and global models are commonly utilized. We also assessed the consistency of this method against: (1) coincident ground data measurements at the US Southern Great Plains (SGP) Central Facility (CF); and (2) against daily inversions of broadband (i.e. SWIR 0.3 – 5.0 μm), cloud-free, actual (or blue-sky) albedo retrievals from the MODIS V005 Climate Modeling Grid (CMG) Albedo Product (MCD43C3).

After assessing the spatial representativeness of the SGP-CF, surface albedo fields were reconstructed from ground-truth observations by using: (1) a local upscaling scheme, which uses fine scale retrievals of representative BRDFs over the full extent of the SGP region; and (2) a regional upscaling scheme based on ordinary kriging interpolation of tower albedo measurements. The key sources of uncertainty on the derived surface albedo retrievals across the entire 142,000-square-kilometer SGP domain were identified during the CLASIC intense observation period (IOP) by evaluating the spatial correspondence between daily albedo retrievals at LSN from MODIS and the surface albedo fields reconstructed from the aforementioned schemes. Comparisons between the two upscaling methods (CAR & ordinary kriging) and the MODIS datasets (i.e. 500 m and 0.05°) were also performed to determine which routines have the highest degree of correspondence. The result is a new set of confidence layers for the MODIS BRDF/Albedo product that provide a measure of pixel-specific accuracy at both local

(500 m) and regional modeling scales (0.05°). Furthermore, a cross-comparison between the confidence layers produced by these two independent schemes provides the necessary constraints to evaluate their consistency and validity at these two scales.

4.2. The ARM Southern Great Plains

The development of a complete observations network in the Southern Great Plains (SGP) is the primary focus of the Atmospheric Radiation Measurement Program (ARM). With this goal in mind, an extensive long term field program was initiated in 1989 to obtain the necessary observations of regional exchanges in water, energy, and momentum spanning diurnal, synoptic, seasonal, and interannual time scales (Ackerman and Stokes 2003). Overall, the SGP region spans two states (Oklahoma and Kansas) over a square grid of 375 x 380 km (Figure 4.1). The field stations consist of the Central Facility (as described in Section 3.3.2), where an enormous set of atmospheric properties and radiation data are being collected and an additional array of 19 other measurement sites deployed across the region. The locations of the ground instruments were specifically chosen so that measurements would reflect conditions over the typical distribution of land uses within the SGP region. Table 4.1 provides a description of all of the field stations where tower albedo measurements were acquired during CLASIC. A description of the land surface conditions, both within each measurement site and across the surrounding landscape, is provided as well. For this experiment, coincident observations of daily albedos at LSN were acquired over these stations throughout a 114-day period from 14 June, 2007 to 6 October, 2007.

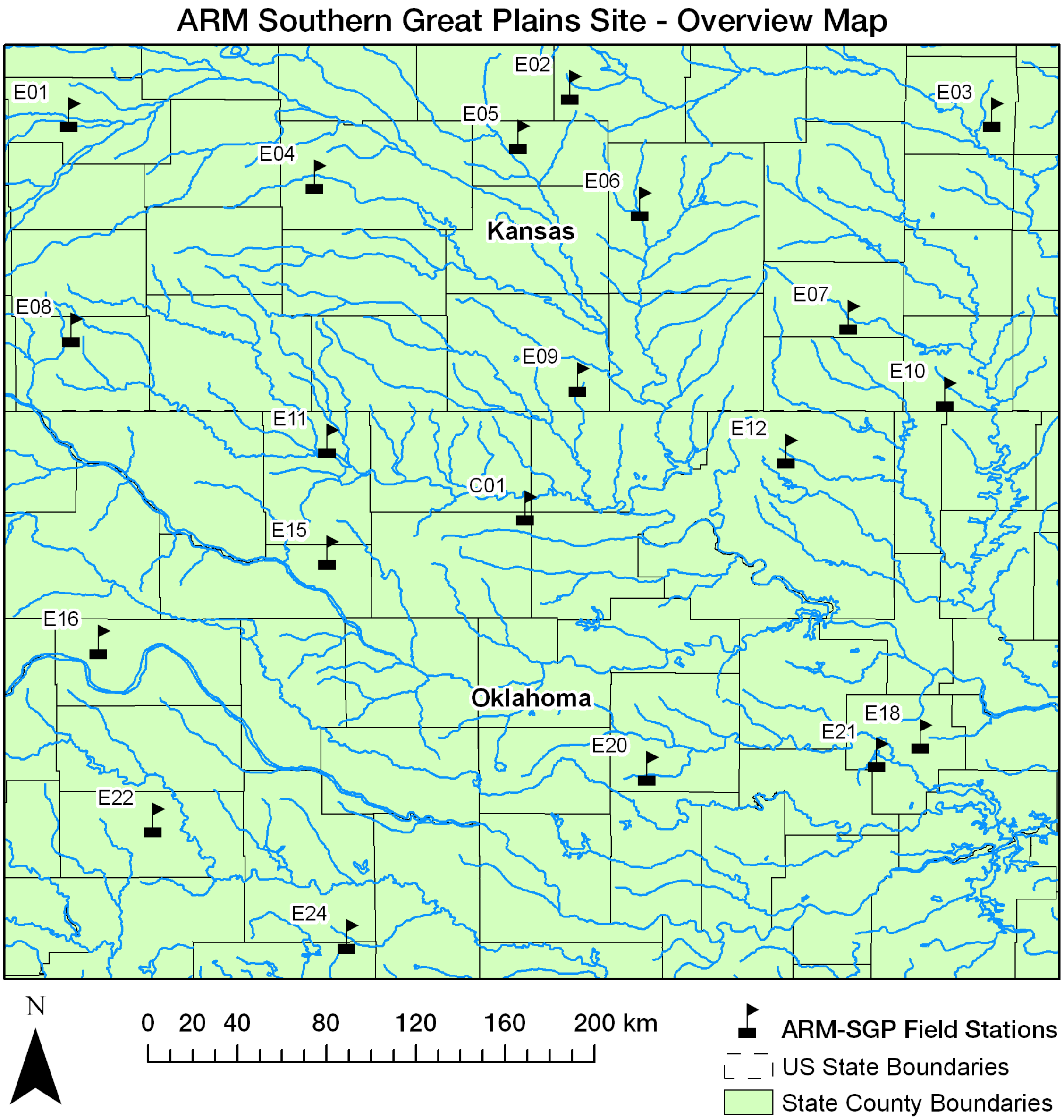

Figure 4.1. The Southern Great Plains (SGP): 20 field stations have been actively collecting surface albedo measurements since the early 1990s. Instrument locations were chosen so that the measurements reflect conditions over the typical distribution of land use/covers.

Table 4.1. Field station coordinates, and their local and regional surface conditions, from surface albedo measurements acquired at the Southern Great Plains during CLASIC.

Field Station	Lat	Lon	Local Surface Conditions	Surrounding Conditions
Lamont, OK (C01)	36.61	-97.49	pasture and winter wheat	winter wheat (N, E, W)
Larned, KS (E01)	38.2	-99.31	pasture and winter wheat	irrigated corn (W)
Hillsboro, KS (E02)	38.31	-97.3	pasture	alfalfa (S) + trees (E, S)
LeRoy, KS (E03)	38.2	-95.6	pasture	winter wheat and soybeans (rotated - S)
Plevna, KS (E04)	37.95	-98.33	rangeland - mowed 1/yr	trees (N, S) + winter wheat (N) + irrigated corn (W)
Halstead, KS (E05)	38.11	-97.51	winter wheat	milo or other tilled irrigated crop (N) + pasture (W)
Towanda, KS (E06)	37.84	-97.02	alfalfa (SE) + grazed pasture (N) + soybean crops (SE)	sorghum (NE) + winter wheat (E)
Elk Falls, KS (E07)	37.38	-96.18	pasture	trees (NW,S)
Coldwater, KS (E08)	37.33	-99.31	rangeland (grazed)	irrigated corn (SW,SE) + winter wheat (N, SE)
Ashton, KS (E09)	37.13	-97.27	pasture	winter wheat (S) + trees (E)
Tyro, KS (E10)	37.07	-95.79	alfalfa or winter wheat + pasture (NW)	trees (E)
Byron, OK (E11)	36.88	-98.28	pasture	trees (W) + alfalfa (NE)
Pawhuska, OK (E12)	36.84	-96.43	tall prairie grazed	trees (N, E)
Ringwood, OK (E15)	36.43	-98.28	pasture	trees (N,W)
Vici, OK (E16)	36.06	-99.13	woody pasture + winter wheat (S)	trees (NW, NE)
Morris, OK (E18)	35.69	-95.86	pasture (clean but ungrazed)	trees (N,S) + winter wheat (S,NE)
Meeker, OK (E20)	35.56	-96.99	pasture + trees (SE)	trees (E,W)
Okmulgee, OK (E21)	35.62	-96.06	forest	forest
Cordell, OK (E22)	35.35	-98.98	rangeland (grazed)	winter wheat (N,E) + urban (NE)
Cyril, OK (E24)	34.88	-98.2	gypsum hill wheat (N,S)	winter wheat (N,S) + urban (NW)
Cement, OK (E26)	34.96	-98.08	pasture	pasture

Tables 4.2 and 4.3 provide the geostatistical rankings, R_{score}, as well as the spatial attributes, R_{CV}, A, R_{SV}, and R_{ST}, for all measurement sites in the SGP. Four of the top-five field stations were ranked as the most spatially representative both during leaf-on and leaf-off conditions. However, only two of the least representative sites (E07-Elk Falls and E21-Okmulgee) were ranked in the bottom five throughout the year. Unlike forested ecosystems, which are consistently stable throughout the year, the rapidly changing surface conditions in the SGP region are very difficult to characterize based on two single "snapshots" obtained throughout a multi-year period. Thus, it is important to characterize both the local and regional variability of these measurement sites based on the conditions observed both before and after this intensive observing period (IOP). Accordingly, surface measurements and detailed land cover surveys were retrieved near several stations throughout the CLASIC-IOP. These sites included various land uses/covers such as winter wheat/stubble (C01), pastures (E11), irrigated crops (E08), and forest canopies (EF21) (Figure 4.2). Four additional CLASIC "super sites" (Figure 4.3) dominated a specific geographic area; e.g. winter-wheat crops in the East and north, forests in the east, irrigated crops in the west, and grasslands in the south and west of the SGP. Additional CLASIC field stations were also selected to include the geographic/land use distribution, considering existing resources. In addition to the large-scale soil moisture measurements conducted throughout the experiment, land cover surveys, vegetation measurements, and surface characterizations were also conducted to develop detailed vegetation water content and land cover imagery. Additional information about the CLASIC-AWiFS land cover dataset can be found in Section 3.3.4.

Table 4.2. Ranking the spatial representativeness of the ARM-SGP measurement sites (during leaf-on conditions) based on the geostatistical attributes R_{CV}, A (or R_{SE}*), R_{SV}, R_{ST}, and the ST_{score}* and RAW_{score}* (*updated: 12/28/2009).

Geostatistical Attributes: Leaf-On Conditions							
Rank	**Field Station**	**R_{CV}**	**R_{SE}**	**R_{SV}**	**R_{ST}**	**STscore**	**RAWscore**
1st	C01	6.49E-02	2.49E-01	4.68E-01	-8.37E-02	2.20E+00	7.71E+00
2nd	E06	8.14E-02	4.82E-01	-1.90E-01	8.61E-02	1.66E+00	6.14E+00
3rd	E18	2.90E-02	5.06E-01	3.54E-01	3.46E-02	1.55E+00	1.72E+01
4th	E08	-2.00E-04	5.71E-01	3.58E-01	-1.95E-02	1.43E+00	2.50E+03
5th	E15	4.88E-02	6.25E-01	-5.66E-02	1.30E-01	1.42E+00	1.02E+01
6th	E20	-1.16E-01	5.74E-01	3.52E-01	-5.47E-02	1.34E+00	4.31E+00
7th	E10	5.17E-02	6.24E-01	2.78E-01	1.30E-01	1.29E+00	9.67E+00
8th	E11	1.18E-01	5.21E-01	7.00E-01	-2.59E-02	1.25E+00	4.25E+00
9th	E22	4.57E-02	6.20E-01	4.91E-01	5.06E-02	1.23E+00	1.09E+01
10th	E04	-5.50E-03	7.21E-01	-1.79E-01	-1.46E-01	1.20E+00	9.09E+01
11th	E24	7.10E-03	6.27E-01	5.48E-01	-8.56E-02	1.19E+00	7.04E+01
12th	E03	-1.42E-01	7.11E-01	9.57E-02	-3.34E-01	1.11E+00	3.53E+00
13th	E09	-1.09E-02	5.65E-01	8.70E-01	1.59E-01	1.10E+00	4.59E+01
14th	E16	-1.30E-01	6.87E-01	-1.96E-01	-3.62E-01	1.09E+00	3.85E+00
15th	E01	-1.07E-01	6.57E-01	6.97E-01	-1.52E-01	1.03E+00	4.66E+00
16th	E07	3.18E-01	5.50E-01	9.37E-01	5.13E-01	8.78E-01	1.57E+00
17th	E05	1.50E-01	7.17E-01	1.22E+00	6.96E-01	7.12E-01	3.32E+00
18th	E12	1.95E-01	7.04E-01	1.15E+00	8.84E-01	6.91E-01	2.56E+00
19th	E02	2.74E-01	7.14E-01	9.52E-01	1.32E+00	6.40E-01	1.83E+00
20th	E21	1.84E+00	5.84E-01	6.91E-01	5.82E+00	2.97E-01	2.72E-01

Table 4.3. Ranking the spatial representativeness of the ARM-SGP measurement sites (during leaf-off conditions) based on the geostatistical attributes R_{CV}, A (or R_{SE}*), R_{SV}, R_{ST}, and the ST_{score}* and RAW_{score}* (*updated: 12/28/2009).

Geostatistical Attributes: Leaf-Off Conditions							
Rank	**Field Station**	**R_{CV}**	**R_{SE}**	**R_{SV}**	**R_{ST}**	**STscore**	**RAWscore**
1st	C01	2.85E-02	1.05E-01	9.55E-02	4.02E-02	6.26E+00	1.76E+01
2nd	E18	-1.13E-01	4.66E-01	-5.64E-02	-1.37E-01	1.76E+00	4.41E+00
3rd	E15	-2.42E-02	5.92E-01	8.44E-02	-3.07E-02	1.57E+00	2.07E+01
4th	E06	-3.20E-02	6.25E-01	-1.89E-02	-2.07E-01	1.41E+00	1.56E+01
5th	E22	8.75E-02	6.96E-01	-7.10E-03	-2.00E-03	1.37E+00	5.71E+00
6th	E12	-4.30E-02	6.79E-01	3.07E-02	-9.95E-02	1.36E+00	1.16E+01
7th	E04	6.40E-03	6.67E-01	-1.89E-01	-1.16E-01	1.30E+00	7.81E+01
8th	E05	-6.20E-03	7.56E-01	3.60E-02	-1.97E-01	1.20E+00	8.06E+01
9th	E24	4.49E-02	7.09E-01	3.23E-01	-1.31E-02	1.20E+00	1.11E+01
10th	E20	8.20E-03	6.88E-01	-3.21E-01	-1.23E-01	1.19E+00	6.10E+01
11th	E16	-1.57E-01	6.69E-01	-1.56E-01	-2.68E-01	1.16E+00	3.19E+00
12th	E02	9.64E-02	5.36E-01	7.14E-01	2.61E-01	1.12E+00	5.19E+00
13th	E09	-1.85E-02	7.77E-01	3.17E-01	-3.35E-02	1.11E+00	2.70E+01
14th	E08	1.73E-02	7.55E-01	3.63E-01	6.36E-02	1.11E+00	2.89E+01
15th	E11	2.96E-01	6.63E-01	4.88E-01	2.61E-01	9.88E-01	1.69E+00
16th	E07	-1.40E-03	7.90E-01	5.43E-01	-1.37E-01	9.84E-01	3.57E+02
17th	E10	4.52E-01	6.63E-01	-2.53E-01	7.76E-01	8.65E-01	1.11E+00
18th	E01	2.77E-02	8.64E-01	1.17E+00	3.23E-01	7.30E-01	1.81E+01
19th	E03	2.07E-01	5.94E-01	2.62E+00	8.79E-01	5.46E-01	2.41E+00
20th	E21	9.65E-01	3.27E-01	1.96E+00	3.86E+00	3.86E-01	5.18E-01

Figure 4.2. Top-Left: Typical conditions of a plowed winter-wheat field near the Central Facility (C01) late June. Top-Right: Grassland conditions during the summer at E24 located near the Little Washita watershed. Bottom Left: Irrigated Crops during CLASIC at Fort Cobb near E22. Bottom-Right: Forest canopy and tower at the Forest Site in Okmulgee, OK (E21).

.

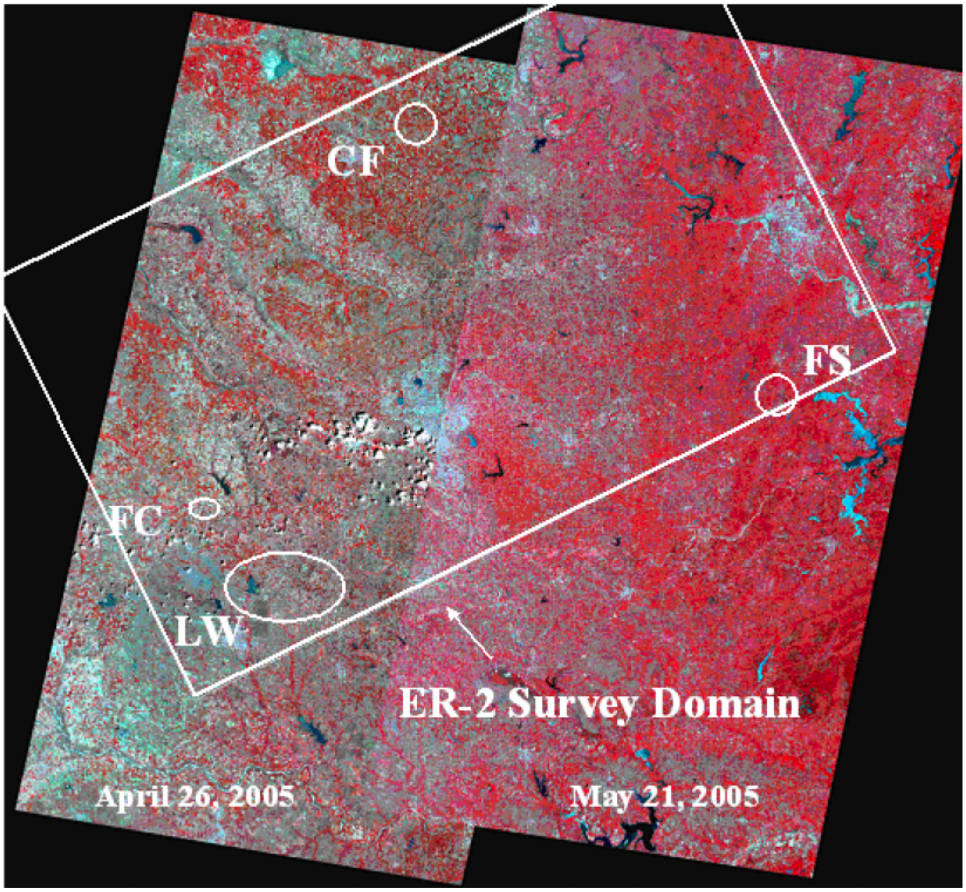

Figure 4.3. Landsat False Color Composite Image of the Oklahoma Portion of the ARM SGP showing the CLASIC super sites. The left portion of the composite was obtained in April and the right in May. Between these dates wheat senesce and grass greens up, assuming adequate moisture with several circular orbits (diameter ≈ 3 km) over each site. Image courtesy of Michael H. Cosh, USDA-ARS-Hydrology and Remote Sensing Laboratory.

4.3. Regional Assessment of Spatial Representativeness

Before proceeding with our two major upscaling schemes, we must first determine whether the in-situ datasets acquired for this study are spatially representative, temporally consistent, and provide a true measure of the regional ecosystems within the SGP region.

Accordingly, we examined the regional representativeness of the SGP Central Facility (SGP-CF), which houses the core instrumentation for the SGP domain and is the center of operations for SGP experiments. This routine uses a combination of ancillary data sources to describe the seasonality and fraction of land cover of the landscapes surrounding a given measurement site to reconstruct a regional signature of surface albedo specific to that site. The methodology for estimating these "transitional albedos" is illustrated in Figure 4.4. Each processing step is described in further detail here:

1. Surface albedo subsets, of size 0.25° x 0.25° and centered on a given measurement site, were extracted from daily inversions of blue-sky albedos at LSN (SWIR 0.3-5.0 μm) from the MODIS (V005) 500 m BRDF/Albedo product.
2. The MODIS (V005) Land Cover 500 m Product (MOD12Q1) (Friedl et al. 2002) was used to separate pixels into tree (or forested) and non-tree (or herbaceous) groups using the PFT classification scheme (Land Cover Type 5) provided in consideration of the Community Land Model (CLM) used in climate modeling. Only pixels classified by the exact same vegetation type(s) observed at the measurement site were selected for each group; pixels classified as shrublands, crops, and grasslands were also selected for the "non-tree" group.
3. The MODIS (V004) Vegetation Continuous Fields 500 m Product (MOD44B) (Hansen et al. 2003) was used to rank the pixels of each tree and non-tree group by percentage cover. The highest ranking pixels of each group, using a 95th percentile as the cut-off point, were then classified into two subgroups of pure-tree and pure-non-tree pixels.

4. Two cloud-free, atmospherically corrected ETM+ scenes acquired at the height of the growing (i.e. leaf-on) and dormancy (leaf-off) seasons were used to calculate the local geostatistical attributes R_{CV}, A, R_{ST}, and R_{SV} for each of the pixel locations belonging to the pure-tree and pure-non-tree subgroups. For each seasonal period, the pixel locations that satisfied the spatial representativeness (defined by ranks of $|R_{CV}| \leq 50\%$, $A \leq 24.3\%$, $|R_{ST}| \leq 50\%$, and $|R_{SV}| \leq 50\%$), were classified into four sub-subgroups: (1) purest-tree pixels during leaf-on period; (2) purest-tree pixels during leaf-off period; (3) purest-non-tree pixels during leaf-on period; and (4) purest-non-tree pixels during leaf-off period.
5. The MODIS (V005) Land Cover Dynamics 500 m Product (MOD12Q2) (Zhang et al. 2006) was used to further specify the daily variation of surface albedo as a function of vegetation phenology. Annual records of the onset of greenness increase (or the first day of green-up) and the onset of greenness minimum (or the first day of dormancy) over each station were used to extract and provide daily averages of the appropriate selection of pixels from the four sub-subgroups.

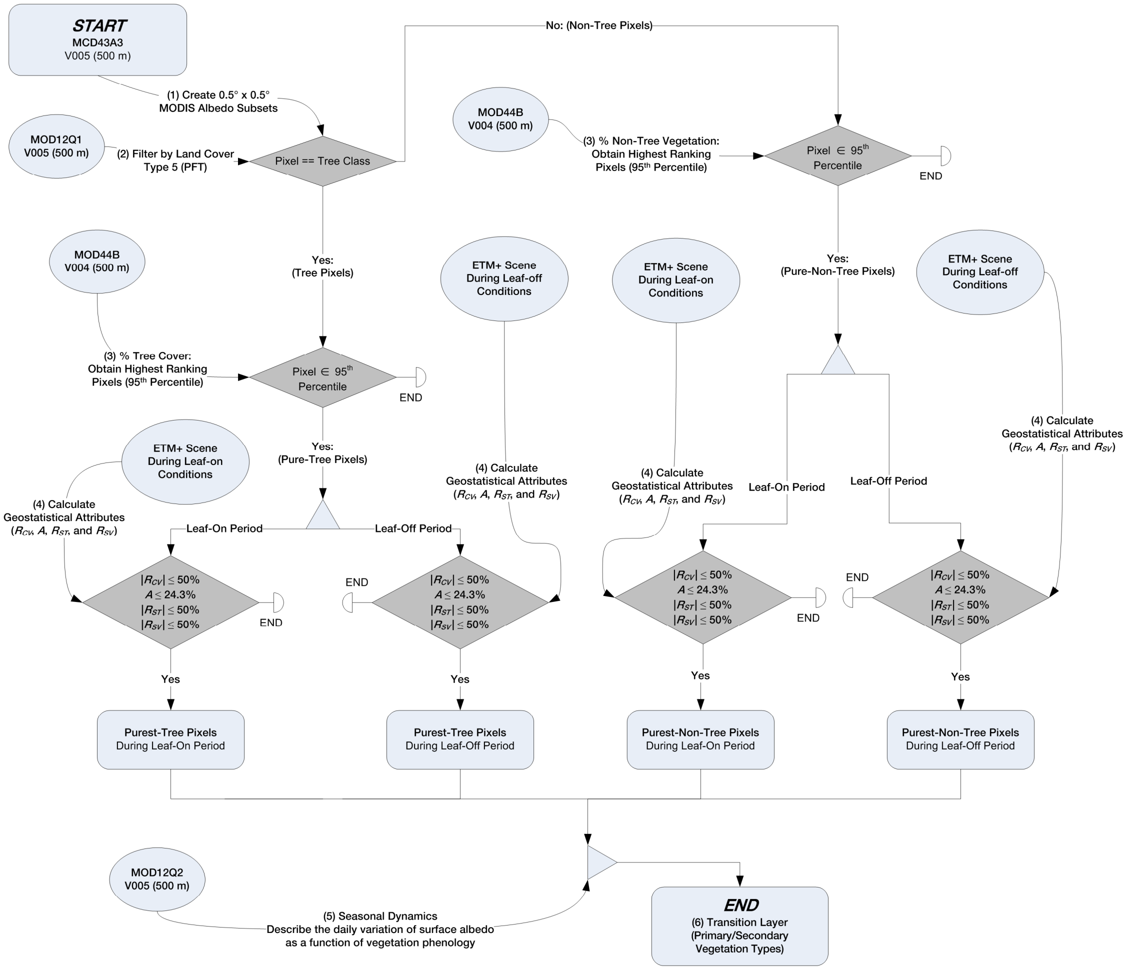

Figure 4.4. Processing and data flow diagram illustrating the creation of a transition stage between the MODIS native (500 m) and climate modeling grid (0.05°) scales, to assess the regional representativeness of measurement sites.

4.3.1. Case Study: ARM-SGP Central Facility

We evaluated the regional representativeness of the SGP-CF by generating a transition stage (as from Figure 4.4) from daily albedos at LSN. Results were then assessed against: (1) coincident ground measurements at the SGP-CF; and (2) daily inversions of broadband (i.e. SWIR 0.3 – 5.0 μm), cloud-free, actual (or blue-sky) albedo retrievals from the MODIS V005 Climate Modeling Grid (CMG) Albedo Product (MCD43C3). Figures 4.6 and 4.7 show results from the two upscaling schemes. These results are also contrasted against a more conventional (or direct) approach, which examines MODIS albedo retrievals at the native (500 m) spatial resolution directly against tower albedo measurements.

The blue circles and red triangles, on the time series plots (Figure 4.5), indicate snow-free blue-sky albedo retrievals at LSN derived from MCD43A3 using the main (full-inversion) and backup algorithms, respectively. The red asterisks, indicate snow-covered retrievals, as indicated by the snow flag in the MODIS V005 albedo product embedded QA (MCD43A2), using the backup algorithm. The series of scatter plots, in Figure 4.6, evaluate the daily blue-sky albedos from MCD43A3 against field measurements using four seasons: January-February-March (JFM) in blue, April-May-June (AMJ) in green, July-August-September (JAS) in red, and October-November-December (OND) in yellow. MODIS data from full inversion retrievals (in open shapes) were also separated from the "Full + Magnitude" inversion cases (in asterisks) to investigate the inversion quality differences when both methods are applied. The solid line is the one-to-one line and the dashed lines are ±0.02 and ±0.05 units. The statistical results for the absolute error (i.e. Groundmean – MODISmean) and RMSE values calculated for the entire multi-year retrieval period are also displayed for each scenario (i.e. Full / Full+Magnitude).

The first comparison (i.e. between transitional albedos compared against tower measurements) provides an estimate of the degree to which a measurement site can be treated as a representative sample of its regional landscape. The second comparison (i.e. transitional albedos compared against the MODIS CMG product) can then be used to quantify the ability of the MODIS CMG data to capture the spatial and seasonal signatures specific to the SGP-CF. Results appear to be consistent across scales (both local and regional). Daily albedos were particularly stable throughout the summer season, which is of interest to our study objectives. On average, 77% of the daily 500 m MODIS retrievals in 2006 were within ±0.05 units (absolute RMSE) of the ground measured seasonal average albedos, while 98% of the daily CMG retrievals were within ±0.05 units.

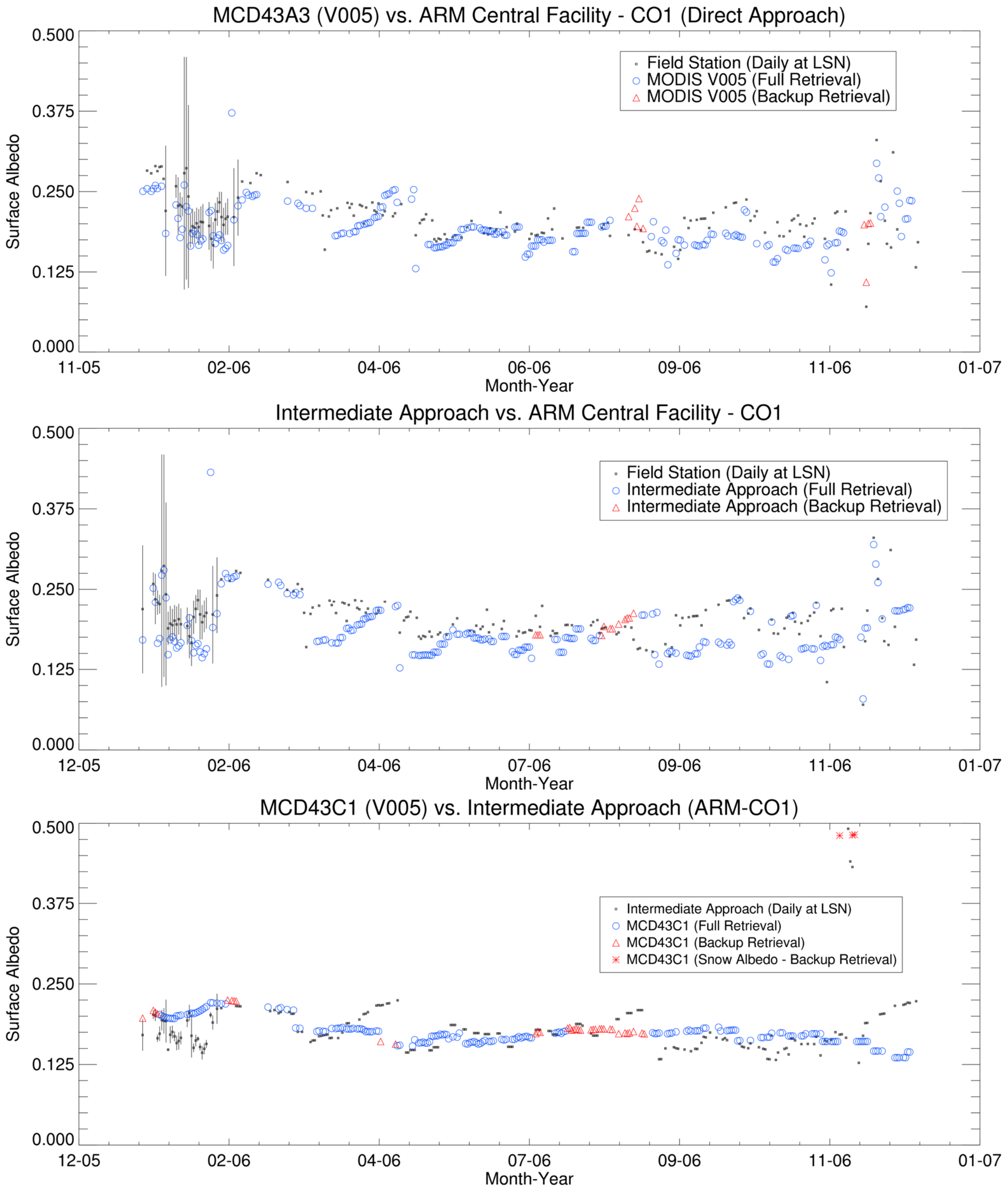

Figure 4.5. Time series of surface albedos at LSN for the ARM-SGP Central Facility in 2006. The three plots show (from top to bottom): (1) comparisons between MCD43A3 and tower measurements; (2) comparisons between the transition stage and tower measurements; and (3) the transition stage vs. MCD43C1. Dark points with error bars are daily retrievals of surface albedo. Blue circles and red triangles indicate snow-free blue-sky albedo retrievals at LSN derived from MCD43A3 using the main (full-inversion) and backup algorithms, respectively. Red asterisk indicate snow-covered retrievals.

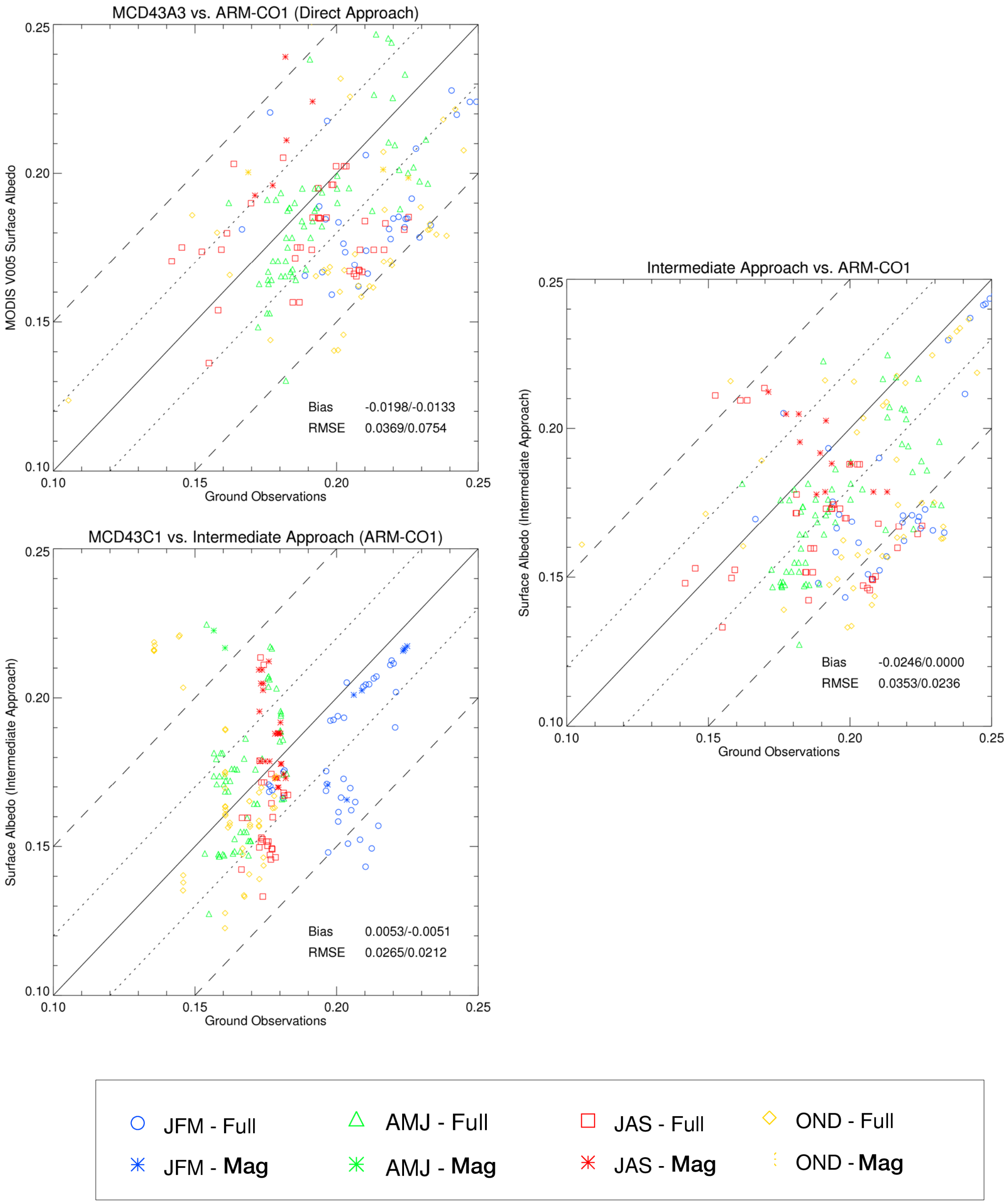

Figure 4.6. Three scatter plots evaluate the blue-sky albedos retrievals (daily at LSN) following the time series comparison as from Figure 4.5. The daily albedos were divided into four seasonal classes: JFM in blue, AMJ in green, JAS in red, and OND in yellow. The solid line is the one-to-one line and the dashed lines are ±0.02 and ±0.05 units. MODIS data from full inversion retrievals (in open shapes) were also separated from the "Full + Magnitude" inversion cases (in asterisks). The statistical results for the absolute bias and RMSE values are also displayed for each scenario (i.e. Full / Full+Magnitude).

4.4. Spatial Upscaling Schemes

4.4.1. Local Upscaling Method

Daily surface albedo fields at LSN were reconstructed from 50 m BRDF retrievals of archetypal landscapes as derived by the Cloud Absorption Radiometer (CAR) at the Central Facility during the CLASIC intense observing period (IOP) (i.e. 18 June, 2007 to 4 July, 2007) (see Figure 3.5). These BRDFs were spatially driven by fine-scale areal fractions based on 50 m land cover fields extracted from the CLASIC-AWiFS land cover dataset across the full spatial extent of the SGP region (Figure 4.7).

Table 4.4 provides results for the RTLSR BRDF model parameters of the most common surface covers found in SGP; and Figure 4.8 shows their respective polar plots. These results were acquired by transforming and scaling the CAR retrievals into 50 m spatial grids and capturing the underlying response over areas representing each of these surface conditions. Looking at the polar plots on Figure 4.8, the hot-spot region appears to be a common feature observed over all land cover classes, particularly for the pasture and wheat classes. The forest and corn classes exhibit a consistent decrease in bi-directional reflectance at increased view angles over the forward-scattering region. Overall, each dominant class has a unique BRDF response, which makes them suitable for our local analyses of albedos over the entire SGP domain.

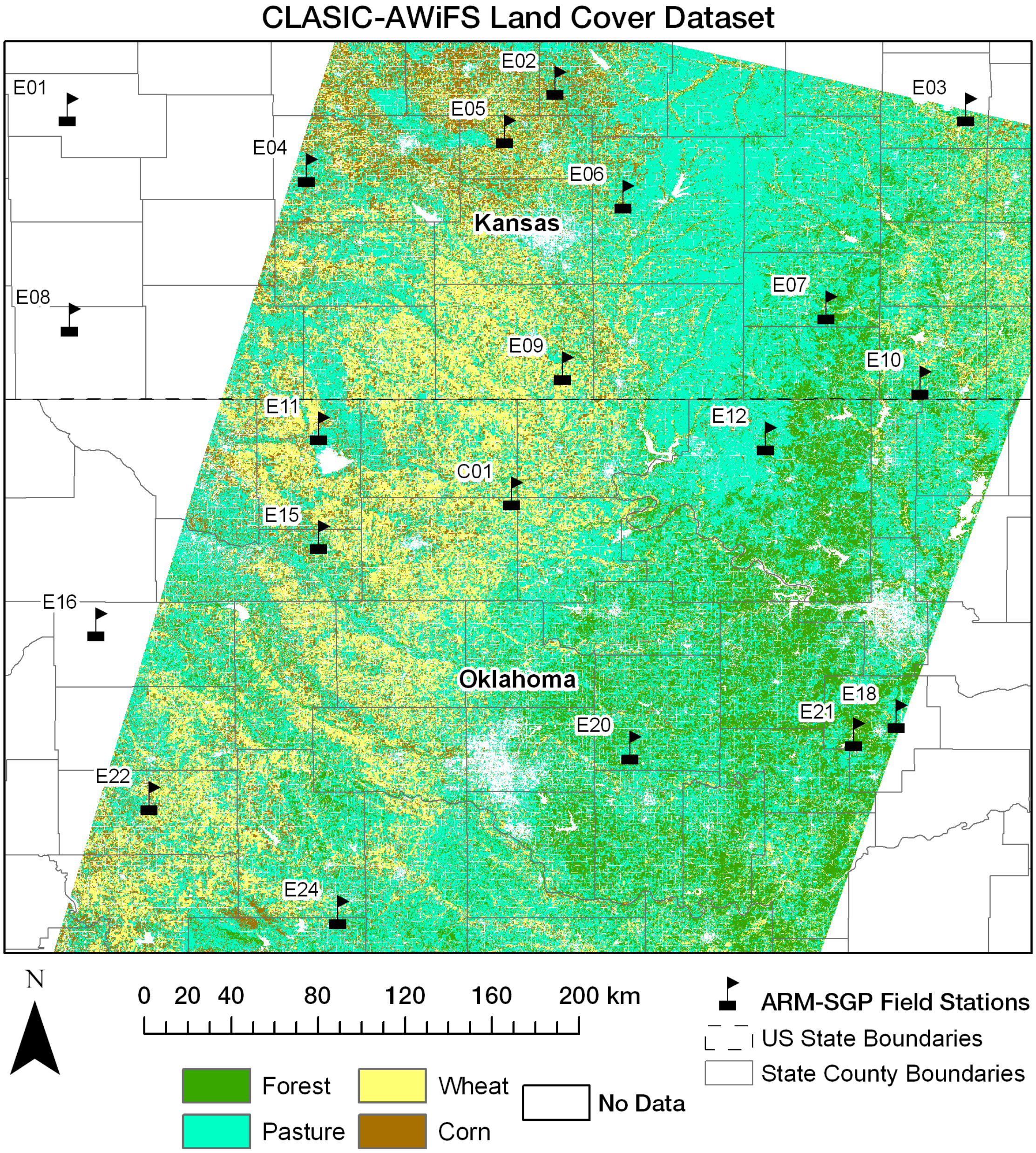

Figure 4.7. The CLASIC-AWiFS 56 m land cover dataset was screened to identify the most representative surface conditions in the SGP region during the CLASIC IOP.

Table 4.4. RTLSR BRDF model parameters of the most representative surface conditions in the SGP region during the CLASIC IOP (i.e. 18 June, 2007 to 4 July, 2007).

	RTLSR BRDF Model Parameters (0.3 - 5.0 μm)		
Land Cover	**$F_{iso}(\Lambda)$**	**$F_{vol}(\Lambda)$**	**$F_{geo}(\Lambda)$**
Forest	0.1651	0.0619	0.0170
Pasture	0.1929	0.0778	0.0127
Wheat	0.2109	0.0607	0.0145
Corn	0.1773	0.0471	0.0180

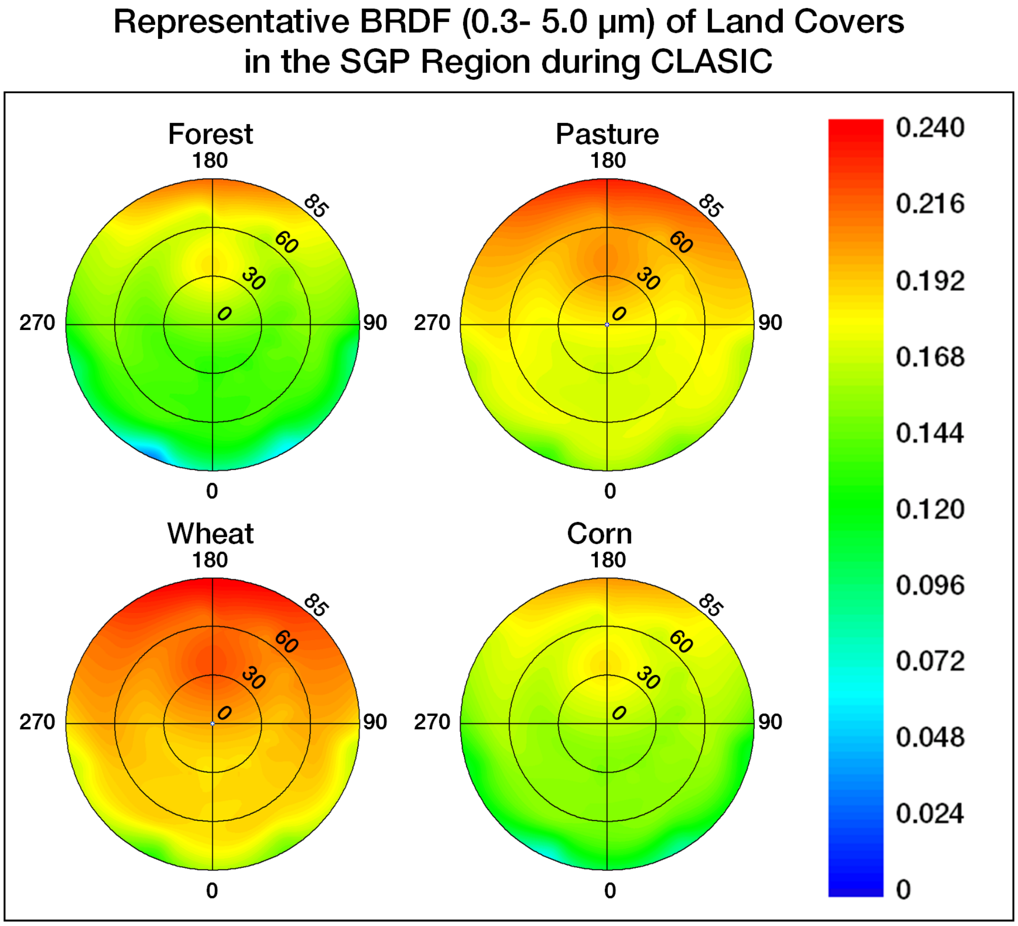
Representative BRDF (0.3- 5.0 μm) of Land Covers in the SGP Region during CLASIC

Figure 4.8. Broadband BRDFs (0.3 – 5.0 μm, with solar zenith angle, θ_s = 30°) derived from CAR retrievals, using 50 m areal-mean estimates of the most representative surface conditions in the SGP region during the CLASIC IOP (see Figure 3.5).

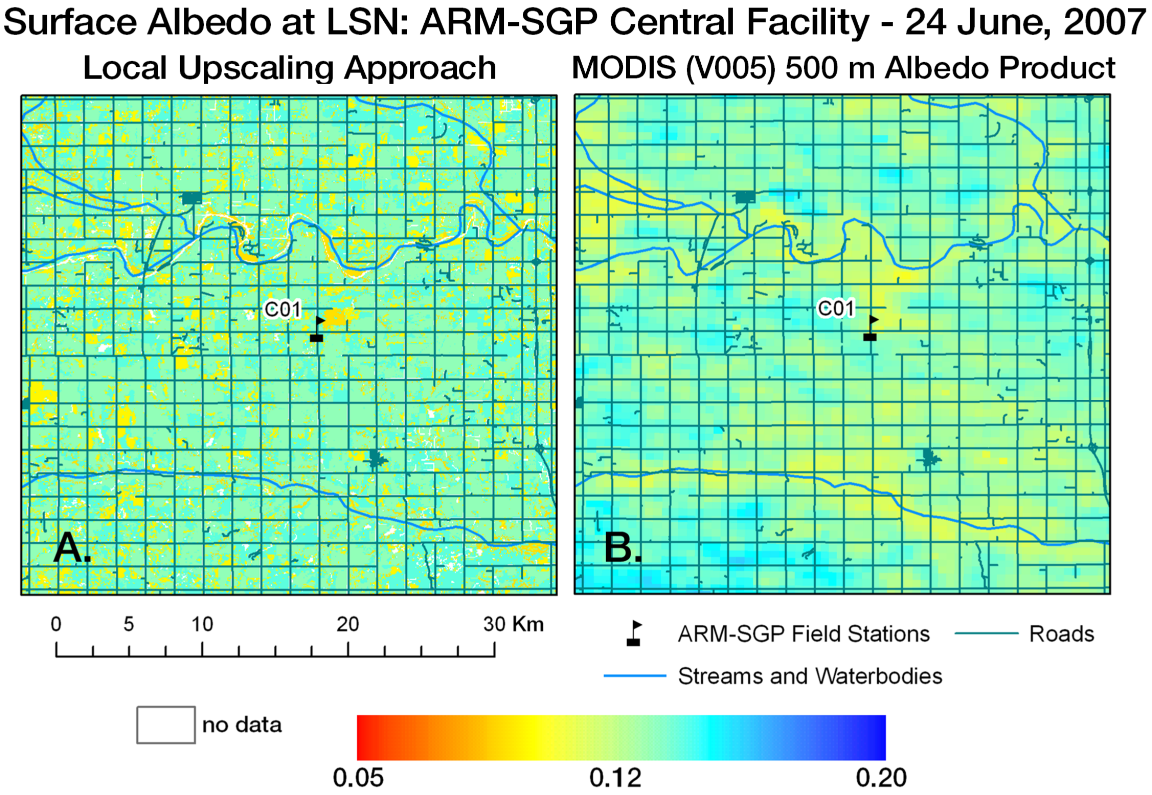

Figure 4.9. Surface albedo fields over the SGP-CF region reconstructed from (A) 50 m BRDF retrievals of archetypal landscapes as derived from the CAR; and (B) MCD43A3 (V005) 500 m retrievals.

Figure 4.9 shows actual (or blue-sky) albedo fields (SWIR 0.3 – 5.0 µm) reconstructed from (A) 50 m BRDF retrievals of archetypal landscapes as derived from the CAR; and (B) MODIS MCD43A3 (V005) 500 m albedo retrievals. Both maps show actual albedo conditions at LSN over the SGP-CF region during 24 June, 2007; i.e., the same day of CLASIC Flight #1928. While the albedos as seen from the 50 m fields appear to be confined to smaller clumps (or patches), the MODIS 500 m retrievals consistently followed their spatial variations all across the SGP-CF region. A notable difference, however, can be seen in the vicinity of both the Salt Fork Arkansas River (~5 km north of the SGP-CF) and the Red Rock Creek (~11 km south of the SGP-CF). Over these areas, the MODIS albedos were consistently lower by 0.025-0.040 units. Since a water class was not included when extracting the 50 m albedo fields, the fine-scale retrievals were not as influenced by conditions of increased wetness at the surface. Conversely, MODIS retrievals located nearby streams and water bodies are mixing up the areal albedo signal over such landscapes, thus producing consistently lower albedos (seen in orange and yellow).

4.4.2. Regional Upscaling Method

Daily surface albedo fields at LSN were also reconstructed from ordinary kriging interpolations of ground albedo measurements. Concurrent observations of surface albedos at LSN were acquired from 20 towers located across the SGP region (see Table 4.1). The basic technique of ordinary kriging is an optimal and unbiased linear technique for estimation. In this sense, it provides the ‘best’ possible estimates of unknown values from sample data. The estimate is obtained by weighting each of several sample data that are adjacent to the tower albedo measurements (*A*):

$$A_{x0} = \sum_{i}^{N} w_i \cdot A_{xi}\,, \tag{4.1}$$

where λ_i are the weights which have to be estimated. Given spatial dependence, closer data to a given field station will receive more weight because they are more likely to be similar to the unknown value. The exact weights are then determined from the exact form of spatial dependence as represented by a spherical variogram. The unbiasedness is ensured by normalizing the weights to one. Note that the expected error of the estimation has to be zero:

$$E\left(\hat{A}_{x0} - A_{x0}\right) = 0, \tag{4.2}$$

where A_{x0} is the true, but unknown value. Using the previous equation, we can compute the mean-squared error in terms of a spherical variogram model:

$$E\left(\left(\hat{A}_{x0} - A_{x0}\right)^2\right) = 2\sum_{i=1}^{N} w_i \cdot \gamma_{sph}(x_i, x_0) - \sum_{j=1}^{N}\sum_{j=1}^{N} w_i w_j \cdot \gamma_{sph}(x_i, x_j), \tag{4.3}$$

where E is the estimation of the kriging variance, which has to be minimized, $\gamma_{sph}(x_i,x_0)$ is the variogram (semivariance) between the data point and the unobserved, $\gamma_{sph}(x_i,x_j)$ is the variogram between the data points x_i and x_j, and w_i and w_j are the weights of the i and j data point (Cressie 1993). For ordinary kriging, we have to minimize equation 4.3, by satisfying the linear constrain that the sum of weights should be one.

Throughout this section, we use ordinary kriging to interpolate surface albedo fields continuously over space and time, based on point samples obtained from tower measurements across the SGP region. Thus, it is important to have a good understanding of the spatial and temporal properties of these in-situ measurements in order to best model the data. As such, a number of exploratory spatial data analysis routines (Haining and Wise 1997) were performed. By understanding the spatial and temporal characteristics of the in-situ data, the better kriging model one can build to interpolate the data, and, consequently, the better estimates, and thus the confidence, of surface albedo that one will produce. In particular, we are interested in understanding the population distribution of the collective number of daily observations obtained across the SGP region. Accordingly, Figure 4.10 shows a histogram plot showing daily surface albedos at LSN from all 22 measurement stations in the SGP region collected throughout a 114-day period during the summer of 2007 (14 June, 2007 – 6 October, 2007). When combined, the ground albedo dataset follows a normal distribution, which is desired, since kriging assumes that the input point data are multivariate normally distributed. Another way to understand the data's distribution is by examining normal Quantile-Quantile (QQ) plots. In a QQ plot we test whether data are normally distributed by plotting it against a dataset with a known normal distribution. If the plot is linear along the line Y=X, then the data follow a normal distribution. Accordingly, the QQ plots on Figure 4.11 reveal the presence of a linear relationship between the distribution of kriged estimates of surface albedo and the standard normal distribution of tower measurements for three separate days throughout the retrieval period.

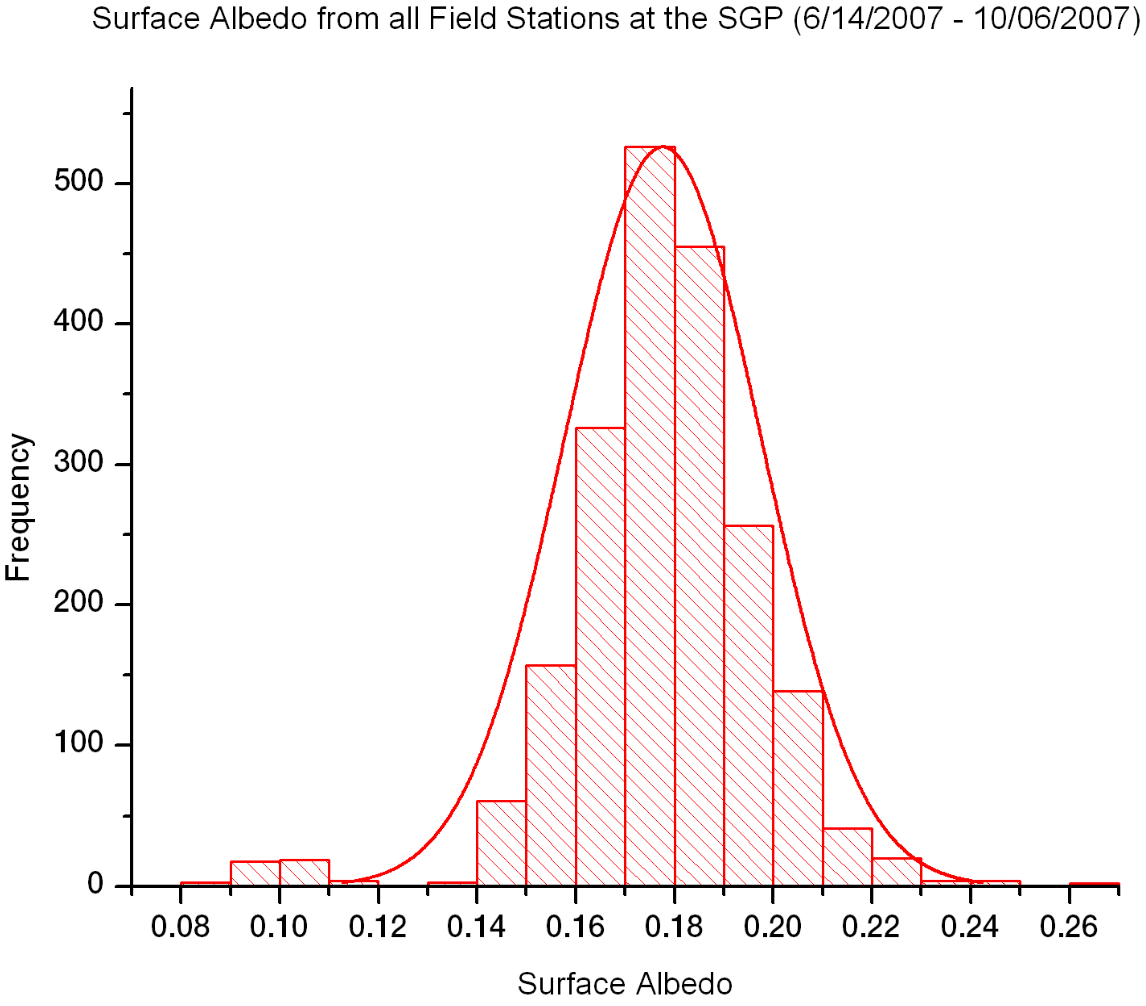

Figure 4.10. Histogram plot showing surface albedos from all 20 measurements sites in the SGP region collected throughout a 114-day period during the summer of 2007 (14 June, 2007 – 6 October, 2007).

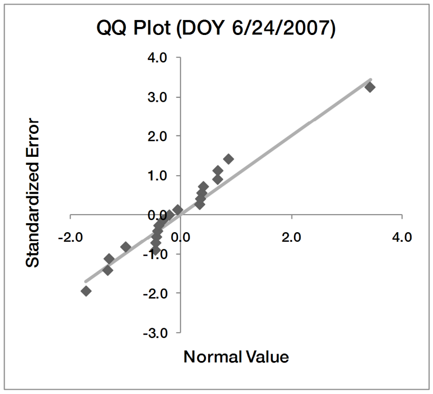

Mean: 0.0003103
Root-Mean-Square: 0.02158
Average Standard Error: 0.02037
Mean Standardized: 0.01449
Root-Mean-Square Standardized: 1.051

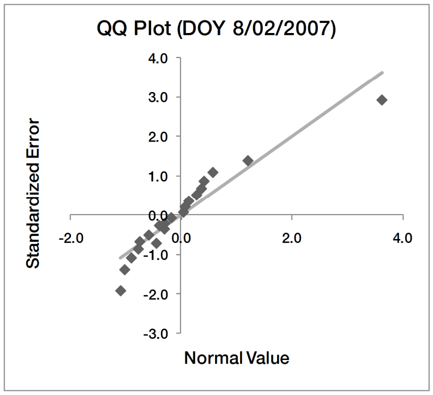

Mean: 0.001105
Root-Mean-Square: 0.02251
Average Standard Error: 0.02157
Mean Standardized: 0.04903
Root-Mean-Square Standardized: 1.039

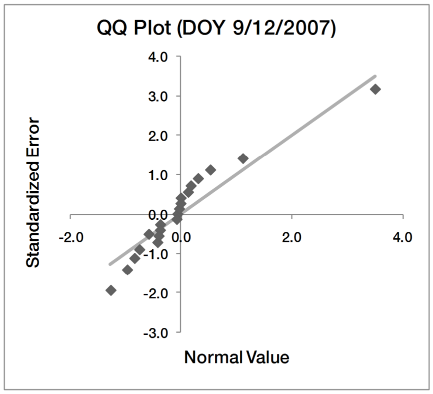

Mean: -0.0001475
Root-Mean-Square: 0.02116
Average Standard Error: 0.02275
Mean Standardized: -0.007199
Root-Mean-Square Standardized: 0.926

Figure 4.11. Normal Quantile-Quantile (QQ) plots show the relationship between the distributions of kriged estimates of surface albedo fields and the standard normal distribution of tower measurements for three separate days during the CLASIC IOP. Additional error statistics were calculated for each case through cross-validation between point measurements and kriged retrievals.

Figure 4.11 provides additional statistics calculated through cross-validation for each of the daily results. These statistics give a measure of uncertainty an indication of the goodness of fit in the kriging predictions. If the prediction errors are unbiased, then the mean prediction errors should be near zero. However, this value depends on the scale of the data, so the mean standardized prediction error gives the prediction errors divided by their prediction standard errors. This value should also be as close to zero as possible. The root-mean-squared prediction error indicates how closely the kriging model predicts the measured values; thus, the smaller the root-mean-squared prediction errors the better.

Since it is crucial to obtain the correct variability in albedo, we estimated the variability of the predictions from the measured values. In ordinary kriging (assuming the residuals are normally distributed) the quantile and probability fields depend on the kriging standard errors as much as the predictions themselves. If the average standard error is close to the root-mean-squared prediction error, then we are correctly assessing the variability in prediction. If the average standard error is less (or greater) than the root-mean-squared prediction error, then we are underestimating (or overestimating) the variability of our predictions. Another way to look at this is to divide each prediction error by its estimated prediction standard error. They should be similar, on average, and so the root-mean-squared standardized error should be close to one if the prediction standard errors are valid. If the root-mean-squared standardized error is greater than one, we are underestimating the variability in our predictions. If the root-mean-squared standardized error is less than one, then we are overestimating the variability in our predictions. The important point to take away from these analyses is that within the bounds of the detection limits, surface albedo fields reconstructed using ordinary kriging methods have predictions errors that are unbiased, consistently predict the measured (or point) values, and are correctly assessing the variability in albedo throughout the SGP region.

Figure 4.12 shows the resulting blue-sky albedo fields (SWIR 0.3 – 5.0 μm) reconstructed from (top) ordinary kriging interpolations of ground albedo measurements; and (bottom) MODIS CMG (MCD43C3 0.05°) albedo retrievals, for three separate days. At the center, three examples of the searching neighborhood method and geometry sectors utilized by the kriging method are shown. Note that the spatial patterns reproduced by the ordinary kriging results depend on both the number and geometry sector in the moving window. The points highlighted in the data view give an indication of the weights associated with each point in the moving window. The weights are then used to estimate the value of the unknown location (i.e. the center of each cross-hair). These results were driven by a spherical variogram model with a minimum lag distance of ~ 0.2°. This was the smallest separation distance that could be specified that would also yield enough pairs of tower measurements in each lag to generate a statistically significant set of kriging weights. Thus, the regional upscaling results are coarser but otherwise consistent with the regional spatial patterns of albedo as seen from the MODIS CMG data. The magnitudes of the albedos between the two datasets agree well, with consistently higher albedos in the northern grasslands and western croplands of the SGP, and lower albedos in the forested regions in the southeast.

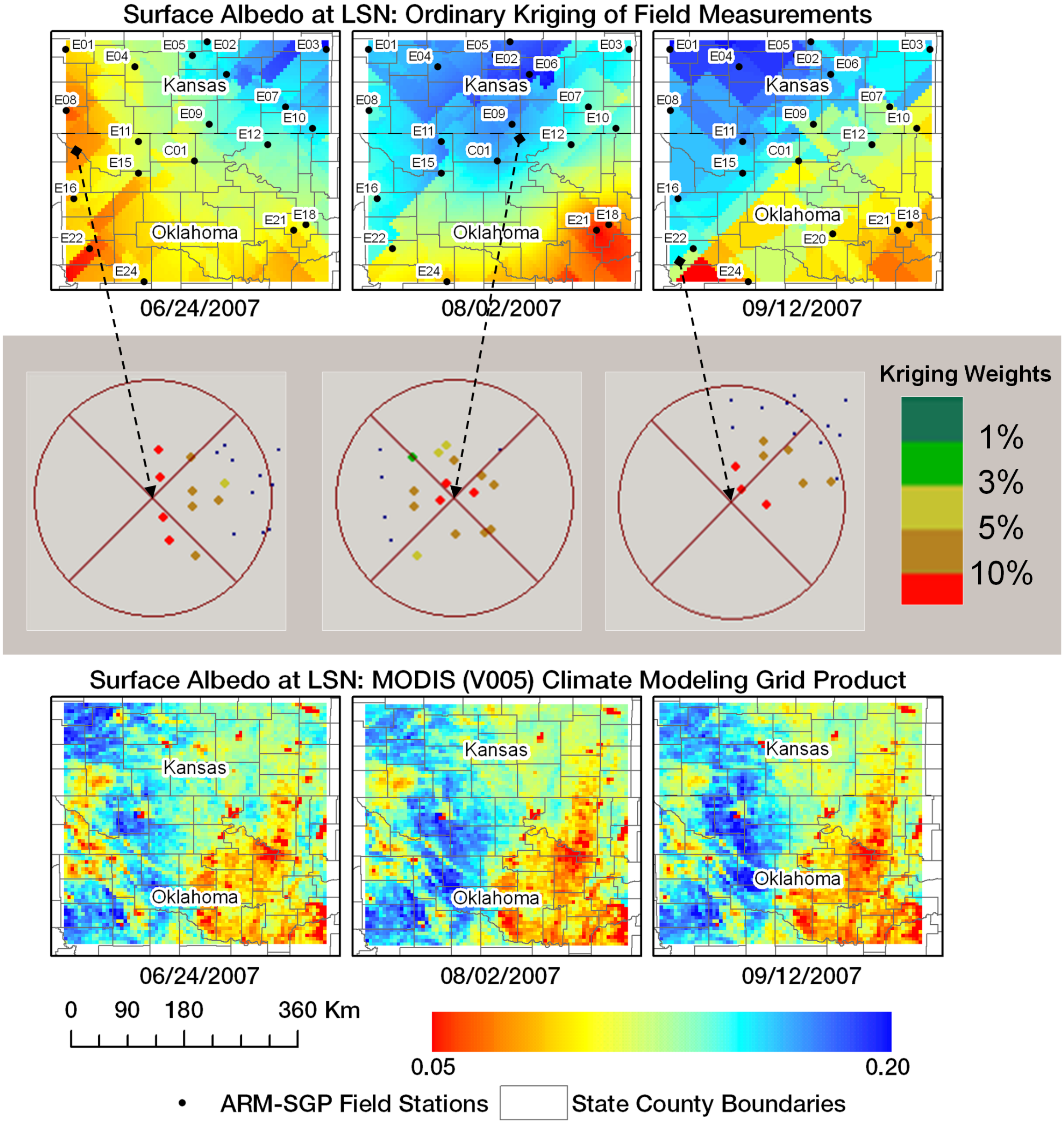

Figure 4.12. Surface albedo fields over the SGP-CF region reconstructed from ordinary kriging interpolations of ground albedo measurements (i.e. regional upscaling approach); and (bottom) MCD43C3 0.05° retrievals, for three separate days. The center figure shows examples of the searching neighborhood method and geometry sectors utilized to generate the regional upscaling data.

4.5. Results and Discussion

Table 4.5 provides a comparison between the local and regional upscaling methods and the MODIS albedo products at 500 m and 0.05°. These datasets were reconstructed using daily surfaces albedos at LSN for a 16-day segment of the CLASIC-IOP (06/18/2007 - 07/03/2007). Each comparison was partitioned by land cover class for each scenario (i.e. forest, pasture, wheat, and corn) and the final results were ranked by their highest-to-lowest degree of correspondence between upscaling methods (i.e. RMSE, mean absolute error, and mean relative error). As expected, the daily comparisons between the MODIS 500 m and MODIS CMG products corresponded closely for all land cover classes, with errors consistently below 0.0075 units of absolute RMSE. Because the MODIS albedo products are ultimately generated using the same input data, these errors can be directly attributed to spatial scaling effects. Thus, any additional errors identified between the MODIS datasets and the local and regional upscaling methods can be attributed to differences in the measurement methodology between the different upscaling schemes.

Both the local and regional upscaling methods followed the MODIS datasets across all land cover classes, with errors consistently under 0.03 units of absolute RMSE. However, results for the local upscaling method were much more accurate than the regional method by 0.008 absolute RMSE or 4.75% relative error. Because the local upscaling layer was driven by finer-scale (50 m) retrievals of archetypal landscapes, these comparisons are more representative of the underlying surface conditions in the SGP region. Conversely, the regional upscaling approach, which was produced at a much lower spatial resolutions (~ 0.2°), consistently underestimated the MODIS albedo retrievals by -0.019 absolute error. These biases can be attributed to spatial mixing between land cover classes, which are very difficult to capture at these large scales.

Albeit a less accurate approach, the regional upscaling method has a wider temporal range that spans beyond a typical 16-day retrieval period of the local upscaling layer. However, these comparisons were constrained by the availability of coincident retrievals between the local and regional upscaling layers. Accordingly, Figures 4.13 to 4.15 provide a series of local uncertainty maps showing the absolute RMSE field values between blue-sky albedo retrievals at LSN from MODIS (MC43A3) and the local upscaling approach. The sample size consists of daily albedo retrievals acquired throughout the same 16-day segment (06/18/2007 - 07/03/2007) of the CLASIC-IOP. Figure 4.16 also provides a confidence map using the regional upscaling method against the MODIS CMG albedo product (MDC43C3), but using a larger sampling period that consists of 114-daily albedo retrievals acquired during the entire CLASIC-IOP (14 June, 2007 to 6 October, 2007).

Table 4.5. Comparing the spatial upscaling routines against each other and against the MODIS 500 m and CMG (0.05°) albedo products throughout a 16-day segment (06/18/2007 - 07/03/2007) of the CLASIC-IOP.

	Land Cover Type - Forest (n = 663)	**Absolute Error**		**Relative Error**		**Absolute RMSE**	
Rank	**Upscaling Method**	**Mean**	**Stdev**	**Mean**	**Stdev**	**Mean**	**Stdev**
1st	MODIS (500 m) vs. MODIS (CMG)	0.0024	0.0105	5.04%	6.59%	0.0075	0.0083
2nd	CAR (Local) vs. MODIS (CMG)	-0.0057	0.0094	5.09%	4.79%	0.0084	0.0077
3rd	CAR (Local) vs. MODIS (500 m)	-0.0081	0.0107	6.31%	5.73%	0.0103	0.0093
4th	CAR (Local) vs. Kriging (Regional)	0.0189	0.0067	12.02%	4.21%	0.0213	0.0062
5th	Kriging (Regional) vs. MODIS (CMG)	-0.0246	0.0103	13.80%	5.40%	0.0272	0.0097
6th	Kriging (Regional) vs. MODIS (500 m)	-0.0270	0.0114	15.16%	6.02%	0.0293	0.0109

	Land Cover Type - Pasture (n = 1833)	**Absolute Error**		**Relative Error**		**Absolute RMSE**	
Rank	**Upscaling Method**	**Mean**	**Stdev**	**Mean**	**Stdev**	**Mean**	**Stdev**
1st	MODIS (500 m) vs. MODIS (CMG)	-0.0017	0.0087	3.84%	4.07%	0.0065	0.0066
2nd	CAR (Local) vs. Kriging (Regional)	0.0023	0.0068	4.81%	1.49%	0.0103	0.0027
3rd	CAR (Local) vs. MODIS (500 m)	-0.0182	0.0083	10.35%	4.54%	0.0190	0.0083
4th	CAR (Local) vs. MODIS (CMG)	-0.0200	0.0089	11.29%	5.00%	0.0207	0.0091
5th	Kriging (Regional) vs. MODIS (500 m)	-0.0205	0.0101	11.59%	4.67%	0.0233	0.0086
6th	Kriging (Regional) vs. MODIS (CMG)	-0.0223	0.0106	12.45%	5.17%	0.0250	0.0095

	Land Cover Type - Wheat (n = 726)	**Absolute Error**		**Relative Error**		**Absolute RMSE**	
Rank	**Upscaling Method**	**Mean**	**Stdev**	**Mean**	**Stdev**	**Mean**	**Stdev**
1st	MODIS (500 m) vs. MODIS (CMG)	-0.0026	0.0086	3.69%	3.96%	0.0066	0.0068
2nd	CAR (Local) vs. Kriging (Regional)	0.0041	0.0055	4.86%	1.39%	0.0103	0.0024
3rd	CAR (Local) vs. MODIS (500 m)	-0.0089	0.0081	5.84%	3.74%	0.0105	0.0067
4th	CAR (Local) vs. MODIS (CMG)	-0.0115	0.0084	6.88%	4.42%	0.0125	0.0079
5th	Kriging (Regional) vs. MODIS (500 m)	-0.0130	0.0109	8.55%	4.11%	0.0176	0.0076
6th	Kriging (Regional) vs. MODIS (CMG)	-0.0156	0.0107	9.44%	4.72%	0.0195	0.0086

	Land Cover Type - Corn (n = 493)	**Absolute Error**		**Relative Error**		**Absolute RMSE**	
Rank	**Upscaling Method**	**Mean**	**Stdev**	**Mean**	**Stdev**	**Mean**	**Stdev**
1st	CAR (Local) vs. MODIS (CMG)	0.0023	0.0084	4.02%	3.68%	0.0068	0.0060
2nd	MODIS (500 m) vs. MODIS (CMG)	-0.0021	0.0093	4.28%	4.48%	0.0073	0.0068
3rd	CAR (Local) vs. MODIS (500 m)	0.0044	0.0099	5.35%	4.22%	0.0088	0.0069
4th	Kriging (Regional) vs. MODIS (500 m)	-0.0152	0.0125	9.60%	5.16%	0.0195	0.0095
5th	Kriging (Regional) vs. MODIS (CMG)	-0.0174	0.0107	10.20%	4.84%	0.0209	0.0088
6th	CAR (Local) vs. Kriging (Regional)	0.0197	0.0060	12.39%	3.72%	0.0219	0.0055

Results show that the MODIS retrievals are consistently within 0.02-0.05 units of absolute RMSE. For the local confidence layer, 82% of the MODIS 500 m pixels in the SGP region were within 0.02 units of absolute RMSE and 95% of the MODIS pixels were within 0.05 units. Similarly, for the regional confidence layer, 80% of the MODIS CMG pixels were within 0.02 units of absolute RMSE and 96% were within 0.05 units. A comparison between confidence layers also shows consistent agreement; particularly over areas where the uncertainties between datasets are greater than 0.05 units. MODIS retrievals located nearby streams and water bodies consistently underestimated the areal albedo signal with respect to both the local and regional upscaling schemes. A closer look at the local confidence layer across the Little Washita Watershed (Figure 4.14) also shows additional uncertainties across neighboring landscapes surrounding the watersheds of various local rivers.

The CLASIC-IOP experienced anomalous rainfall conditions, which resulted in widespread and repeated flooding throughout the state of Oklahoma and Texas. In particular, the Little Washita (E24) and Forest Site (E21) regions experienced > 8 inches of rainfall (see Figure 4.17). Thus, it is likely that the uncertainties in the confidence layers over these regions are caused by the inability of the upscaling methods, which are driven by maps based on data prior to the rainy period or the widely scattered towers, to capture such anomalous rainfall conditions.

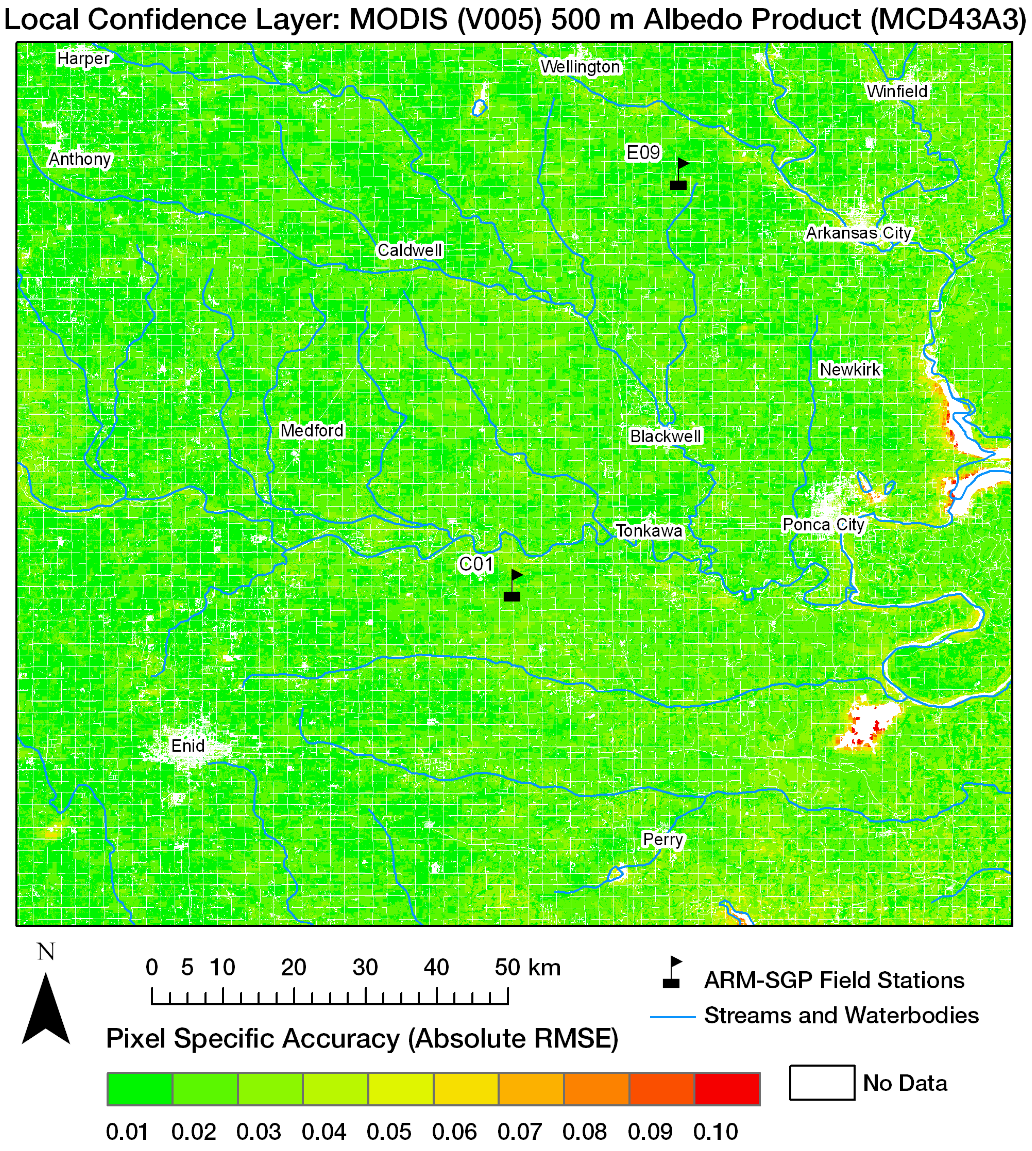

Figure 4.13. Local uncertainty map of the SGP-Central Facility (and vicinity) showing the absolute RMSE field values between blue-sky albedo retrievals at LSN from MC43A3 and the local (50 m) upscaling approach.

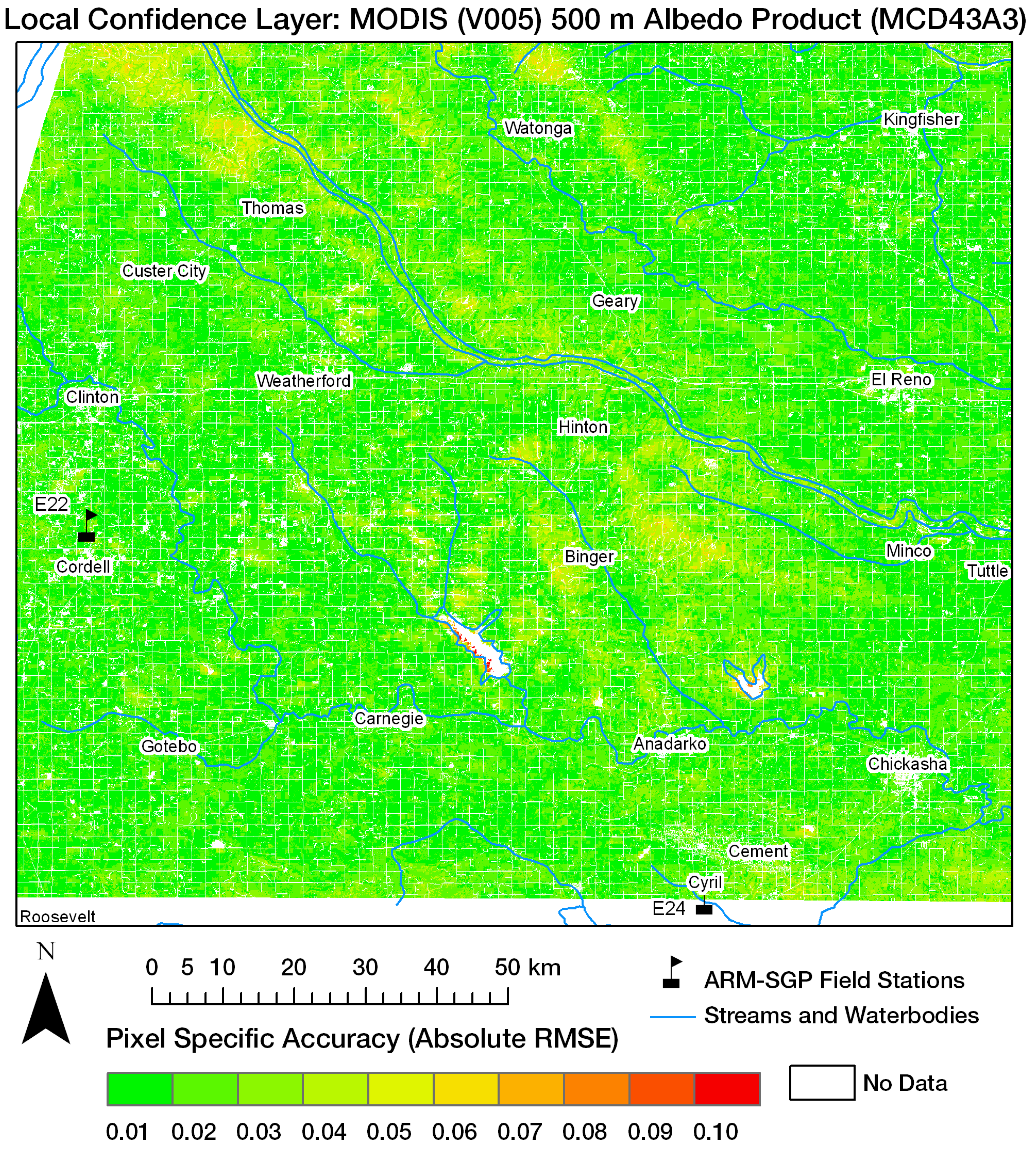

Figure 4.14. Local uncertainty map of the Little Washita Watershed (and vicinity) showing the absolute RMSE field values between blue-sky albedo retrievals at LSN from MC43A3 and the local (50 m) upscaling approach.

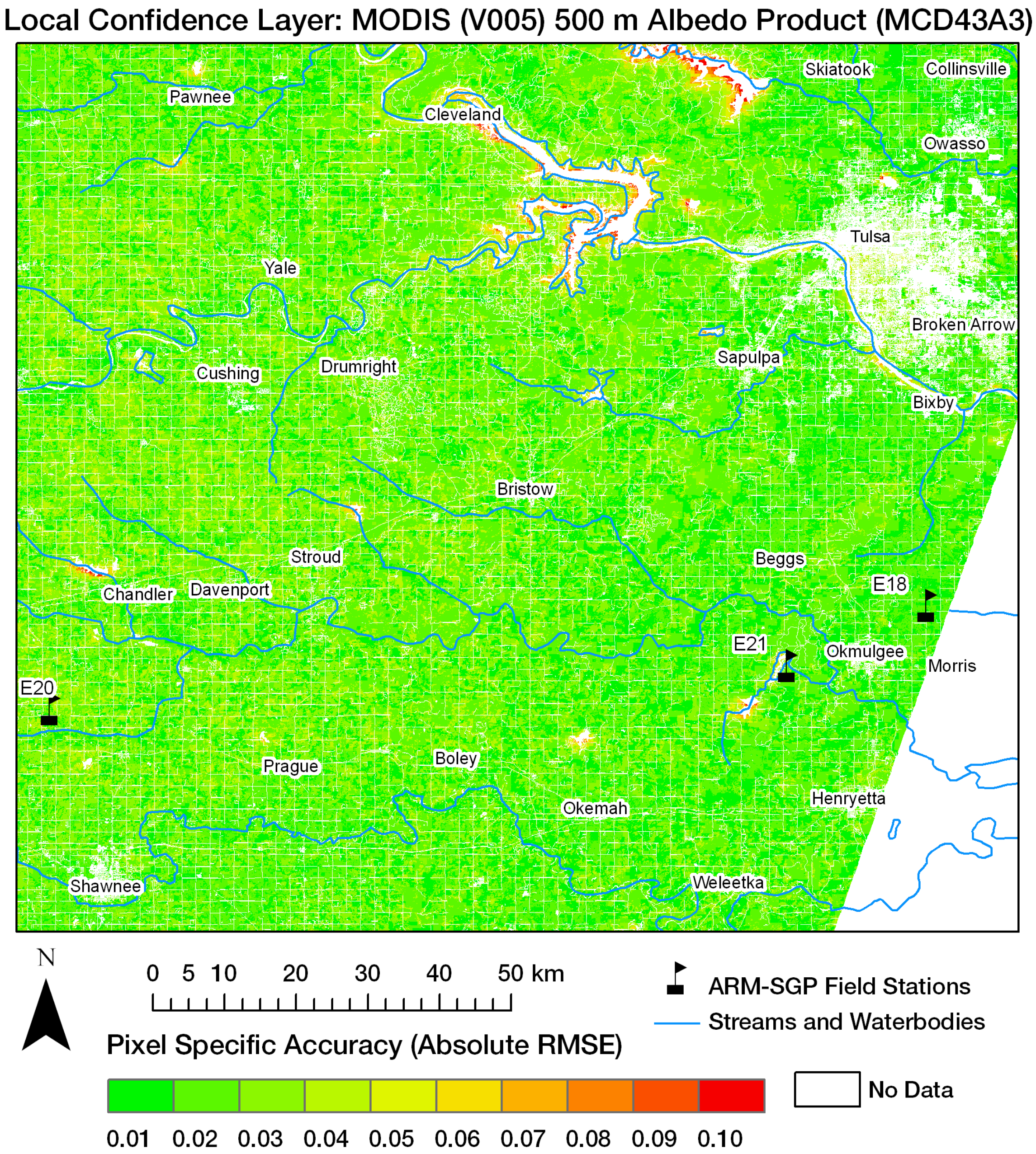

Figure 4.15. Local uncertainty map of the Okmulgee Forest Site (and vicinity) showing the absolute RMSE field values between blue-sky albedo retrievals at LSN from MC43A3 and the local (50 m) upscaling approach.

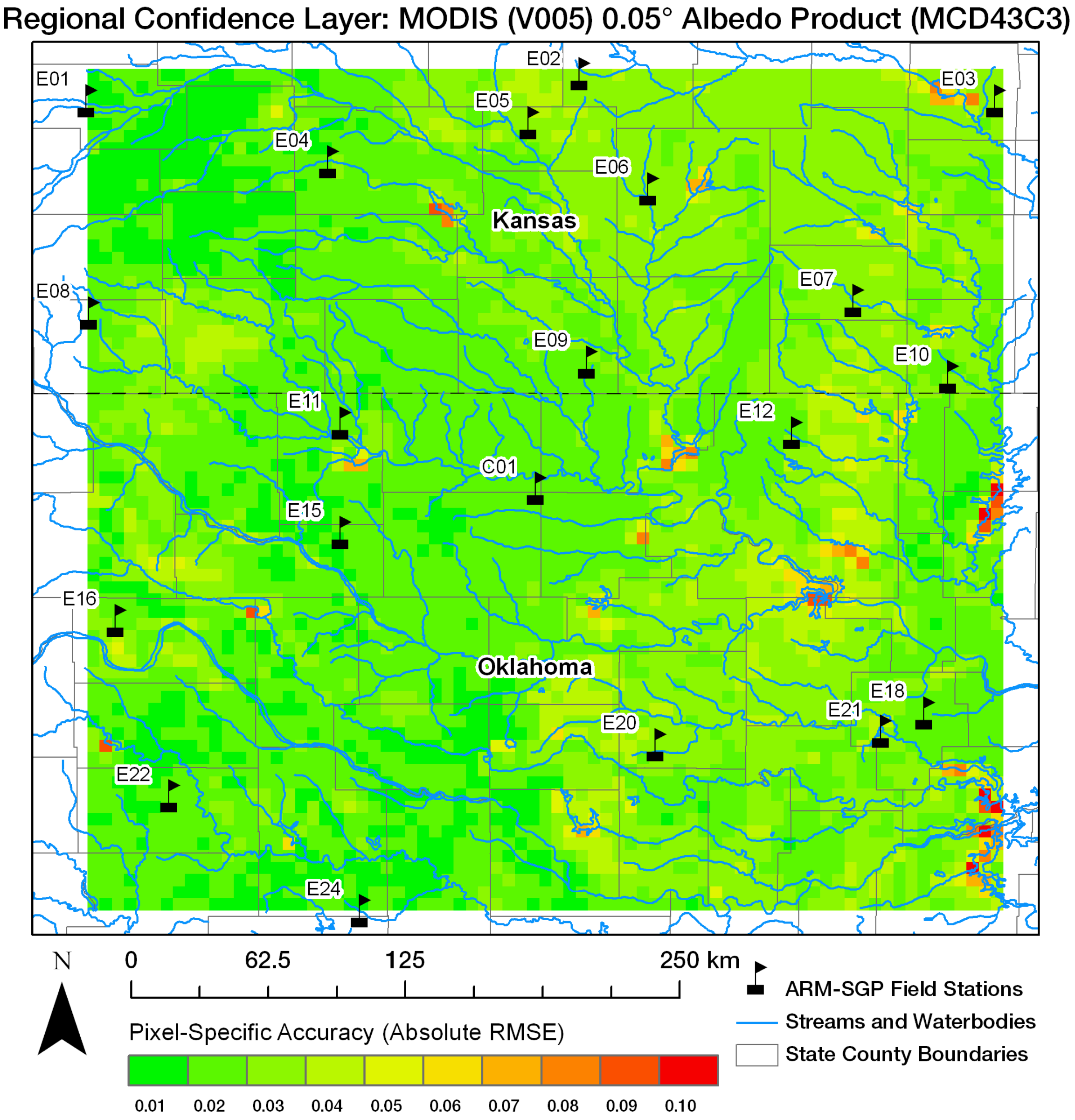

Figure 4.16. Regional uncertainty map of the SGP region showing the absolute RMSE field values between blue-sky albedo retrievals at LSN from MC43C3 and the regional upscaling approach.

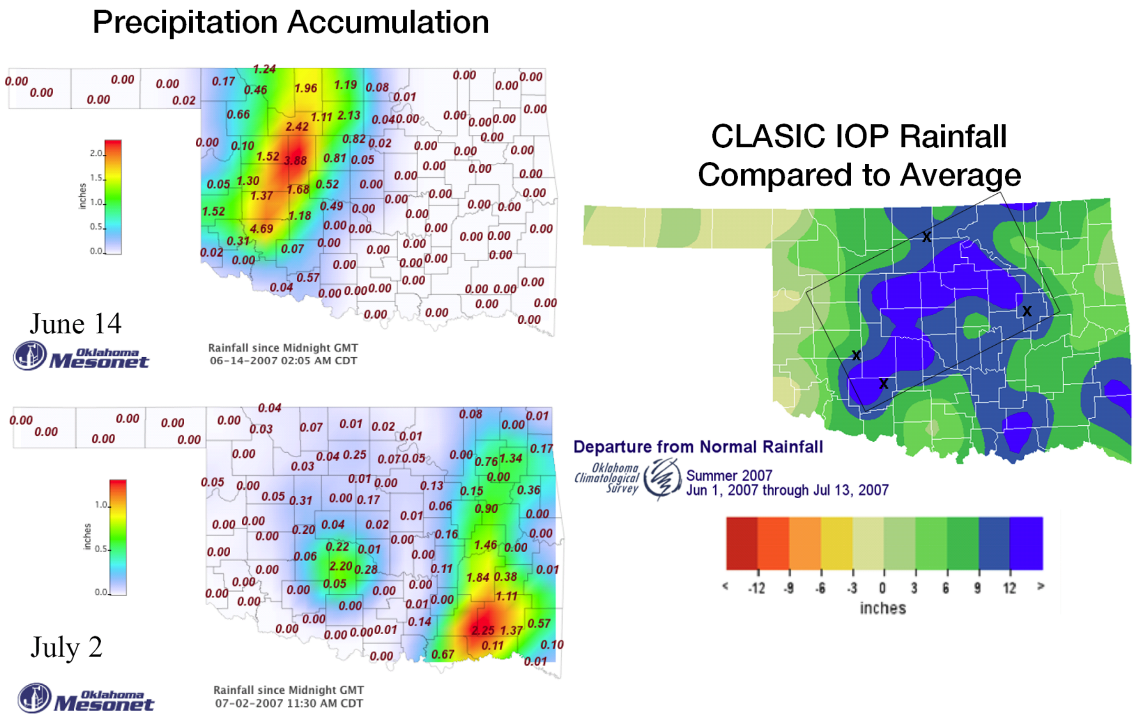

Figure 4.17. (Left) Cumulative rainfall maps (from midnight GMT) for the state of Oklahoma during 14 June, 2007 (top) and 2 July, 2007 (bottom). Departure from normal rainfall throughout the CLASIC IOP. Credit: Oklahoma Mesonet.

4.6. Conclusions

The key sources of uncertainty on the derived albedo retrievals from the MODIS V005 BRDF/Albedo Products were identified for the 2007 CLASIC Intense Observation Period (IOP). By evaluating the spatial correspondence between daily albedos at LSN from MODIS and the surface albedo fields reconstructed from two independent upscaling schemes, a new set of confidence layers for the MODIS BRDF/Albedo product were created at both local (500 m) and regional modeling scales (0.05°) for the entire 142,000-

square-kilometer SGP region. These layers provide a measure of pixel-specific accuracy for the routine algorithms used in MODIS data processing.

To further close the scaling gaps between the point-based and region-based assessments of spatial representativeness for surface albedo, a new set of routines were developed to establish whether a given field station is spatially representative of the broader regional ecosystems. The approach produces a transition stage for the MODIS V005 BRDF/Albedo product based on a linear weighting function of the primary/secondary vegetation types that is resolved by the sensor over a given field station. Assessments of regional representativeness over the ARM-SGP Central Facility suggest that the broader regional ecosystems are being captured by this intensely measured station.

Surface albedo fields were reconstructed from ground-truth observations by implementing: (1) a local upscaling scheme, which uses fine scale retrievals of representative BRDFs as derived from CAR observations during the CLASIC IOP; and (2) a regional upscaling scheme based on ordinary kriging interpolation of tower albedo measurements. For the latter, a series of exploratory data analyses were performed, including descriptive statistics, to provide an indication of the goodness of fit in the kriging predictions and to estimate the variability of the predictions from the measured values. Given the wide distribution of field stations measuring ground albedos across the SGP region (both in terms of quantity and quality), results show that the ARM-SGP network is able to reduce the variance error of estimation for MODIS retrievals, and thus provide consistent in-situ signatures that are suitable for use in rigorous applications at the spatial scales at which regional and global models are commonly utilized. Comparisons between the two upscaling methods (CAR & ordinary kriging) and the MODIS datasets (i.e. 500 m and 0.05°) were also performed. Results show that the intrinsic scaling effects between the two MODIS datasets were well under 0.0075 units of absolute RMSE. The local upscaling approach was much more accurate than the regional method in capturing the underlying surface conditions in the SGP region.

The CLASIC IOP experienced anomalous rainfall conditions that resulted in widespread and repeated flooding throughout Oklahoma and Texas including significant loss of life and property. The major sources of uncertainty were thus found in the vicinity of streams and water bodies all across the SGP region. Unfortunately, both the local and regional upscaling routines were unable to capture the anomalous rainfall conditions that were responsible for the consistent drop in the albedo (and thus in accuracy) over such inundated landscapes. Over these areas, the MODIS albedos were within ±0.050-0.065 units of absolute RMSE when compared against retrievals acquired in-situ.

Chapter 5

5. Concluding remarks

The role played by scale in models describing the Bidirectional Reflectance Distribution Function (BRDF) and albedo of land surfaces needs to be understood in terms of the multidirectional and multispectral signatures acquired from multiple sensor platforms. This effort focused on comparisons between satellite, airborne, and ground measurements, namely, MODerate Resolution Imaging Spectroradiometer (MODIS) BRDF and Albedo products, airborne angular reflectance measurements from NASA's Cloud Absorption Radiometer (CAR), and tower albedo measurements.

The BRDF describes the surface reflectance explicitly in terms of its spectral, directional, spatial, and temporal properties. It provides an improved understanding of the physical processes of light interaction with vegetation canopies and has the added practical benefit of allowing improved interpretation of remotely sensed data (Ni et al. 1999). The availability of a large number of directional reflectances available from a particular land surface over a wide angular range can effectively capture its surface anisotropy and thus be used to accurately model the surface albedo. The MODIS V005 BRDF/Albedo product provides the RossThick-LiSparseReciprocal (RTLSR) BRDF kernel model parameters, which can be used to compute the intrinsic black-sky albedo (directional-hemispherical reflectance) and white-sky albedo (bihemispherical reflectance under isotropic illumination) quantities. To accurately couple these satellite-derived intrinsic quantities with field and airborne-derived albedos, the MODIS black-sky and white-sky quantities must be combined as function of solar geometry and atmospheric state. With knowledge of the latter, actual surface albedo retrievals can be derived. Actual surface albedo is therefore a continuously varying function of both the specific atmospheric conditions that modulate the incoming solar irradiance as well as the intrinsic anisotropic scattering of the surface as determined by the reflected irradiance. Consequently, an accurate estimation of actual surface albedo is dependent on an accurate description of the overlying atmosphere as well as the intrinsic reflective properties of the underlying surface (i.e. the intrinsic albedo) at a specific point in time.

While previous validation studies have evaluated the consistency of the MODIS BRDF/Albedo Products at different spatial and temporal resolutions, uncertainties due to spatial scale continue to plague such efforts. Knowledge of the spatial representativeness between tower measurements of surface albedo and MODIS retrievals has significant implications in the efficiency of such direct “point-to-pixel” comparisons. In view of that, a new validation framework for the estimation of the spatial representativeness of tower albedo measurements was developed. This method brings together knowledge of the intrinsic biophysical properties of a given spatial domain and its surrounding landscape to produce a number of geostatistical attributes that describe the overall variability, spatial extent, strength, and temporal structure of surface albedo patterns at separated seasonal periods throughout the year. The resulting product is a set of geostatistical measures derived from the principles of traditional variography that can be used to quantify the degree of spatial representativeness between the prescribed footprint and its surrounding landscape at different seasonal periods throughout the year.

Ground observations acquired over the broad range of forested landscapes that are part of the AmeriFlux network of sites were found to generally capture the footprint of MODIS observations. However, measurement sites instrumented with tower albedometers at very low heights above ground level (< 20 m) or in close proximity to significantly different surface conditions experienced difficulties in capturing the albedo retrievals from the MODIS satellite footprint during some or all seasons. This validation framework contributes to an improved methodology for quantifying the uncertainties and identifying possible sources of error in the MODIS retrievals. These errors can be described both in terms of the quality of the algorithm inversions (e.g. given a limited number of cloud-free satellite retrievals) and their ability to capture the underlying spatial and temporal variability of the surrounding landscape.

The BRDF is important in modeling atmospheric shortwave radiative fluxes (Loeb et al. 2003; Pinker et al. 1995), in modeling the energy exchange in the coupled soil-vegetation-atmosphere system (Dickinson 1983; Kustas et al. 2004) in retrieving cloud and aerosol properties from radiance measurements (Chiu et al. 2004; Marshak and Davis 2005), and in improving vicarious calibration techniques (Thome et al. 2003; Yoshida et al. 2005). The role played by scale in models describing the BRDF of land surfaces, however, needs to be fully understood before the most effective production and validation of BRDF retrievals that are extracted from airborne and satellite data can be devised.

Accordingly, airborne measurements from NASA's Cloud Absorption Radiometer were taken over agricultural and natural landscapes in the Southern Great Plains (SGP) region during the 2007 Cloud and Land Surface Interaction Campaign (CLASIC) Intense Observing Period (IOP). These measurements were processed using a spatial transformation and scaling routine, whereby the directional surface reflectances derived from the CAR are efficiently transformed into image space to recreate the same measurement methodology, spatial coverage, and data processing protocols to retrieve surface BRDFs as employed by the MODIS standard processing. Results over the ARM-SGP Central Facility during the CLASIC IOP provide fine-scale retrievals of the BRDF, using 50 m and 100 m spatial grids for each of the archetypal landscapes within the SGP region, over eight spectral bands, and three broadbands. Local upscaling results between the BRDF retrievals from the CAR and MODIS sensors show a good degree of correspondence between the three spatial grids, with results being consistently under 0.05 absolute RMSE (in reflectance units) or 17% relative RMSE, for both the narrowband and broadband retrievals. However, results in the visible domain of the spectrum were found to be more sensitive to changes in the backscattering region of the BRDF hemisphere, and consequently, to solar zenith angle variations, particularly when MODIS grids are directly compared against the finer-scale retrievals from CAR.

The diurnal performance of the MODIS V005 BRDF/Albedo algorithm and CAR retrievals was also evaluated using field measurements of albedo over the ARM-SGP Central Facility throughout the period of CLASIC. The overall accuracies of both the CAR and MODIS albedos were within 0.02 units of absolute RMSE, but show a decreasing trend with underestimation as the solar zenith angle increases to > 70°. Assessments of spatial representativeness at the SGP Central Facility indicate that the surface conditions inside the footprint of the 60 m radiation tower are much different from the surrounding region extending to the MODIS footprint. Results from semivariogram functions further suggest that a direct assessment between tower measurements and the MODIS satellite retrievals will result in residual scaling errors. This may clarify the negative biases of ~0.03 units seen in the MODIS albedo retrievals.

A major finding in this study is that both the uncertainties and the close agreement between the CAR and MODIS retrievals confirm the untested prediction that the spatial degradation of modeled reflectances can be achieved through degradation of the RossThick-LiSparseReciprocal BRDF kernel model parameters. The spectral consistency of the BRDF model parameters, using both narrowband and broadband retrievals at increased scales of resolution, further suggests that the RTLSR model, and perhaps linear BRDF models in general, are capturing the underlying surface heterogeneities of the archetypal landscapes observed in this study.

Surface albedo fields were reconstructed from ground-truth observations by implementing: (1) a local upscaling scheme, which uses fine scale retrievals of representative BRDFs as derived from CAR observations during the CLASIC IOP; and (2) a regional upscaling scheme based on ordinary kriging interpolation of tower albedo measurements. For the latter, a series of exploratory data analyses were performed, including descriptive statistics, to provide an indication of the goodness of fit in the kriging predictions and to estimate the variability of the predictions from the measured albedo values. Comparisons between confidence layers show consistent agreement particularly over areas where the uncertainties between datasets are greater. Given the wide distribution of field stations measuring ground albedos across the SGP region (both in terms of quantity and quality), results show that the ARM-SGP network is able to reduce the variance error of estimation for MODIS retrievals, and thus provide consistent in-situ signatures that are suitable for use in rigorous applications at the spatial and temporal scales at which regional and global models are commonly utilized.

To further close the scaling gaps between the point-based and region-based assessments of spatial representativeness for surface albedo, a new transition stage for the MODIS V005 BRDF/Albedo product was developed. This method can be particularly useful for (1) estimating whether measurement site can be treated as a representative sample of its regional landscape; and (2) quantifying the ability of the MODIS CMG data to capture the spatial and seasonal signatures specific that site. Assessments over the ARM-SGP Central Facility, suggest that the broader regional ecosystems are being captured by this intensely measured station. Future efforts will focus on implementing this transition stage over the entire array of measurements sites in the SGP region. By constraining the albedos from ground observations based on their ability to capture the regional signatures specific to each location, these assessments will result in increased levels of confidence.

As production moves from MODIS data to NPP and NPOESS data, user specifications require that production also moves from the current multi-date approach to daily albedo computations. Thus, the spatial characteristics from directional observations determined from BRDFs acquired during a single day overpass will have to be thoroughly examined to ensure that the algorithms are holding on throughout periods of rapidly changing surface conditions. Assessments of spatial representativeness under such dynamic scenarios will thus improve the confidence in the validation results. Additional improvements to this methodology will further enhance our understanding of the spatial dependencies intrinsic to a given field station under snow-covered conditions. By obtaining coincident observations from high-resolution imagery, the spatial characteristics of a measurement site can be captured in-situ both before and after a snow event. These enhancements would minimize the retrieval uncertainties in the daily snow-albedo retrievals from MODIS.

In the coming decade NASA's Earth Science Division will be facing a challenge to implement Venture-class missions as recommended by the National Research Council Decadal Survey, to incorporate an optimal mix of space-based and suborbital sensor platforms. A complete characterization of finer-scale BRDFs, and the albedos derived from them, using independent retrievals from the CAR at different spatial scales will leverage opportunities in these missions. Future efforts will focus on applying the newly developed CAR BRDF/Albedo product by using the information-rich data library of CAR measurements over a wide range of terrestrial ecosystems (see: http://car.gsfc.nasa.gov/data/). The fine scale retrievals of archetypal landscapes as derived by the Cloud Absorption Radiometer (CAR) will also be used to drive the anisotropic response over the full regional extent of these measurement sites. Results from these analyses will thus improve parameterization of the lower boundary forcing conditions in models such as climate, biogeochemical, hydrological, and weather forecast models and will guide future modifications of the CAR instrument to meet the rigorous expectations of Decadal Survey missions. This combination of one-of-a-kind maps of the bidirectional reflectance distribution function (BRDF) and albedo of unique landscapes will have broad utility, specifically to be used to: (1) acquire representative BRDF and albedo retrievals from areas comparable to global modeling grids (~0.05 – 2.0°), for shortwave radiation closure studies; (2) provide ground-truth layers for intercomparisons between current and future global surface albedo and reflectance anisotropy products; and (3) provide spatially characterized retrievals of land surface BRDFs to improve vicarious calibration techniques over the operational dynamic range of moderate-to-high spatial resolution sensors (VIS to SWIR). For the latter, the CAR data library currently holds datasets from a number of actively managed calibration sites. These records offer the extremely rare opportunity for deriving spatially-characterized BRDFs to improve model-based vicarious calibration techniques specific to these calibration sites. Spatially characterized retrievals over these regions are currently needed to address the higher-order spatial and directional uncertainties associated to their natural environment (Thome et al. 2001).

A new set of confidence layers for the MODIS BRDF/Albedo products were developed at both local and regional modeling scales for the entire 142,000-square-kilometer SGP region. These layers provide a measure of pixel-specific accuracy for the routine algorithms used in the MODIS data processing at both local (500 m) and regional (0.05°) scales. Using these validation and assessment methodologies, the key sources of uncertainty on the derived albedo retrievals from the MODIS V005 BRDF/Albedo Products during the CLASIC Intense Observing Period (IOP) were identified. Results show that the intrinsic scaling effects between the two MODIS datasets are well under 0.0075 units of absolute RMSE. Another key finding was that the local upscaling approach can accurately captured the underlying surface conditions in the SGP region. These results demonstrate the utility of the fine-scale retrievals of archetypal landscapes derived from the CAR instrument. These datasets utilize a measurement methodology that is truly consistent with the MODIS albedo retrievals at both local and regional modeling scales. Thus, this method can further be used to provide areally-weighed signatures specific to the larger set of spatial domains that are directly assimilated in regional and global modeling schemes.

Future efforts will also focus on combining the additional ancillary data sources obtained throughout the CLASIC-IOP, such as fine scale maps of soil moisture, vegetation water content, and crop phenology. These layers could be translated into predictive components of surface albedo dynamics. This would have the dual benefit of further enhancing the confidence in the MODIS albedo retrievals at multiple spatial scales throughout the growing season and improving our understanding of the relationships between surface albedo and land surface-atmosphere interactions for climate models and watershed models.

Bibliography

Abdou, W.A., Helmlinger, M.C., Conel, J.E., Bruegge, C.J., Pilorz, S.H., Martonchik, J.V., & Gaitley, B.J. (2001). Ground measurements of surface BRF and HDRF using PARABOLA III. *Journal of Geophysical Research-Atmospheres, 106*, 11967-11976.

Ackerman, T.P., & Stokes, G. (2003). The atmospheric radiation measurement program. *Physics Today, 56*, 38–45.

Baccini, A., Friedl, M.A., Woodcock, C.E., & R., W. (2004). Forest biomass estimation over regional scales using multisource data. *Geophysical Research Letters, 31*, L10501.

Baret, F., Morisette, J.T., Fernandes, R.A., Champeaux, J.L., Myneni, R.B., Chen, J., Plummer, S., Weiss, M., Bacour, C., Garrigues, S., & Nickeson, J.E. (2006). Evaluation of the representativeness of networks of sites for the global validation and intercomparison of land biophysical products: Proposition of the CEOS-BELMANIP. *IEEE Transactions on Geoscience and Remote Sensing, 44*, 1794-1803.

Berbet, M.L., & Costa, M.H. (2003). Climate change after tropical deforestation: seasonal variability of surface albedo and its effects on precipitation change. *Journal of Climate, 16*, 2099-2104.

Carroll, S.S., & Cressie, N. (1996). A Comparison of Geostatistical Methodologies Used to Estimate Snow Water Equivalent. *Water Resources Bulletin, 32*, 267-278.

Chen, J.M., & Leblanc, S.G. (1997). A four-scale bidirectional reflectance model based on canopy architecture. *IEEE Transactions on Geoscience and Remote Sensing, 35*, 1316-1337.

Chen, J.M., Leblanc, S.G., Cihlar, J.C., Bicheron, P., Leroy, M., Deering, D., & Eck, T. (1997). Studies of BRDF in conifer and deciduous boreal forests using the 4-scale model and airborne POLDER and ground-based PARABOLA measurements. In I.G.a.R. Sensing (Ed.), *IEEE International Geoscience & Remote Sensing Symposium* (pp. 165-167). Singapore: IEEE International.

Chiu, J.-Y.C., Marshak, A., & Wiscombe, W.J. (2004). The effect of surface heterogeneity on cloud absorption estimates. *Geophysical Research Letters, 31*, L15105, doi:10.1029/2004GL020104.

Cooper, S.D., Barmuta, L., Sarnelle, O., Kratz, K., & Diehl., S. (1997). Quantifying spatial heterogeneity in streams. *Journal of the North American Benthological Society, 16*, 174-188.

Cosh, M.H. (2007). Cosh, M. (2007). SGP Cloud and Land Surface Interaction Campaign (CLASIC) Land Surface States and Fluxes Experiment Plan. In: Atmospheric Radiation Measurement (ARM) Program.

Cressie, N. (1993). *Statistics for Spatial Data, Revised Edition*. New York: John Wiley & Sons.

Curtis, P.S., Hanson, P.J., Bolstad, P., Barford, C., Randolph, J.C., Schmid, H.P., & Wilson, K.B. (2002). Biometric and eddy-covariance based estimates of annual carbon storage in five eastern North American deciduous forests. *Agricultural and Forest Meteorology, 113*, 3-19.

Davis, J.C. (1986). *Statistics and data analysis in geology*. New York: Wiley.

Davis, K.J., Bakwin, P.S., Yi, C.X., Berger, B.W., Zhao, C.L., Teclaw, R.M., & Isebrands, J.G. (2003). The annual cycles of CO2 and H2O exchange over a northern mixed forest as observed from a very tall tower. *Global Change Biology, 9*, 1278-1293.

Dent, C.L., & Grimm, N.B. (1999). Spatial heterogeneity of stream water nutrient concentrations over successional time. *Ecology, 80*, 2283-2298.

Dickinson, R.E. (1983). Land Surface Processes and Climate Surface Albedos and Energy-Balance. *Advances in Geophysics, 25*, 305-353.

Dickinson, R.E., Pinty, B., & Verstraete, M.M. (1990). Relating surface albedos in GCMs to remotely sensed data. *Agricultural and Forest Meteorology, 32*, 109-131.

Doraiswamy, P.C., Hatfield, J.L., Jackson, T.J., Akhmedov, B., Prueger, J., & Stern, A. (2004). Crop condition and yield simulations using Landsat and MODIS. *Remote Sensing of Environment, 92*, 548-559.

Downing, J.A. (1991). Biological heterogeneity in aquatic ecosystems. In J. Kolasa & S.T.A. Pickett (Eds.), *Ecological heterogeneity* (pp. 160-180). New York, NY, USA: Springer-Verlag.

Dubovik, O., & King, M.D. (2000). A flexible inversion algorithm for retrieval of aerosol optical properties from Sun and sky radiance measurements. *Journal of Geophysical Research, 105*, 20673-20696.

Ferranti, L., & Viterbo, P. (2006). The European Summer of 2003: Sensitivity to Soil Water Initial Conditions. *Journal of Climate, 19*, 3659-3680.

Finkral, A.J., & Evans, A.M. (2008). The effect of a thinning treatment on carbon stocks in a northern Arizona forest. *Forest Ecology and Management, 255*, 2743-2750.

Friedl, M.A., & Brodley, C.E. (1997). Decision tree classification of land cover from remotely sensed data. *Remote Sensing of Environment, 61*, 399-409.

Friedl, M.A., McIver, D.K., Hodges, J.C.F., Zhang, X.Y., Muchoney, D., Strahler, A.H., Woodcock, C.E., Gopal, S., Schneider, A., Cooper, A., Baccini, A., Gao, F., & Schaaf, C.B. (2002). Global land cover mapping from MODIS: algorithms and early results. *Remote Sensing of Environment, 83*, 287-302.

Friedl, M.A., & Strahler, A.H. (2000). Mapping global land cover using the MODIS land cover classification algorithm: Recent progress and initial results. *EOS Transactions of the American Geophysical Union*.

Gao, F., Schaaf, C.B., Strahler, A.H., Jin, Y.F., & Li, X. (2003). Detecting vegetation structure using a kernel-based BRDF model. *Remote Sensing of Environment, 86*, 198-205.

Gatebe, C.K., Butler, J.M., Cooper, J.W., Kowalewski, M., & King, M.D. (2007). Characterization of errors in the use of integrating-sphere systems in the calibration of scanning radiometers. In, *Applied Optics* (pp. 7640-7651).

Gatebe, C.K., Dubovik, O., & King, M.D. (2009). Simultaneous retrieval of aerosol and surface optical properties from combined airborne- and ground-based direct and diffuse radiometric measurements. *(In Preparation)*.

Gatebe, C.K., King, M.D., Lyapustin, A.I., Arnold, G.T., & Redemann, J. (2005). Airborne Spectral Measurements of Ocean Directional Reflectance. *Journal of Atmospheric Sciences, 62*, 1072-1092.

Gatebe, C.K., King, M.D., Platnick, S., Arnold, G.T., Vermote, E.F., & Schmid, B. (2003). Airborne spectral measurements of surface-atmosphere anisotropy for several surfaces and ecosystems over southern Africa. *Journal of Geophysical Research, 108*, 1-16, doi:10.1029/2002JD002397.

Geiger, B., Carrer, D., Franchistéguy, L., Roujean, J.L., & C. Meurey (2008). Land surface albedo derived on a daily basis from Meteosat Second Generation observations. *IEEE Transactions on Geoscience and Remote Sensing, 46*, 3841-3856.

Gough, C.M., C. S. Vogel, H. P. Schmid, H-B. Su, & Curtis, P.S. (2008). Multi-year convergence of biometric and meteorological estimates of forest carbon storage. *Agricultural and Forest Meteorology, 148*, 158-170.

Goulden, M.L., Winston, G.C., McMillan, A.M.S., Litvak, E.E., Read, E.L., Rocha, A.V., & Elliot, J.R. (2006). An Eddy Covariance Mesonet to Measure the Effect of Forest Age on Land-Atmosphere Exchange. *Global Change Biology, 12*, 2146-2162.

Grant, I., Prata, A., & Ceche, R. (2000). The impact of the diurnal variation of albedo on the remote sensing of the daily mean albedo of grassland. *Journal of Applied Meteorology, 39*, 231-244.

Gu, L.H., Meyers, T.P., Pallardy, S.G., Hanson, P.J., Yang, B., Heuer, M., Hosman, K.P., Riggs, J.S., Sluss, D., & Wullschleger, S.D. (2006). Direct and indirect effects of atmospheric conditions and soil moisture on surface energy partitioning revealed by a prolonged drought at a temperate forest site. *Journal of Geophysical Research-Atmospheres, 111*, D16102, doi:10.1029/2006JD007161.

Haining, R., & Wise, S. (1997). Exploratory Spatial Data Analysis, http://www.ncgia.ucsb.edu/giscc/units/u128/u128.html. In, *NCGIA Core Curriculum in Geographic Information System Sciences*.

Hansen, M.C., DeFries, R.S., Townshend, J.R.G., Carroll, M., Dimiceli, C., & Sohlberg, R.A. (2003). Global Percent Tree Cover at a Spatial Resolution of 500 Meters: First

Results of the MODIS Vegetation Continuous Fields Algorithm. *Earth Interactions, 7*.

Henderson-Sellers, A., & Wilson, M.F. (1983). Surface Albedo Data for Climatic Modeling. *Reviews of Geophysics*, *21*, 1743-1778.

Hernandez-Filho, P., Shimabukuro, Y.E., & Lee, D.C.L. (1993). Final report on the forest inventory project at the Tapajos National Forest. In. Saõ José dos Campos, SP, Brasil: Instituto Nacional de Pesquisas Espaciais.

Hill, M. J., Averill, C., Jiao, Z., Schaaf, C. B., & Armston, J. D. (2008). Relationship of MISR RPV parameters and MODIS BRDF shape indicators to surface vegetation patterns in an Australian tropical savanna. *Canadian Journal of Remote Sensing, 34*, S247-S267.

Holben, B.N., Tanre, D., Smirnov, A., Eck, T.F., Slutsker, I., N., A., Newcomb, W.W., Schafer, J., Chatenet, B., Lavenue, F., Kaufman, Y.J., J., V.-C., Setzer, A., Markham, B., Clark, D., Frouin, R., Halthore, R., Karnieli, A., O'Neill, N.T., Pietras, C., Pinker, R.T., Voss, K., & Zibordi, G. (2001). An emerging ground-based aerosol climatology: Aerosol Optical Depth from AERONET. *Journal of Geophysical Research, 106*, 12067-12097.

Hollinger, D.Y., Aber, J., Dail, B., Davidson, E.A., Goltz, S.M., Hughes, H., Leclerc, M.Y., Lee, J.T., Richardson, A.D., Rodrigues, C., Scott, N.A., Achuatavarier, D., & Walsh, J. (2004). Spatial and temporal variability in forest-atmosphere CO2 exchange. *Global Change Biology, 10*, 1689-1706.

Isaaks, E.H., & Srivastava, R.M. (1989). *An introduction to applied geostatistics*. New York: Oxford University Press.

Jackson, T.J., Chen, D., Cosh, M.H., Li, F., Anderson, M., Walthall, C., Doraiswamy, P., & Hunt, E.R. (2004). Vegetation water content mapping using Landsat data derived normalized difference water index for corn and soybeans. *Remote Sensing of Environment, 92*, 475-482.

Jenkins, J.P., Richardson, A.D., Braswell, B.H., Ollinger, S.V., Hollinger, D.Y., & Smith, M.L. (2007). Refining light-use efficiency calculations for a deciduous forest canopy using simultaneous tower-based carbon flux and radiometric measurements. *Agricultural and Forest Meteorology, 143*, 64-79.

Jin, Y.F., Schaaf, C.B., Gao, F., Li, X.W., Strahler, A.H., Lucht, W., & Liang, S.L. (2003a). Consistency of MODIS surface bidirectional reflectance distribution function and albedo retrievals: 1. Algorithm performance. *Journal of Geophysical Research-Atmospheres, 108*, D5.

Jin, Y.F., Schaaf, C.B., Woodcock, C.E., Gao, F., Li, X.W., Strahler, A.H., Lucht, W., & Liang, S.L. (2003b). Consistency of MODIS surface bidirectional reflectance distribution function and albedo retrievals: 2. Validation. *Journal of Geophysical Research-Atmospheres, 108*, D5.

Journel, A.G., & Huijbregts, C.J. (1978). *Mining geostatistics*. New York, NY, USA: Academic Press.

Kaufman, Y.J. (1989). The atmospheric effect on remote sensing and its correction. In G. Asrar (Ed.), *Theory and Applications of Optical Remote Sensing* (pp. 336–428). New York: John Wiley.

Kimes, D., P., S., & W., N. (1987). Hemispherical reflectance variations of vegetation canopies and implications for global and regional energy budget studies. *Journal of Applied Meteorology, 26*, 959-972.

King, M.D. (1981). A method for determining the single scattering albedo of clouds through observation of the internal scattered radiation field

Journal of Atmospheric Sciences, 38, 2031-2044.

King, M.D. (1992). Directional and spectral reflectance of the Kuwait oil-fire smoke. *Journal of Geophysical Research, 97*, 14545-14549.

King, M.D., & Herring, D.D. (2000). Monitoring Earth’s vital signs. *Scientific American, 282*, 72–77.

King, M.D., Radke, L.F., & Hobbs, P.V. (1990). Determination of the spectral absorption of solar radiation by marine stratocumulus clouds from airborne measurements within clouds. *Journal of Atmospheric Sciences, 47*, 894-907.

King, M.D., Strange, M.G., Leone, P., & Blaine, L.R. (1986). Multiwavelength scanning radiometer for airborne measurements of scattered radiation within clouds. *Journal of Atmospheric and Oceanic Technology, 3*, 513-522.

Knobelspiesse, K.D., Cairns, B., Schmid, B., Román, M., & Schaaf, C.B. (2008). Surface BRDF estimation from an aircraft compared to MODIS and ground estimates at the Southern Great Plains site. *Journal of Geophysical Research-Atmospheres, 113*, D20, doi:10.1029/2008JD010062.

Kotchenova, S.Y., Vermote, E.F., Matarrese, R., & Klemm, F.J. (2006). Validation of a vector version of the 6S radiative transfer code for atmospheric correction of satellite data. Part I: Path Radiance. *Applied Optics, 45*, 6726-6774.

Kustas, W.P., Li, F., Jackson, T.J., Prueger, J.H., MacPherson, J.I., & Wolde, M. (2004). Effects of remote sensing pixel resolution on modeled energy flux variability of croplands in Iowa. *Remote Sensing of Environment, 92*, 535-547.

Law, B.E., Falge, E., Gu, L., Baldocchi, D.D., Bakwin, P., Berbigier, P., Davis, K., Dolman, A.J., Falk, M., Fuentes, J.D., Goldstein, A., Granier, A., Grelle, A., Hollinger, D.Y., Janssens, I.A., Jarvis, P., Jensen, N.O., Katul, G., Mahli, Y., & Matteucci, G. (2002). Environmental controls over carbon dioxide and water vapor exchange of terrestrial vegetation. *Agricultural and Forest Meteorology, 113,* 97-120.

Lawrence, P.J., & Chase, T.N. (2007). Representing a new MODIS consistent land surface in the Community Land Model (CLM 3.0). *Journal of Geophysical Research-Biogeosciences, 112*, G01023, doi:10.1029/2006JG000168.

Lean, J., & Rowntree, P.R. (1997). Understanding the sensitivity of a GCM simulation of Amazonian deforestation to the specification of vegetation and soil characteristics. *Journal of Climate, 10*, 1216–1235.

Leblanc, S.G., Bicheron, P., Chen, J.M., Leroy, M., & Cihlar, J. (1999). Investigation of directional reflectance in boreal forests with an improved four-scale model and airborne POLDER data. *IEEE Transactions on Geoscience and Remote Sensing, 37*, 1396-1414.

Leroy, M., & Hautecoeur, O. (1999). Anisotropy-corrected vegetation indexes derived from POLDER ADEOS. *IEEE Transactions on Geoscience and Remote Sensing, 37*, 1698-1708.

Lewis, P., & Barnsley, M. (1994). Influence of the Sky Radiance Distribution on Various Formulations of the Earth Surface Albedo. In, *Colloque International Mesures Physiques et Signatures en Teledetection* (pp. 707-716). Val d'Isere, France.

Li, H., & Reynolds, J.E. (1995). On definition and quantification of heterogeneity. *Oikos: A Journal of Ecology, 73*, 280-284.

Li, X.W., & Strahler, A.H. (1992). Geometric-Optical Bidirectional Reflectance Modeling of the Discrete Crown Vegetation Canopy - Effect of Crown Shape and Mutual Shadowing. *IEEE Transactions on Geoscience and Remote Sensing, 30*, 276-292.

Li, Z., Cihlar, J., Zheng, X., Moreau, L., & Ly, H. (1996). The bidirectional effects of AVHRR measurements over boreal regions

IEEE Transactions on Geoscience and Remote Sensing, 34, 1308-1322.

Liang, S. (2001). Narrowband to Broadband Conversion of Land Surface Albedo. I. Algorithms. *Remote Sensing of Environment, 76*, 213-238.

Liang, S., Shuey, C., Russ, A., Fang, H., Chen, M., Walthall, C., Daughtry, C., & Jr., R.H. (2003). Narrowband to broadband conversions of land surface albedo. II: Validation. *Remote Sensing of Environment, 84*, 25-41.

Liang, S.L., Fang, H.L., Chen, M.Z., Shuey, C.J., Walthall, C., Daughtry, C., Morisette, J., Schaaf, C., & Strahler, A. (2002). Validating MODIS land surface reflectance and albedo products: methods and preliminary results. *Remote Sensing of Environment, 83*, 149-162.

Liu, J., Schaaf, C.B., Strahler, A.H., Jiao, Z., Shuai, Y., Zhang, Q., Román, M., Augustine, J.A., & Dutton, E.G. (2009). Validation of Moderate Resolution Imaging Spectroradiometer (MODIS) albedo retrieval algorithm: Dependence of albedo on solar zenith angle. *Journal of Geophysical Research-Atmospheres, 114*, D01106, doi:10.1029/2008JD009969.

Loeb, N.G., Manalo-Smith, N., Kato, S., Miller, W.F., Gupta, S.K., Minnis, P., & Wielicki, B.A. (2003). Angular Distribution Models for Top-of-Atmosphere Radiative Flux Estimation from the Clouds and the Earth's Radiant Energy System Instrument on the Tropical Rainfall Measuring Mission Satellite. Part I: Methodology. *Journal of Applied Meteorology, 42*, 240-265.

Loescher, H.W., & Munger, J.W. (2006). Preface; New approaches to quantifying exchanges of carbon and energy across a range of scale. *Journal of Geophysical Research, 111*, D14S91 doi:10.1029/2006JD007135.

Lucht, W., Schaaf, C.B., & Strahler, A.H. (2000). An algorithm for the retrieval of albedo from space using semi-empirical BRDF models. *IEEE Transactions on Geoscience and Remote Sensing, 38*, 977-967.

Luo, Y., Trishchenko, A., Latifovic, R., & Li, Z. (2003). Surface bi-directional reflectance properties over the arm sgp area from satellite multi-platform observations. In D. Carrothers (Ed.), *Thirteenth Atmospheric Radiation Measurement (ARM) Science Team Meeting* (pp. 1-12). Richland, Wash.: Department of Energy.

Marshak, A., & Davis, A. (2005). *Three-dimensional radiative transfer in cloudy atmospheres*: Springer, Verlag.

Martonchik, J., Bruegge, C., & Strahler, A.H. (2000). A Review of Reflectance Nomenclature Used in Remote Sensing. *Remote Sensing Reviews, 19*, 9-20.

Materon, G. (1963). Principles of Geostatistics. *Economic Geology, 58*, 1246-1266, DOI: 10.2113/gsecongeo.58.8.1246.

McArthur, L.B.J. (2004). Baseline Surface Radiation Network (BSRN) Operations Manual Version 2.1. Technical Report. In: World Climate Research Program.

McMillan, A.M.S., & Goulden, M.L. (2008). Age-dependent variation in the biophysical properties of boreal forests. *Global Biogeochemical Cycles, 22*, GB2019.

Miller, S.D., Goulden, M.L., Menton, M.C., da Rocha, H.R., Freitas, H.C., Figueira, A.M.S., & de Sousa, C.A.D. (2004). Biometric and micrometeorological measurements of tropical forest carbon balance. *Ecological Applications, 14*, S114-S126.

Morcrette, J.-J. (2000). *Assessment of the ECMWF model cloudiness and surface radiation fields at the ARM-SGP site*. Reading,.

Morisette, J.T., Baret F., Liang S., (2006). Special issue on Global Land Product Validation, *IEEE Transactions of Geoscience and Remote Sensing*, 44, 1695-1697.

Ni, W., Li, X., Woodcock, C.E., Caetano, M.R., & Strahler, A.H. (1999). An analytical hybrid GORT model for bidirectional reflectance over discontinuous plant canopies. *IEEE Transactions of Geoscience and Remote Sensing*, *37*, 987-999.

Nicodemus, F.E. (1977). Geometrical considerations and nomenclature for reflectance. *National Bureau of Standards monograph, no. 160* (pp. 1-52). Washington, DC.

Noreus, J.P., Nyborg, M.R., & Hayling, K.L. (1997). The gravity anomaly field in the Gulf of Bothnia spatially characterized from satellite altimetry and in situ measurements. *Journal of Applied Geophysics, 37*, 67-84, DOI: 10.1016/S0926-9851(97)00007-4.

Oleson, K.W., Bonan, G.B., Schaaf, C.B., Gao, F., Jin, Y.F., & Strahler, A.H. (2003). Assessment of global climate model land surface albedo using MODIS data. . *Geophysical Research Letters, 38*.

Ollinger, S.V., Richardson, A.D., Martin, M.E., Hollinger, D.Y., Frolking, S.E., Reich, P.B., Plourde, L.C., Katul, G.G., Munger, J.W., Oren, R., Smith, M.-L., U, K.T.P., Bolstad, P.V., Cook, B.D., Day, M.C., Martin, T.A., Monson, R.K., & Schmid, H.P. (2008). Canopy nitrogen, carbon assimilation, and albedo in temperate and boreal forests: Functional relations and potential climate feedbacks. *Proceedings of the National Academy of Sciences, 105*, 19336-19341.

Parkinson, C.L. (2003). Aqua: An earth-observing satellite mission to examine water and other climate variables. *IEEE Transactions on Geoscience and Remote Sensing, 41*, 173-183.

Pinker, R.T., Frouin, R., & Li, Z. (1995). A review of satellite methods to derive surface shortwave irradiance. *Remote Sensing of Environment*, *51*, 108–124.

Pinty, B., Roveda, F., Verstraete, M.M., Gobron, N., Govaerts, Y., Martonchik, J.V., Diner, D.J., & Kahn, R.A. (2000). Surface albedo retrieval from Meteosat: Part 1: Theory. *Journal of Geophysical Research, 105*, 18099-18112.

Rechid, D., & Jacob, D. (2006). Influence of monthly varying vegetation on the simulated climate in Europe. *Meteorologische Zeitschrift, 15*, 99-116.

Remer, L.A., Kaufman, Y.J., Tanré, D., Mattoo, S., Chu, D.A., Martins, J.V., Li, R.R., Ichoku, C., Levy, R.C., Kleidman, R.G., Eck, T.F., Vermote, E., & Holben, B.N. (2005). The MODIS Aerosol Algorithm, Products, and Validation. . *Journal of Atmospheric Sciences, 62*, 947–973.

Ricchiazzi, P., Yang, S., Gautier, C., & Sowle, D. (1998). SBDART: a research and teaching software tool for plane-parallel radiative transfer in the earth's atmosphere. *Bulletin of the American Meteorological Society, 79*, 2101-2114.

Roesch, A., Schaaf, C.B., & Gao, F. (2004). Use of Moderate-Resolution Imaging Spectroradiometer Bidirectional Reflectance Distribution Function products to enhance simulated surface albedos. *Journal of Geophysical Research-Atmospheres, 102*, D12105, doi:10.1029/2004JD004552.

Román, M., Schaaf, C.B., Anderson, G.P., Gao, F., Lewis, P., Privette, J.L., Strahler, A.H., & Woodcock, C.E. (2009a). Assessing the Coupling between Surface Albedo derived from MODIS and the Fraction of Diffuse Skylight over Spatially-Characterized Landscapes. *Remote Sensing of Environment*, Submitted.

Román, M., Schaaf, C.B., Woodcock, C.E., Strahler, A.H., Braswell, R.H., Curtis, P.S., Davis, K.J., Gu, L., Goulden, M.L., Hollinger, D.Y., Kolb, T.E., Meyers, T.P., Munger, J.W., Richardson, A.D., Wilson, T.B., & Wofsy, S.C. (2009b). The MODIS BRDF/Albedo Product: Assessment of Pixel-Specific Accuracy over Forested Ecosystems. *Remote Sensing of Environment*, Submitted.

Ross, J. (1981). *The radiation regime and architecture of plant stands*. Norwell, Mass.: The Hague: Dr. W. Junk Publishers.

Running, S.W., Baldocchi, D.D., Turner, D.P., Gower, S.T., Bakwin, P.S., & Hibbard, K.A. (1999). A global terrestrial monitoring network integrating tower fluxes, flask sampling, ecosystem modeling and EOS satellite data. *Remote Sensing of Environment, 70*, 108-127.

Rutan, D.A., Rose, F.G., Smith, N.M., & Charlock, T.P. (2001). Validation data set for CERES surface and atmospheric radiation budget (SARB). In, *World Climate Research Programme (WCRP) Global Energy and Water Cycle Experiment (GEWEX) Newsletter* (pp. 11-12).

Salomon, J.G., Schaaf, C.B., Strahler, A.H., Gao, F., & Jin, Y.F. (2006). Validation of the MODIS Bidirectional Reflectance Distribution Function and Albedo retrievals using combined observations from the Aqua and Terra platforms. *IEEE Transactions on Geoscience and Remote Sensing, 44*, 1555-1565.

Schaaf, C.B., Gao, F., Strahler, A.H., Lucht, W., Li, X., Tsang, T., Strugnell, N.C., Zhang, X., Jin, Y., Muller, J.-P., Lewis, P., Barnsley, M., Hobson, P., Disney, M., Roberts, G., Dunderdale, M., Doll, C., d'Entremont, R., Hu, B., Liang, S., Privette, J.L., & Roy, D.P. (2002). First Operational BRDF, Albedo and Nadir Reflectance Products from MODIS. *Remote Sensing of Environment, 83*, 135-148.

Schaaf, C.B., Martonchik, J., Pinty, B., Govaerts, Y., Gao, F., Lattanzio, A., Liu, J., Strahler, A.H., & Taberner, M. (2008). Retrieval of Surface Albedo from Satellite Sensors. In S. Liang (Ed.), *Advances in Land Remote Sensing: System, Modeling, Inversion and Application* (pp. 219-243): Springer.

Schaepman-Strub, G., Schaepman, M.E., Painter, T.H., Dangel, S., & Martonchik, J.V. (2006). Reflectance quantities in optical remote sensing-definitions and case studies. *Remote Sensing of Environment, 103*, 27-42.

Schmid, H.P., Grimmond, C.S.B., Cropley, F., Offerle, B., & Su, H.B. (2002). Measurements of CO2 and energy fluxes over a mixed hardwood forest in the mid-western United States. *Agricultural and Forest Meteorology, 103*, 357-374.

Sellers, P.J., Meeson, B.W., Hall, F.G., Asrar, G., Murphy, R.E., Schiffer, R.A., Bretherton, F.P., Dickinson, R.E., Ellingson, R.G., Field, C.B., Huemmrich, K.F., Justice, C.O., Melack, J.M., Roulet, N.T., Schimel, D.S., & Try, P.D. (1995). Remote sensing of the land surface for studies of global change: Models & Algorithms Experiments. *Remote Sensing of Environment*, *15*, 3-26.

Sitch, S., Smith, B., Prentice, I.C., Arneth, A., Bondeau, A., Cramer, W., Kaplan, J.O., Levis, S., Lucht, W., Sykes, M.T., Thonicke, K., & Venevsky, S. (2003). Evaluation of ecosystem dynamics, plant geography and terrestrial carbon cycling in the LPJ dynamic global vegetation model. *Global Change Biology*, *9*, 161-185, 10.1046/j.1365-2486.2003.00569.

Strahler, A.H., Lucht, W., Schaaf, C.B., Tsang, T., Gao, F., Li, X., Muller, J.-P., Lewis, P., & Barnsley, M. (1999). MODIS BRDF/Albedo Product: Algorithm Theoretical Basis Document Version 5.0. Technical Report. In: NASA EOS-MODIS.

Strahler, A.H., Townshend, J.T., Muchoney, D., Borak, J.S., Friedl, M.A., Gopal, S., Hyman, A., Moody, A., & Lambin, E. (1996). MODIS land cover and land cover change: Algorithm technical basis document. In (p. 120): NASA EOS-MODIS.

Strugnell, N., Lucht, W., & Schaaf, C.B. (2001). A global albedo data set derived from AVHRR data for use in climate simulations. *Geophysical Research Letters, 28*, 191-194.

Sullivan, B.W., Kolb, T.E., Hart, S.C., Kaye, J.P., Dore, S., & Montes-Helu, M.C. (2008). Thinning reduces soil carbon dioxide but not methane flux from southwestern USA ponderosa pine forests. *Forest Ecology and Management*, *255*, 4047-4055.

Susaki, J., Yasuoka, Y., Kajiwara, K., Honda, Y., & Hara, K. (2007). Validation of MODIS albedo products of paddy fields in Japan. *IEEE Transactions on Geoscience and Remote Sensing, 45*, 206-217.

Tan, B., Woodcock, C.E., Hu, J., Zhang, P., Ozdogan, M., Huang, D., Yang, W., Knyazikhin, Y., & Myneni, R.B. (2006). The impact of gridding artifacts on the local spatial properties of MODIS data: Implications for validation, compositing, and band-to-band registration across resolutions. *Remote Sensing of Environment, 105*, 98-114.

Thome, K.J., Czapla-Myers, J., & Biggar, S.F. (2003). Vicarious calibration of Aqua and Terra MODIS. In, *Society of Photo-Optical Instrumentation Engineers* (pp. 395–405).

Thome, K.J., Smith, N., & Scott, K. (2001). Vicarious calibration of MODIS using Railroad Valley Playa. In, *Geoscience and Remote Sensing Symposium, IGARSS '01* (pp. 1209-1211). Sydney, NSW, Australia: IEEE International.

Tian, Y., Woodcock, C.E., Wang, Y., Privette, J.L., Shabanov, N.V., Zhou, L., Zhang, Y., Buermann, W., Dong, J., Veikkanen, B., Ha¨me, T., Andersson, K., Ozdogan, M., Knyazikhin, Y., & Myneni, R.B. (2004). Multiscale Analysis and Validation of the MODIS LAI Product. II. Sampling Strategy. *Remote Sensing of Environment, 83*, 431-441.

Trishchenko, A., Luo, Y., Li, Z., Park, W., & Khlopenkov, K. (2005). Spectral, temporal and spatial properties of surface BRDF/Albedo over the ARM SGP area from multi-year satellite observations. In, *Fifteenth Atmospheric Radiation Measurement (ARM) Science Team Meeting*. Daytona Beach, Florida.

Urbanski, S., Barford, C., Wofsy, S., Kucharik, C., Pyle, E., Budney, J., McKain, K., Fitzjarrald, D., Czikowsky, M., & Munger, J.W. (2007). Factors controlling CO2 exchange on timescales from hourly to decadal at Harvard Forest. *Journal of Geophysical Research-Biogeosciences, 112*, G02020, doi:10.1029/2006JG000293.

Vermote, E.F., Tanre, D., Deuze, J.L., Herman, M., & Morcrette, J.-J. (1997). Second Simulation of the Satellite Signal in the Solar Spectrum, 6S: an overview, Geoscience and Remote Sensing. *IEEE Transactions on Geoscience and Remote Sensing, 35*, 675-686.

Wang, Z., Zeng, X., Barlage, M., Dickinson, R.E., Gao, F., & Schaaf, C.B. (2004). Using MODIS BRDF and albedo data to evaluate global model land surface albedo. *Journal of Hydrometeorology, 5*, 3-14.

Wanner, W., Li, X., & Strahler, A.H. (1995). On the Derivation of Kernels for Kernel-Driven Models of Bidirectional Reflectance. *Journal of Geophysical Research-Atmospheres, 100*, 21077-21089.

Wanner, W., Strahler, A.H., Hu, B., Lewis, P., Muller, J., Li, X., Schaaf, C.B., & Barnsley, M. (1997). Global retrieval of bidirectional reflectance and albedo over land from EOS MODIS and MISR data: Theory and algorithm. *Journal of Geophysical Research, 102*, 17143-17161.

Wilson, T.B., & Meyers, T.P. (2007). Determining vegetation indices from solar and photosynthetically active radiation fluxes. *Agricultural and Forest Meteorology, 144*, 160-179.

Wolfe, R.E., Nishihama, M., Fleig, A.J., Kuyper, J.A., Roy, D.P., Storey, J.C., & Patt, F.S. (2002). Achieving sub-pixel geolocation accuracy in support of MODIS land science. *Remote Sensing of Environment, 83*, 31-49.

Yang, F. (2006). Parameterizing the dependence of surface albedo on solar zenith angle using atmospheric radiation measurement observations

Alburquerque, NM. In D. Carrothers (Ed.), *Sixteenth ARM Science Team Meeting Proceedings*. Albuquerque, New Mexico: Department of Energy.

Yoshida, M., Murakami, H., Mitomi, Y., Hori, M., Thome, K.J., Clark, D.K., & Fukushima, H. (2005). "Vicarious calibration of GLI by ground observation data. *IEEE Transactions on Geoscience and Remote Sensing, 43*, 2167-2176.

Zhang, X., Friedl, M.A., & Schaaf, C.B. (2006). Global vegetation phenology from Moderate Resolution Imaging Spectroradiometer (MODIS): Evaluation of global patterns and comparison with in situ measurements. *Journal of Geophysical Research*, G04017, doi:10.1029/2006JG000217.

Zhang, X., Friedl, M.A., Schaaf, C.B., Strahler, A.H., Hodges, J.C.F., Gao, F., Reed, B.C., & Huete, A. (2003). Monitoring vegetation phenology using MODIS. *Remote Sensing of Environment, 84*, 471-475.

Zhou, L., Dickinson, R.E., Tian, Y., Zeng, X., Dai, Y., Yang, Z.L., Schaaf, C.B., Gao, F., Jin, Y.F., Strahler, A.H., Myneni, R.B., Yu, H., Wu, W., & Shaikh, M. (2003). Comparison of seasonal and spatial variations of albedos from Moderate-Resolution Imaging Spectroradiometer (MODIS) and Common Land Model. *Journal of Geophysical Research-Atmospheres, 108*, 4488, doi:10.1029/2002JD003326.

Curriculum Vitae

Miguel O. Román
675 Commonwealth Ave. STO-457
Boston MA, 02215-1406, USA
W. 617-353-8033, M. 617-999-7996, F. 617-353-8399
romanm@ieee.org

Summary

For the past four years, I have been working as a NASA-GSRP fellow with Professors Crystal B. Schaaf, Alan H. Strahler, and Curtis E. Woodcock at Boston University's Center for Remote Sensing. My research is centrally concerned with the development and application of remote sensing, radiative transfer, image processing, and geostatistical techniques to measure and monitor global biophysical variables. My research has been positioned at the interface between theoretical modeling and data validation of global land surface albedo and reflectance anisotropy products. I have also focused on a number of technical assignments, such as performing instrument calibration, arranging measurement scenarios, and acquiring multiangular and multispectral observations suitable for satellite validation using NASA's suite of airborne science platforms. I am particularly interested in understanding the relation between vegetation parameters estimated from remotely sensed data at different spatial scales (from both airborne and satellite sensors) and the bidirectional reflectance distribution function (BRDF) of different surface types and ecosystems.

Specialties

Remote Sensing Algorithm Development and Validation, Terrestrial Ecosystem Analysis and Modeling, Radiative Transfer and Propagation Modeling, Design, Analysis, and Calibration of Electro-Optical (EO) Systems, Pattern-Recognition Analysis, Spectral Analysis (Multi/Hyperspectral), Systems Engineering, GIS-Based Risk Assessment and Mitigation, Geostatistical Modeling and Propagation of Uncertainty, GRID Computing, Education/Outreach, and Leadership Development.

Education

Ph.D. Geography (Major: Remote Sensing), 2009
Boston University - Graduate School of Arts and Sciences
M.Eng. Systems Engineering, 2005
Cornell University - Graduate School
B.S. Electrical Engineering, 2004
University of Puerto Rico – Mayagüez

Research and Professional Experiences

NASA-GSRP Fellow - MODIS BRDF/Albedo Group - 08/05 - Present
Boston University Center for Remote Sensing, Boston, MA

- To develop the algorithm theoretical basis, data processing, and validation protocols for the retrieval of BRDF and albedo from multiangular sensor observations.
- To perform instrument calibration, arrange field deployments, and acquire multiangular and multispectral observations suitable for satellite validation using NASA’s suite of airborne sensor systems e.g. the Cloud Absorption Radiometer, Ames Airborne Tracking Sunphotometer (AATS-14), and the Solar Spectral Flux Radiometer (SSFR).

- To deploy undercanopy lidar and optical analyzers (e.g. LAI-2000, TRAC, and hemispherical photography) to improve retrievals of vegetation structural parameters from airborne laser ranging data (e.g. NASA-LVIS).

Visiting Fellow (JPFP-MRA) - Earth Sciences Division - 05/05-09/05 ; 05/06-09/06
NASA Goddard Space Flight Center, Greenbelt, MD

- Coordinated production of in-depth accuracy and variability assessments for current and future reprocessing of global surface albedo and anisotropy products. Organized experimental campaigns through partnership with field observation programs (e.g. FLUXNET, NACP, ARM-DoE, and BSRN).
- Retrieved estimates of surface temperature and emissivity from airborne and satellite thermal infrared sensors (e.g. EOS-ASTER, MODIS, and ATLAS) to determine the surface energy response and turbulent fluxes of tropical urban environments.

Device Test Engineer - Laboratory for High Energy Astrophysics - 8/03 - 12/03
NASA Goddard Space Flight Center, Greenbelt MD

- Developed experimental and numerical characterization of quantum calorimeters under cryogenic conditions (50-100mK). Produced a high-resolution high-throughput model that successfully optimized the detection of faint x-ray sources (0.5-8.9keV) observed by position-sensitive quantum calorimeters using Mo/Au transition-edge sensors.

Remote Sensing Analyst - Hydrological Sciences Branch - 05/03 - 8/03
NASA Goddard Space Flight Center, Greenbelt, MD

- Developed satellite image processing tools and organized comparison studies using fieldwork and weather observation data to optimize the integration of urban-modified physical parameters (e.g. surface albedo, emissivity, land cover, roughness length, thermal, and hydraulic properties) into the National Center for Atmospheric Research (NCAR) Community Land Model Version 2 (CLM2) and the single column coupled NCAR Community Atmosphere Model CAM2/CLM2.

Geospatial Analyst - Gateway to the Earth Initiative - 5/01 - 12/01

United States Geological Survey Mapping Division, Reston, VA

- Designed, coded, and tested a geospatial server that managed caches and improved access to natural resource information from USGS digital mapping libraries.

Recent Awards and Honors

Who's Who in America (2008); NASA-GSRP Fellowship (2007-Present); NASA-JPFP Fellowship (2004-2007); NCAR-ASP Traineeship (2007); US Geospatial Intelligence Foundation Award (2005); Xerox Technical Research Award (2005); Cornell University Lazaro Fellowship (2004); NASA-PaSCoR Research Award (2002); IBM Corporation Traineeship at Harvard Business School (2002); USGS STAR Award (2001).

Groups and Associations

AGU, AMS, ASPRS, IEEE (GOLD/GRSS), INCOSE, NAAA, and Tau Beta Pi.

Technical Expertise

Programming Languages:	C, C++, Fortran, IDL, Java, Matlab, IGOR, Perl, MPI (IBM Blue Gene, pSeries, and SUN GRID), and Linux/Unix GNU Shell.
Applications:	R/S-Plus, AutoCAD, LabView, ENVI, ERDAS Imagine, Adobe Photoshop, MS-Office, Visio, Access, ArcGIS-View-IMS-SDE-Pad, ORACLE, PCI GEOMATICA, SAS, SPSS, ER-MAPPER, Origin, and eCognition.
Industry Standards:	ISO 14644 (for ISO 3-4 cleanrooms), HDF-EOS, OGC, DEM, USGS SDTS, XML, GPS, KML, and GML.

Selected Publications

Refereed Journal Articles

M. Román, C. B. Schaaf, G. P. Anderson, F. Gao, P. Lewis, J. L. Privette, A. H. Strahler, and C. E. Woodcock (2009), Assessing the Coupling between Surface Albedo derived from MODIS and the Fraction of Diffuse Skylight over Spatially-Characterized Landscapes. Remote Sensing of Environment, 2009. *(submitted)*

M. Román, C. B. Schaaf, C. E. Woodcock, A. H. Strahler, R. H. Braswell, P. S. Curtis, K. J. Davis, L. Gu, M. L. Goulden, D. Y. Hollinger, T. E. Kolb, T. P. Meyers, J. W. Munger, A. D. Richardson, T. B. Wilson, and S. C. Wofsy (2009), The MODIS BRDF/Albedo Product: Assessment of Spatial Representativeness over Forested Landscapes. Remote Sensing of Environment, 2009. *(accepted)*

M. Román, C. K. Gatebe, C. B. Schaaf, and M. D. King, Airborne Measurements of Surface Anisotropy over the US Southern Great Plains Ecosystems at Different Scales. *(in preparation*)

M. Román., C. B. Schaaf, C. E. Woodcock, M. Cosh, and A. H. Strahler (2009), Development of a Confidence Layer for the MODIS BRDF/Albedo Product, (*in preparation*).

D. Rutan, F. Rose, ***M. Román***, N. Manalo-Smith, C. B. Schaaf, and T. Charlock, Development and Assessment of Broadband Surface Albedo from CERES Clouds and Radiation Swath Data Product. Journal of Geophysical Research, 2008. *(in press)*

Liu, J., C. B. Schaaf, A. H. Strahler, Z. Jiao, Y Shuai, Q. Zhang, ***M. Román***, J. A. Augustine, and E. G. Dutton (2009), Validation of Moderate Resolution Imaging Spectroradiometer (MODIS) albedo retrieval algorithm: Dependence of albedo on solar zenith angle, J. Geophys. Res., 114, D01106, doi:10.1029/2008JD009969.

Knobelspiesse, K. D., B. Cairns, B. Schmid, ***M. Román***, and C. B. Schaaf (2008), Surface BRDF estimation from an aircraft compared to MODIS and ground estimates at the Southern Great Plains site, J. Geophys. Res., 113, D20105, doi:10.1029/2008JD010062.

Coddington, O., K. S. Schmidt, P. Pilewskie, W. J. Gore, R. W. Bergstrom, ***M. Román***, J. Redemann, P. B. Russell, J. Liu, and C. B. Schaaf (2008), Aircraft measurements of spectral surface albedo and its consistency with ground-based and space-borne observations, J. Geophys. Res., 113, D17209, doi:10.1029/2008JD010089.

Stone, R. S., G. P. Anderson, E. P. Shettle, E. Andrews, K. Loukachine, E. G. Dutton, C. B. Schaaf, and ***M. Román*** (2008), Radiative impact of boreal smoke in the Arctic: Observed and modeled, J. Geophys. Res., 113, D14S16, doi:10.1029/2007JD009657.

M. Román and A. H. Strahler, Land observation from geosynchronous earth orbit (LOGEO): Mission concept and preliminary engineering analysis, Acta Astronautica, 61:101–114, 2007.

S. Wallace, M. Gamache, and ***M. Román***, Last of the Amazon, National Geographic, p.40-71, Jan., 2007.

Book Chapters

Hill, M. J., ***M. Román***, and C B. Schaaf (2009), Chapter 1: Biogeography, Ecology and Dynamics of Global Savanna: A Geospatial View, in Ecosystem Function in Savannas: Measurement and Modeling at Landscape to Global Scales, edited by H. M. J., CRC Press, London, UK, In Preparation.